Discrete element method to study biofilm deformation in fluid flow

A thesis submitted to the Faculty of Science, Agriculture and Engineering for the Degree of Doctor of Philosophy

by

Yuqing Xia

School of Engineering, Newcastle University

2021

To my dear family and beloved friends who always support me

Abstract

Biofilms are the assemblage of one or more types of microorganisms, which are usually found attached and grew on surfaces, embedded in their extracellular polymeric substances (EPS). They could form diverse morphologies to adapt to different environments, especially in a flow system such as water filtration. Hydrodynamic conditions have a significant impact on the deformation and detachment of biofilm, which has been primarily investigated by the experiments. However, relevant modelling research is lacking. Therefore, the individual based model (IbM) is adopted to study the biofilm-fluid interaction in present work.

In the first part of this work, the discrete element method was utilized to simulate the biofilm growth, deformation and detachment, where the fluid was mimicked by applying a simple shear force. Due to the fact that the biofilms would also affect the flow pattern in return, the simply one-way approach was then extended to a two-way coupled computational fluid dynamic – discrete element method (CFD-DEM) model. Biofilm deformation and detachment was investigated at varied inlet flow velocity. We have also studied the effect of the EPS content on the deformation and detachment of biofilms. Furthermore, the strain-stress curves during biofilm deformation have been captured by loading and unloading the fluid shear stress.

Biofilm streamer (filamentous structure of biofilm) motion under different flow conditions is important for a wide range of industries as well. The flow-induced oscillations and cohesive failure of single and multiple biofilm streamers have been investigated based on the CFD-DEM model. In this section, we have studied the effect of streamer length on the oscillation at varied flow rates. The predicted single biofilm streamer oscillations in various flow rates agreed well with experimental measurements. We have also investigated the effect of the spatial arrangement of streamers on interactions between two oscillating streamers in parallel and tandem arrangements. Besides, cohesive failure of streamers was studied in an accelerating fluid flow, which is important for slowing down biofilm induced clogging.

Acknowledgements

First and foremost, I would like to express sincere gratitude to my supervisor Dr. Jinju Chen for her invaluable advice, continuous support, and patience during my PhD study. Her perspective on life, immense knowledge and plentiful experience have encouraged me in all the time of my academic research and daily life.

I would like to thank Dr. Pahala Gedara Jayathilake for the constructive suggestions, help and availability. I do appreciate all his help and time in modelling learning, and he always answer my questions patiently. I would also like to thank Dr. Bowen Li for his help and time with the software and codes.

I would also like to acknowledge EPSRC funded NUFEB project and BBSRC NBIC funded project for partially sponsoring my research.

I am deeply grateful to my landlord and friend Wendy Zhang, I have lived with her from the first day I arrived Newcastle. She almost helped me solve all the difficulties encountered in life.

I would like to especially thank my boyfriend Liang Wang for his love, endless support, encouragement and delicious food he cooks.

Above all I would like to offer my special thanks to my parents for their endless support on every decision I made.

Contents

Figure list

Table list

Abbreviations

1D	One-dimensional
2D	Two-dimensional
3D	Three-dimensional
AB	Acid-base
AOB	Ammonia Oxidizing Bacteria
BbM	Biomass-based model
CA	Cellular Automaton
CFD	Computational fluid dynamics
DEM	Discrete Element Method
DLA	Diffusion-limited aggregation
EL	Electrostatic
EPS	Extracellular polymeric substances
HET	Heterotrophic bacteria
IbM	Individual based model
LW	Lifshitz-Van der Waals
MAC	Marker-And-Cell
MCBs	Mixed-culture biofilms
MD	Molecular dynamics
NOB	Nitrite Oxidizing Bacteria
OCT	Optical coherence tomography

Symbols

Ks	Substrate affinity
μ_{max}	Maximum specific growth rate
S_S	Nutrient concentrations
Y_{eps}	EPS formation coefficient
D	Effective diffusion coefficient
D_s	Diffusion coefficient for substrate
R	Nutrient uptake rate
$\vec{F}_{a,i}$	Adhesive force
$\vec{F}_{c,i}$	Contact force
$\vec{F}_{d,i}$	Drag force
k^{eps}	Spring stiffness per unit mass
k_n	Elastic constant for normal contact
k_t	Elastic constant for tangential contact
γ_n	Damping coefficient for normal contact
γ_t	Damping coefficient for tangential contact
$\vec{F}_{coh,i}$	Inter-particle cohesive force
$\vec{F}_{fp,i}$	fluid-particles interaction force
ϵ_s	solid volume fraction
ϵ_f	fluid volume fraction
ζ	Shear rate
R_e	Reynolds number
E	Young’s modulus

G	Shear modulus
φ	Fraction coefficient
η	Fluid dynamic viscosity
S_t	Strouhal number

1 Introduction

Biofilms usually form in aqueous environments when planktonic microbials attach to the surface (e.g. metal, plastic or tissue) and enclose in the extracellular polymeric substances (EPS) which are produced by themselves [1, 2]. EPS production and biofilm formation confers many advantages to the microorganisms. For instance, EPS could provide a sufficient physical resistance when biofilm experience external force, such as the shear force in the hydrodynamic environments [3]. Comparing with planktonic counterparts, it was also found that bacteria in biofilms have a higher resistant (10-1000 times) to antibiotics [1, 4].

Biofilms have advantageous application in several fields. The biosorption capacity of biofilm allows them to remove heavy metals from wastewater [5]. Biofilms also play an important role on bioremediation since the toxic pollutants could be converted to less toxic or harmless productions by the enzymatic activity of microbes [6, 7]. However, biofilms also have numerous harmful impacts. In the nature setting, most biofilm contain multi-species which might be quite harmful for human health. It was reported by National Institutes of Health that over 80 % of infections in the body are caused by biofilms [8]. For example, biofilm formation on the surface of medical devices, such as heart valves, intravascular catheters and orthopaedic implants, is becoming the major pathogenesis of implant infection and can rapidly spread to patients [9, 10]. In addition, biofilms can form quickly in food industry environment and create a persistent source of contamination, the pathogenic species within biofilm would lead to a serious impact on human health and economy [11, 12]. Therefore, a deep insight into how biofilm interact with the mechanical force in its surroundings may contribute to biofilm control and removal.

By considering biofilms as biomaterials, many experiments have been performed to measure the mechanical properties of biofilms and shown their viscoelastic behaviours when exposed to external stress [13-16]. However, it is hard to test and analyse biofilms mechanically since they are microscopically small and nonuniform [17], thus the mechanical properties of biofilm are still not entirely known. As such, computational modelling of biofilms could be a powerful assistance in studying how biofilm response to the external force. Recently, individual based model (IbM) seems to be appealing to biofilm researchers because this approach allows individual variability, it was widely used to mimic biofilm formation since it can provide a high resolution of biofilm structure [18, 19]. However, IbM is rarely used to simulate fluid induced biofilm deformation and detachment.

As biofilms are always subjected to a range of fluid flow conditions, biofilm deformation and detachment are very important behaviors to help them to resist to the fluid shear force. In this case, the biofilm deformation and detachment are affected by the morphology of biofilm, fluid shear force and their living matrix (EPS). The effect of EPS on biofilm structure have been investigated by using IbM in [20], however, little is known about its effect on biofilm deformation and detachment when expose to fluid shear force. Moreover, the filamentous structure of biofilm, which is so-called biofilm streamer, comes from the deformation of biofilm, and highly relevant to a wide range of critical biomedical situations and industrial applications including clogging of catheters, heart stents, and water filtration systems [21, 22]. The existing experimental work has also shown that the biofilm streamer could be found under both turbulent and laminar fluids [23, 24]. However, there was lack of micro-scale models to describe the biofilm deformation, detachment and biofilm streamer motion in the fluid flow, this project tends to tackle this issue. In this project, IbM approach was firstly adopted to study biofilm deformation and detachment by applying a simple shear flow, then the two-way coupled CFD-DEM (Computational Fluid Dynamics – Discrete Element Method) approach was utilized to study biofilm streamer oscillation and biofilm deformation and detachment under different hydrodynamic conditions.

1.1 Aim and objective

The aim of this project is to investigate biofilm deformation and detachment under different flow conditions and how EPS production affects biofilm deformation and detachment. The specific objectives are to:

- adopt one-way model to investigate the biofilm deformation and detachment by varying EPS amount and shear rate.
- adopt two-way coupled CFD-DEM model to study biofilm streamer/flow interaction in different hydrodynamic conditions. In addition, the cohesive failure of biofilm streamer in fluid flow has been predicted as well.
- adopt two-way coupled CFD-DEM model to study biofilm deformation and detachment in hydrodynamic conditions.
- adopt two-way coupled CFD-DEM model to express the relationship between the stress and strain during biofilm deformation-recovery test.

1.2 Thesis structure

The thesis is divided into 7 chapters including this chapter 1 which gives an introduction, scope and objectives of this project.

Chapter 2 presents a review on the literature relevant to this project which consists of four main sections: (1) the details of biofilm development; (2) experimental investigation of flow induced biofilm deformation; (3) evolution of biofilm models including continuum models and discrete models. (4) viscoelastic properties of biofilm.

Chapter 3 provides a detailed methodology of the models employed in this thesis. Firstly, the sub-models in the IbM (NUFEB), such as biological processes and mechanical interactions, were explained with great details. Following that, the two-way coupled biofilm model with computational fluid dynamics (DEM-CFD model) was elaborated.

Chapter 4 presents IbM simulation of biofilm deformation and detachment by applying a simple shear flow which could be controlled by the input shear rate. The effect of EPS production and flow shear rate on biofilm deformation and detachment have been investigated. Biofilm detachment coefficient rate has been calculated to describe the detachment events in each case.

Chapter 5 presents CFD-DEM simulations of biofilm streamer oscillation in different hydrodynamic conditions. The amplitude and frequency of single biofilm oscillation have been studies. In addition, the oscillation of two biofilms in parallel and tandem arrangement have been studied by change the spacing distance between them. The fluid induced biofilm streamer failure has been predicted by using the two-way coupled approach.

Chapter 6 presents CFD-DEM simulation of biofilm deformation and detachment in various hydrodynamic conditions. Biofilm was pre-grown by using IbM described in chapter 1. The effect of fluid velocity and EPS production have been investigated. In addition, the deformation-recovery test was carried out to obtain the stress-strain curve thus to illustrate the mechanical properties of biofilm.

Chapter 7 concludes the research work in this thesis and provides an outlook of future work.

Publication based on this thesis:

Xia, Y., Jayathilake, P. G., Li, B., Zuliani, P., & Chen, J. (2021). CFD–DEM modelling of biofilm streamer oscillations and their cohesive failure in fluid flow. *Biotechnology and bioengineering*, *118*(2), 918-929.

Xia, Y., Jayathilake, P. G., Li, B., Zuliani, P., & Chen, J. Modelling fluid induced biofilm deformation and detachmen by CFD-DEM approach. (In preparation)

Other publications:

Xia, Y., Duan, P., & Chen, J. (2018). Modelling the nanomechanical responses of biofilms grown on the indenter probe. Processes, 6(7), 84

Kandemir, N., **Xia, Y.**, Duan, P., Yang, W., & Chen, J. (2018). Rheological characterization of Agarose and Poloxamer 407 (P407) based hydrogels. MRS Advances, 3(30), 1719-1724

Duan, P., **Xia, Y.**, Bull, S., & Chen, J. (2018). Finite element modeling of nanoindentation response of elastic fiber-matrix composites. Journal of Materials Research, 33(17), 2494-2503.

2 Literature review

2.1 Biofilm development

The conception of “biofilm” was proposed by an extraordinary medical scientist named John William Costerton (1934-2012), but it had been disregarded at that time, however, this notion was gradually becoming very important in bacteriology and related research fields [25]. So, what is a biofilm? As early as 1977, Costerton’s group found the rumen bacteria were surrounded and protected by extracellular structures [26] which was later introduced as glycocalyx [27]. Thereafter, they observed that the biofilm could be developed by the bacteria and their exopolysaccharide product on the latex surface within 8 hours, these embedded bacteria have high antimicrobial resistance compared with the planktonic bacteria [28, 29]. Furthermore, it has been reported that the bacteria can survive easier and exist for a longer time in the biofilms [25]. When the components inside the extracellular structure were fully discovered, the term was altered to extracellular polymeric substance (EPS) [30]. Overall, the biofilm is a result of microorganisms accumulation with the EPS produced at interfaces [2].

The schematic for typical stages of biofilm development has been displayed in figure 2.1. The planktonic bacteria are suspended in the bulk liquid, which can approach the solid surface by passive or active movement [31]. When the condition is suitable for growth, the cells could permanently adhere to the surface and start to grow. The extracellular polymeric substance could be extracted during bacteria growth and embeds the cells to form the initial biofilm. Subsequently, bacteria proliferate in biofilm and evolve into mature biofilm. Finally, biofilm dispersal occurs. Some bacteria leave from the mature system, dispersing into the aqueous, which may land on the surface and start biofilm recolonization [32]. More details about biofilm development will be explained below.

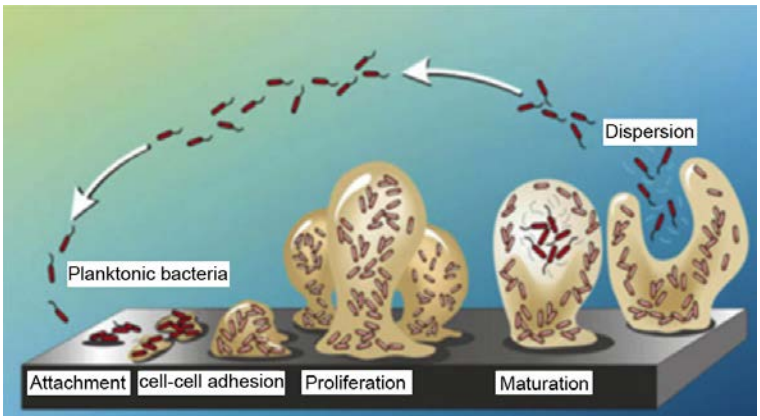

Figure 2.1. The stages of biofilm development [33].

2.1.1 Reversible-irreversible adhesion of bacteria

The initial step of biofilm formation is the adhesion of planktonic bacterial cells to the surface. This process could be influenced by both biological, chemical and physical properties of the surrounding environment [31]. The liquid environment could be divided into three regions: (1) the bulk liquid where the cells are not affected by the surface and could move freely; (2) near-surface fluid layer where the cells are subjected to fluid shear force; (3) the surface where cells are experiencing both hydrodynamic and physicochemical effects, such as van der Waals interaction which is generally attractive, and electrostatic interaction which is attraction or repulsion determined by ionic strength and pH [34, 35]. Furthermore, the surface hydrophobicity of bacteria and the materials surface can also affect the initial bacterial attachment. Therefore, the total energy between a cell and the surface is the sum of Lifshitz-Van der Waals interaction (LW), electrostatic interaction (EL) energies and acid-base (AB) interaction energies (due to surface hydrophobicity) [36, 37]. Non-motile bacteria could be transported to the surface by passive movement is usually driven by the gravity and Brownian motion in the liquid environment [25, 38], while the motile bacteria approaches the surface by a self-propelled active movement. At the reversible attachment stage, the bacterial loosely adhere to surface and could also quickly detach [39], and those bacteria reach irreversible adhesion when they overcome the physical repulsive force [40]. The transition from reversible to irreversible adhesion takes several hours. EPS can immobilize bacterial cells to the surface to facilitate this process. Besides, the organelles in the bacteria surface, such as flagella, pili can help the bacteria to achieve the irreversible attachment [34, 41]. As shown in figure 2.2, when the repulsive force is high, the bacteria will be prevented from approaching the surface by an energy barrier. In this case, the nanofibers on bacteria surface are utilized to pierce the energy

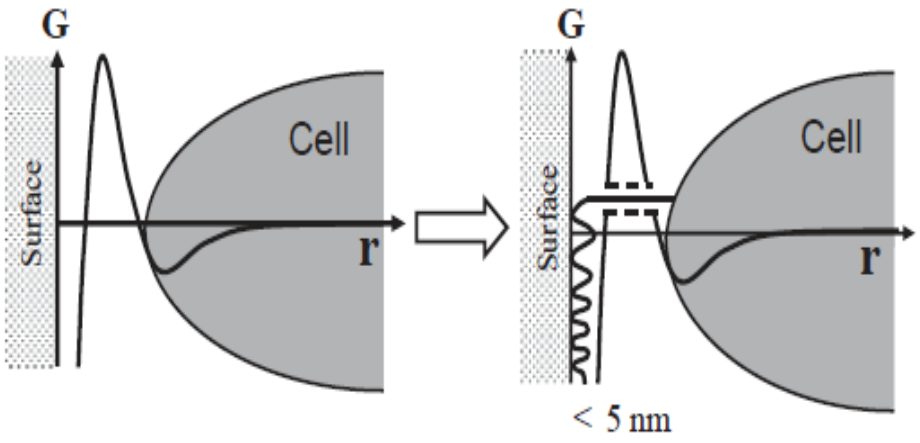

Figure 2.2. Bacteria adhere to the surface with nanofiber [25].

barrier, hence behave as a bridge between the bacterium and the surface [25]. Then the bacteria will reposition their body to a longitudinal position to obtain the maximum contact area to reach irreversible adhesion [42].

2.1.2 Bacterial growth

Bacterial cell growth is the next step following the irreversible attachment. To investigate and understand the bacterial growth, cells are often cultivated in the aqueous solution with supply of nutrients. The growth curves of bacteria could be obtained. As shown in figure 2.3, the whole growth process often consists of four distinct growth phases: the lag phase, the exponential phases, the stationary phase and the death phase.

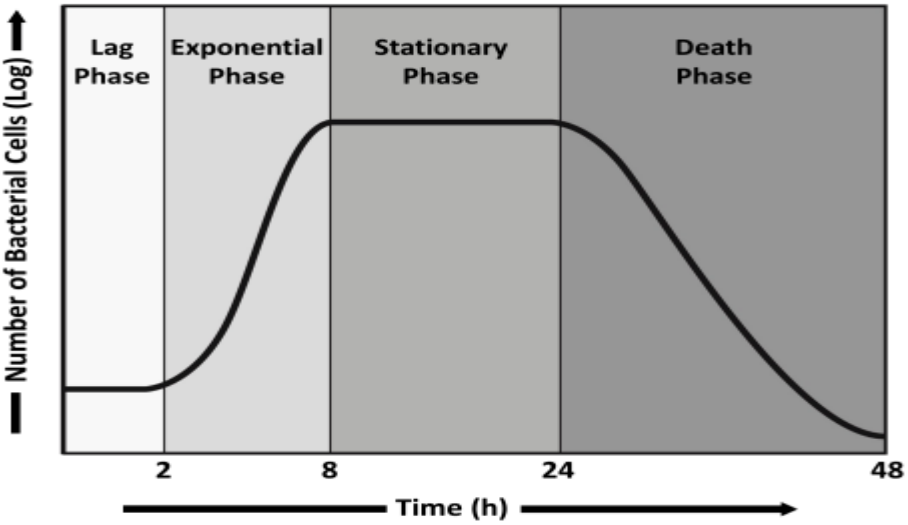

Figure 2.3. Four phases of bacteria growth [43].

According to experimental observation, lag phase is the first stage of the bacterial growth cycle, and it is defined as the duration from the bacteria are inoculated into the medium to the beginning of division [44], the growth rate is 0 on this phase. Bacteria sense the new living environment and adapt the new environment during this phase, hence, prepared for the exponential growth. During the exponentail phase, one cell divided into two cells, the number of cells increases exponentially, growth rate in this period is greatest and could be affected by environment factors like temperature and nutrient supply. However, the exponential growth in a batch culture is limited, after that cell growth reaches a plateau which is called stationary phase. In this phase, cells continue to divide and grow, but the number of increasing cells is equal to the number of dead cells, consquently, no net gowth was observed [44]. One common reason for the stationary phase is that the nutreint was consumed by the exponentially growing

cells [45]. Death phase is the final stage of bacterial growth, the number of organisms decreased exponentially during this phase and the death rate is less than the growth rate on the exponential phase.

2.1.3 Biofilm dispersal and detachment

Biofilm dispersal and detachment is used to describe the final stage of biofilm development, the bacterial cells will departure from the mature biofilm system and return to planktonic state to start recolonization. Dispersion of biofilm could be divided into two part: passive dispersal and active dispersal [46]. The passive dispersal refers to biofilm detachment due to external force, such as shear stress. Individual cells or cell flocs release from the mature biofilm during detachment [47]. There are three major mechanisms that cause biofilm detachment (1) sloughing: removal of the large section from the whole biofilm architecture; (2) erosion: physical force like shear stress and cell-mediated type events induced continuous loss of single particles. (3) abrasion: the detachment caused by the collision of agents from the solution with the biofilm [25]. Traditionally, the shear force used to be identified as the dominate mechanisms for biofilm detachment, however, more mechanisms have been discovered which contribute to the dispersal of biofilm as well. These include quorum sensing and increased expression of flagella [48]. These kinds of dispersal are termed active dispersal since the induced mechanisms are initiated by the bacteria. Other examples include the depletion of oxygen, and dead cells in the biofilm all could induce the biofilm dispersal. Overall, biofilm detachment is a pressing subject required further investigation as it is highly relevant to the biomaterials-related infections [49, 50], bacteria induced corrosions [51, 52] , and the increased drag for marine industries [53].

2.2 Flow induced biofilm deformation

2.2.1 Biofilm deformation and detachment in the hydrodynamic conditions

The external shear force from the hydrodynamic environment could cause the deformation and detachment of the biofilm. The behaviour of biofilm varies with the fluid conditions. For example, the fluctuate fluid was applied to investigate the biofilm deformation, the experiment demonstrated that the biofilm may behave like viscoelastic fluids [16, 54]. Biofilm grown in different flow conditions may have different mechanical resilience. For example, after growing biofilm (mixed various *P.aeruginosa* strains) at fluid velocity of 0.03 m/s and 1 m/s for 6 days, it was found that biofilm grown under high shear rate appears to be stronger and more resistant to the fluid shear force. For biofilms grown on both low and high shear rates, the detachment

rate coefficient increased with the fluid velocity [54]. Later, biofilm rolling migration controlled by viscoelastic tethers was captured in [15]. The mechanical deformation and failure of biofilms can be characterized by utilizing capillary flow cell methods [55]. In this case, *Staphylococcus epidermidis* biofilm was grown in a capillary flow cell at a flow rate of 1 mL/min, then a shear test was performed for 15 seconds with increasing flow velocity. Figure 2.4 displays the biofilm deformation along the downstream direction. Biofilm recovery could be monitored by high-speed camera when the flow was stopped. In this experiment, 5 cases were carried out by treating the biofilms with chemical or enzymatic agents. The results shown that the biofilms treated with urea or DispersinB appear to be weaker and they deform more when subjected to the fluid flow.

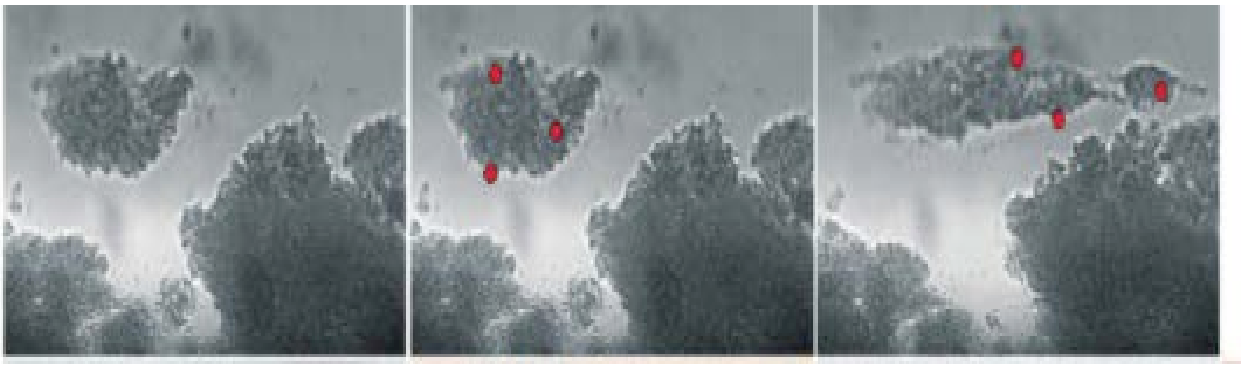

Figure 2.4. Biofilm deformation during a capillary flow test [55].

Recently, optical coherence tomography (OCT) has been employed for the study of biofilm structure and fluid-structure interaction [56]. The structure of biofilms grown in different flow conditions has been visualized successfully by using OCT [57]. As a result, heterogeneous structure of biofilm was captured when biofilm was subjected to a laminar flow or transient flow. However, when a turbulent flow was applied, the biofilm structure became more homogeneous. Later, time-resolved deformation of biofilm has been measured by using optical coherence tomography during the flow tests [58]. In the first time-lapsed experiment, the biofilm was subjected to a shear stress of 1.64 Pa for 30 minutes, followed by a 20-minute relaxation wherein no shear stress was applied. Figure 2.5 displays the deformation and recovery of biofilm in 50 minutes, the biofilm returned to its original shape after 50 minutes due to the elastic response. Additional stress-strain experiments were carried out to investigate the viscoelastic properties of biofilm by incrementally increasing and decreasing the shear stress in the range of 0-3.6 Pa. The results illustrated that the shear stress have a linear correlation to

the resulting strain in the loading cycle, the Young's modulus was estimated to equal to 36.0 ± 2.6 Pa [58].

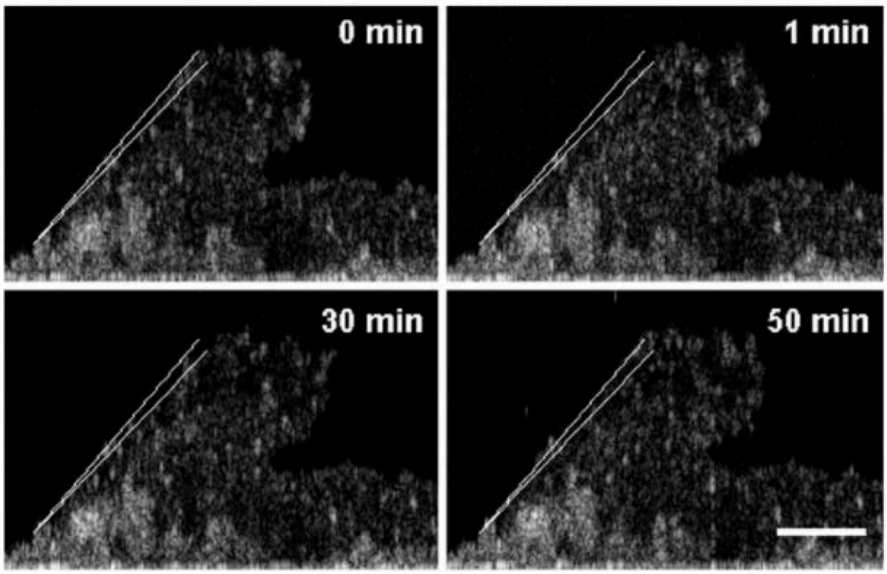

Figure 2.5. Biofilm deformation in a creep-recover test. The biofilm was exposed to a shear stress for 30 minutes followed by a relaxation of 20 min. Scale-bar equals 250 μm [58].

2.2.2 Biofilm streamers formation in flow

Klapper et al. found that extracellular matrix can hold the cells together to develop the thread-like biofilm structure and suspended freely with fluid flow [59]. This filamentous structures of biofilms is so-called biofilm streamer and may cause emergent clogging of medical stents and industrial filters [60].

In order to investigate the characteristics and formation of biofilm streamers, Stoodley et al. cultivated the mixed biofilm (*Pseudomonas aeruginosa*, *P. fluorescens* and *Klebsiella pneumonia*) under turbulent flow which is more related to the industrial environments [23]. The reactor was established by a flow cell integrated with a mixing chamber, and a differential pressure sensor is utilized to measure the pressure drop across the flow cell. The velocity of the water flow is 18 cm/s, and after 7 days growth, the biofilm streamers were observed and oscillated in the fluid, as shown in figure 2.6. The length of the streamer is up to 3mm. The average flow velocity was increased from 0 to 50.5 cm/s, as a result, the amplitude of the streamer became larger with the increase in average flow velocity. In addition, the pressure drops across flow cell significantly raised after biofilm growth and streamer formation. This is consistent with the hypothesis of Picologlou et al. [61]. In addition, Stoodley et al. [54] performed another experiment in 2002, the *Pseudomonas aeruginosa* PAN067 were cultivated

under both turbulent and laminar conditions, the average flow velocity is 1 m/s (Reynold number R_e = 3636) and 0.033 m/s (R_e = 120), respectively. The biofilm grew under laminar flow was much smaller than those grew in turbulent condition, and the filamentous streamers could be observed in the high-velocity fluids.

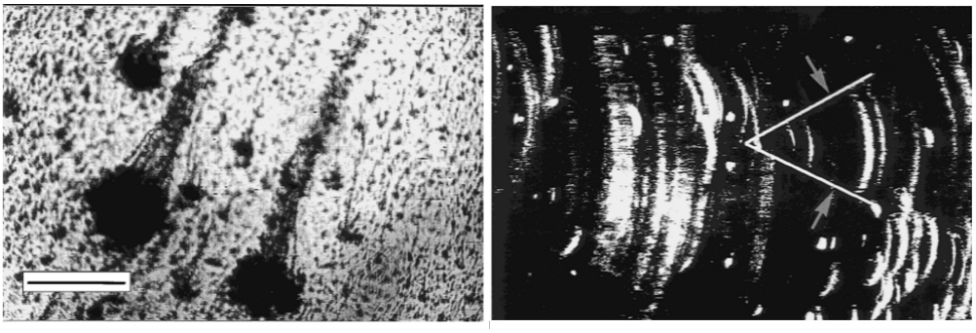

Figure 2.6. Biofilm streamer and streamer oscillation. Scale-bar equals 500 μm [23].

Nevertheless, the biofilm streamers can also form in low Reynolds number flow as well. As shown in figure 2.7(a), the microfluidic curved channel, which consist of sharp and round corners, had been used to capture the filamentous biofilm structure [24]. In this experiment, the bacterial solution was infused into the channel continually, after a few hours, biofilm streamer could be observed in a plane at half the channel height. Figure 2.7(b) and (c) showed biofilm streamer formation produced by two different bacterial concentrations (i.e. OD_{600} = 0.4 and OD_{600} = 0.17). It is clear that the streamer grew fast when the concentration of bacteria is higher (figure 2.7(b)). In addition, they found that the shape of corner did not affect the streamer formation.

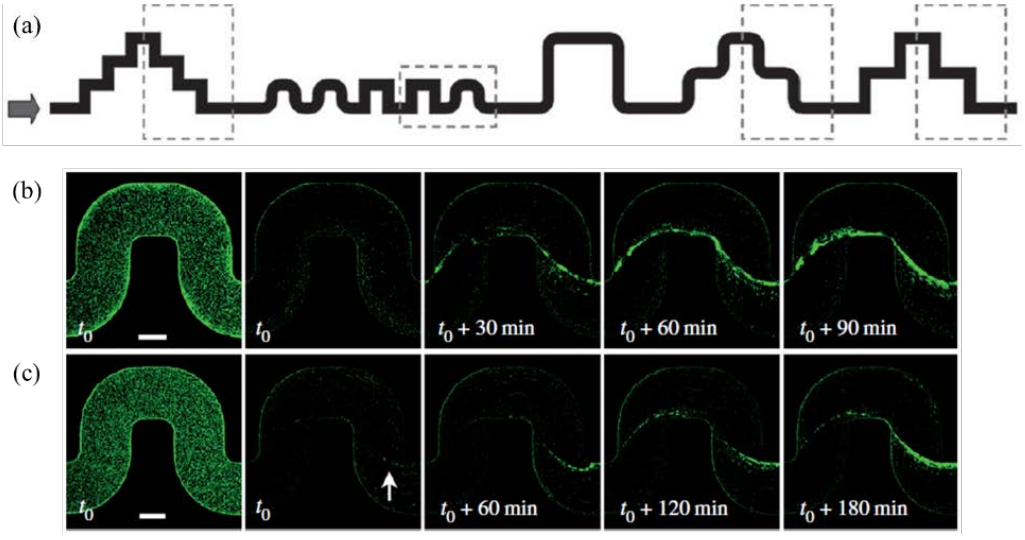

Figure 2.7. (a) The layout of the microfluidic channels. (b) and (c) streamer formed with time from two different experiment sets. t_0 is equal to 6 h in (b) and 7 h in (c). Scale-bars are 100 μm [24].

In principle, biofilm streamer would fully develop and grow stably on porous materials due to their greater exposed area. Thereby, a few studies have also investigated the biofilm streamer formation in porous media. For example, Valiei et al. [62] utilized microchannel with a number of embedded microposts as the porous media to grow the biofilm, with fluid flow controlled by a microfluidic device. In this study, the wild type *Pseudomonas fluorescens* CHA0 was injected into the microfluidic instrument at flow rate of 0.8 μL h^{-1}, no biofilm streamer formed after 24 hours, and this phenomenon has not changed with the increase in flow rate. Nevertheless, after infusing culture medium to biofilms, streamers were observed in few hours. In addition, the results also show that the streamers grew faster with increased flow rate, but they were non-persistent at high flow rate.

Meanwhile, Drescher et al. [60] used a model fluidic system consisting of an array of corners, *P. aeruginosa* cells were loaded into a reservoir in this experiment and then swimming into the microfluidic channel with a flow driven by a constant pressure. As a result, they found a rapid clogging induced by the biofilm streamers in this experimental system. However, it is worth noting that the biofilm grew on the chamber walls initially and slightly decreased the flow rate in 50 hours (T). While the biofilm streamer formed at the corner make a sharply decrease in the flow rate and cause clogging at a short timescales t = 30 mins, as illustrated in figure 2.8. In addition, they establish a transparent porous material which is similar to fine sand layers. Consequently, it was found that the biofilm streamers developed rapidly and cause clogging in this soil-like environment.

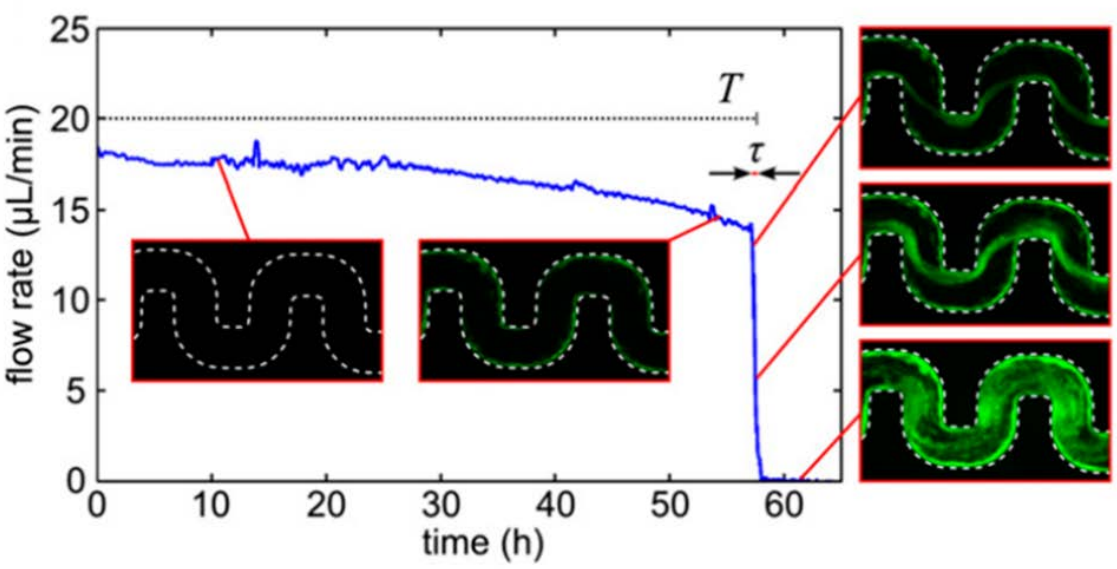

Figure 2.8. The flow rate measurement over time, T = 50 h and t = 30 mins [60].

Recently, a new flow-induced bacterial streamer from pre-formed bacterial flocs at low Reynold number ($Re = 0.001$) has been discovered by Hassanpourfard and Nikakhtari [63]. In this experiment, the bacterial flocs are formed by growing the wild type (WT) strain of *Pseudomonas fluorescens* in a solution at 30 ℃ overnight. The microfluidic system they used was a grid pattern with an array of polydimethylsiloxane micropillars, and the flow in the channel was in the creeping flow regime. It was found that the biofilm flocs got attached to the micropillars initially when imposed the fluid flow, subsequently the filamentous streamers formed in few minutes due to the flocs deformation which was caused by the hydrodynamic shear forces (Figure 2.9). Finally, it was shown that the formation of streamers could block the microfluidic devices.

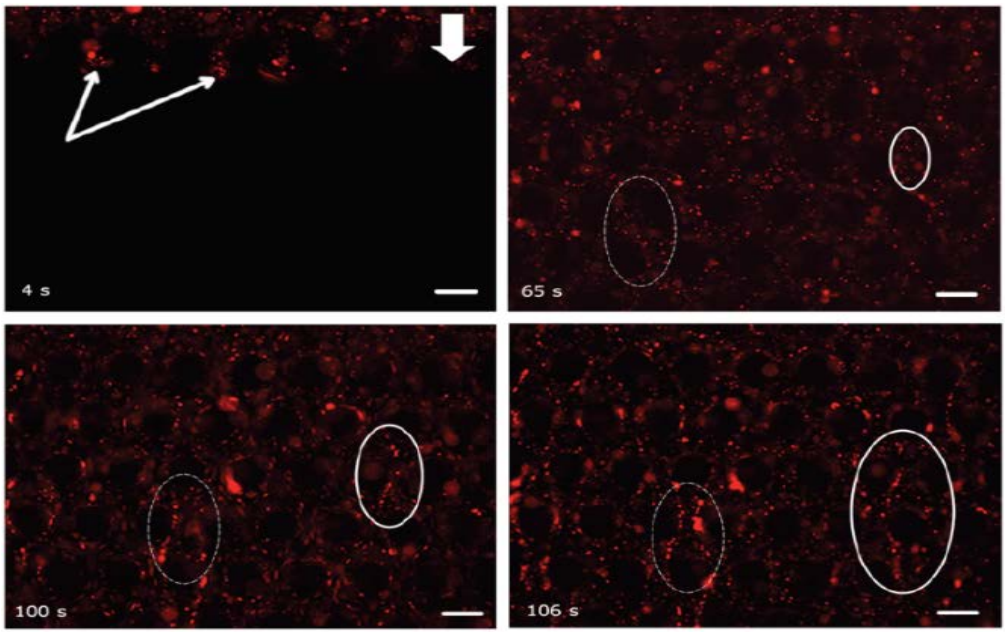

Figure 2.9. The streamer formed in a short time scale and the location of this event was marked by the dashed ellipse. The arrows demarcate the advancing fluid meniscus. Scale-bars are 50 μm [63].

2.3 Computational models for biofilm

Biofilms are everywhere and have a significant impact in both nature and industry. Extensive experimental research has been performed to have a better understanding of the biofilms, such as biofilm formation and their behaviours in the different environments [55, 58, 64]. However, the experimental work alone may not be able to reveal all the physical insights of microbial system. Biofilm features can be described by using mathematical models. These models can be implemented in computational models and play a significant role to complement the experiments [65]. A wide variety of experimental results could be used to calibrate

mathematical models, meanwhile, those models could be validated via appropriate experiments as well. Hence, the mathematical models have the potential to investigate the more complex behaviours of the biofilm. Over the years, the computational models have been developed from simple one-dimensional to multidimensional models, most features of biofilm could be simulated by using those models. Overall, there are two main categories: continuum model and discrete model. In the continuum model, the biofilm is characterized by a continuous biomass, and the biomass spreading was solved by using differential equations. Therefore, the quantitative results for substrate transport could be obtained by the model. However, biomass spreading in discrete element model is a stochastic process, therefore, the heterogenetic structures represented by discrete model often have better agreement with the experimental observation [66].

In this section, the typical biofilm models have been described. The continuum biofilm models have been classified in one-dimensional and multidimensional models. The discrete models are introduced from Cellular Automaton (CA) model, hybrid differential-discrete Cellular Automaton models to Individual-based models (IbMs).

2.3.1 One-dimensional continuum biofilm models

At early stage, one-dimensional continuum models were initially developed for mathematical description of biofilm. Most of these models were able to investigate a steady-state biofilm which has no net growth nor decay [67]. In 1976, a conceptual model which includes the main parameters such as the maximum utilization rate coefficient, half-velocity coefficient and the substrate diffusion coefficients, has been established to investigate the substrate utilization within biofilms [68]. In this study, the biofilm adhered to a flat surface with infinite length and width. The biofilm was characterized by the depth L_f and density X_f. In addition, the reaction rate was assumed to be limited by a single substrate, the concentration of the substrate varies along z direction (normal to the biofilm surface). The utilization of substrate in the biofilm was assumed to follow the Monod relation, based on the Fick's second law, the differential equation for substrate concentration within the biofilm could be expressed as [68]:

$$D_f \frac{d^2 S_f}{dz^2} = \frac{k S_f X_f}{(S_f + K_s)} \tag{2.1}$$

S_f is the concentration of substrate at any point in the biofilm matrix (mg/l), k is the maximum utilization rate of the substrate, refers to substrate mass consumed per unit mass of organisms per day (day^{-1}), D_f is the diffusion coefficient in biofilms (cm^2/day) and K_s is the half-velocity

coefficient (mg/l). Although the substrate utilization in a biofilm could be illustrated by using this simple model, it didn't take biofilm growth and decay into considerations. Therefore, this fundamental model has been refined by applying bacterial growth kinetic to the steady-state biofilm, the net growth rate of bacterial mass could be expressed by the following formula [69]:

$$\frac{\partial AX_f dz}{\partial t} = Y \frac{kS_f}{K_s + S_f} AX_f dz - bAX_f dz \tag{2.2}$$

A and dz are the cross-section area and thickness of a biofilm section, Y is the yield of bacterial mass per unit of substrate utilized ($M_x {M_s}^{-1}$), M_x and M_s are the mass of bacteria and substrate, b is the decay coefficient (T^{-1}). According to energy conservation and mass balance, the net thickness of biofilm could be kept as constant. However, in addition to the bacteria decay, the external force could also cause the decrease in bacterial mass, therefore, the biomass might be overestimated when using this model [69]. In [70], *Rittman* has improved the mathematical formula for biofilm loss by incorporating the bacteria decay and shear stress induced biomass loss, the biomass loss rate due to shear stress was obtained from experimental work.

With the continuous development of biofilm research, a general 1D multispecies model has been established and allows the description of a dynamic biofilm and the investigation of the interactions among different microbial species [71]. The model was derived in z direction by assuming the biomass to be treated as continuum, which means the biomass was characterized by the average quantities such as the concentration of microorganisms. As shown in figure 2.10, there are nx microbial species in a differential volume element $A\ dz$, for the microbial species i, the mass balance could be expressed as [71]:

$$\frac{\partial [A\ dz\ \rho_i f_i(t,z)]}{\partial t} = A\ dz\ \mu_i(t,z)\rho_i f_i(t,z) + A g_i(t,z) - A\left[g_i(t,z) + \frac{\partial g_i(t,z)}{\partial z}\ dz\right] \tag{2.3}$$

ρ_i is the density of the individual microbial species i, which is assumed to be a constant in the model. μ_i is the observed specific growth rate. f_i is the volume fraction of the i-th species, the summation of volume fraction over all nx species equals to 1($\sum_{i=1}^{nx} f_i = 1$). g_i is the biomass flux, that is, the amount of mass of species i displaced per unit time across a unit area which is perpendicular to the z-direction [72]. g_i could be further expressed as $g_i(t,z) = u(t,z)\rho_i f_i(t,z)$, where $u(t,z)$ denotes the velocity of microbial mass flowing. Therefore, equation (2.1) could be written as:

$$\frac{\partial f_i}{\partial t} = \left(\mu_i - \frac{\partial u}{\partial z}\right) f_i - u \frac{\partial f_i}{\partial z} \tag{2.4}$$

Summing equation (2.4) over all species, the mean observed specific growth rate could be expressed as:

$$\bar{\mu}(t,z) = \frac{\partial u(t,z)}{\partial z} \tag{2.5}$$

Substituting equation (2.5) into equation (2.4), the mass balance could then be described by the following equation:

$$\frac{\partial f_i(t,z)}{\partial t} = [\mu_i(t,z) - \bar{\mu}(t,z)]f_i(t,z) - u(t,z)\frac{\partial f_i(t,z)}{\partial z}] \tag{2.6}$$

The mass balance for any substrate i could be derived in the same way:

$$\frac{\partial S_i(t,z)}{\partial t} = r_i(t,z) + \frac{\partial}{\partial z}(D_i \frac{\partial S_i(t,z)}{\partial z}) \tag{2.7}$$

S_i, r_i and D_i are the concentration, observed conversion rate and diffusion coefficient of substrate i.

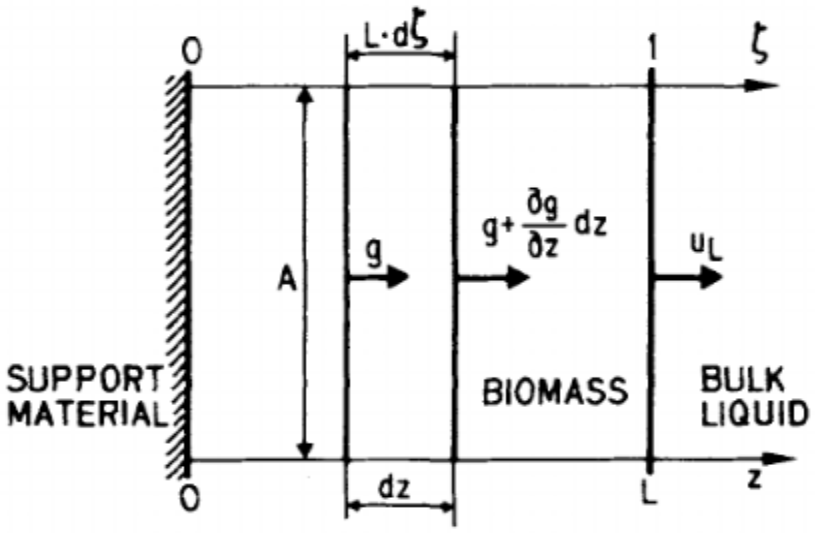

Figure 2.10. Flux of biomass through a differential volume element of an expanding idealized biofilm [71].

The model was used to investigate the competition in the mixed biofilm which consists of heterotrophic and autotrophic species. The biofilm growth under the following five different conditions has been studied: (1). Unrestricted biofilm growth with constant substrate concentration. In this case, the thickness of biofilm exponentially increases in the first three days, after several days, biofilm thickness increases continuously at a low constant rate due to the carbon limited heterotrophs growth and oxygen limited autotrophs growth. (2). Biofilm growth with changed substrate concentration. The oxygen flux dropped immediately after the

organics have been removed, thus, the autotrophs become dominant in the biofilm. (3). Biofilm growth with shear stress induced biomass loss which was described as $\sigma = -\lambda L^2$, where λ is the coefficient and L is the biofilm thickness. The fast-growing heterotrophs could be removed from the biofilm surface by shear, further lead to an increase in the abundance of nearby autotrophs. Thus, the performance of autotrophs improved overtime. (4). Biomass sloughing ($\Delta L = \sigma \Delta t$) has been included during biofilm growth, which cause two species take turns to dominate the biofilm. (5). Biofilm growth in the mixed reactor with external mass transfer resistance. In this case, the competition within the biofilm is unobvious. This mixed-culture biofilms (MCBs) model has been extended by using a mathematical software-AQUASIM [73]. Additional processes, such as the variable biofilm liquid phase volume fraction, simultaneous attachment and detachment at the interface between biofilm and bulk liquid, have been included in the refined MCBs model. Furthermore, the geometry of the biofilm could be defined as a plane, cylinder or sphere. This detailed model has demonstrated to be a powerful tool to reproduce and analyse the new experimental data during 1986-1996. However, there are a large number of differential equations have been implemented into the model which makes it relatively inefficient. To reduce the computational cost, a simplified MCBs model has been established in [74]. In which case, the modelling of diffusion process and spatial distribution of microorganic species for biokinetic reactions has been decoupled to decrease the model complexity. As illustrated in figure 2.11, there are two compartments in this model: bulk liquid and biofilm. The biofilm is treated with two parts: liquid phase and solid matrix. The dissolved substances are transport in the liquid phase, meanwhile, different microorganic species, inert material and particulate substrate are included in the solid matrix. The particulate elements could attach to or detach from biofilm surface.

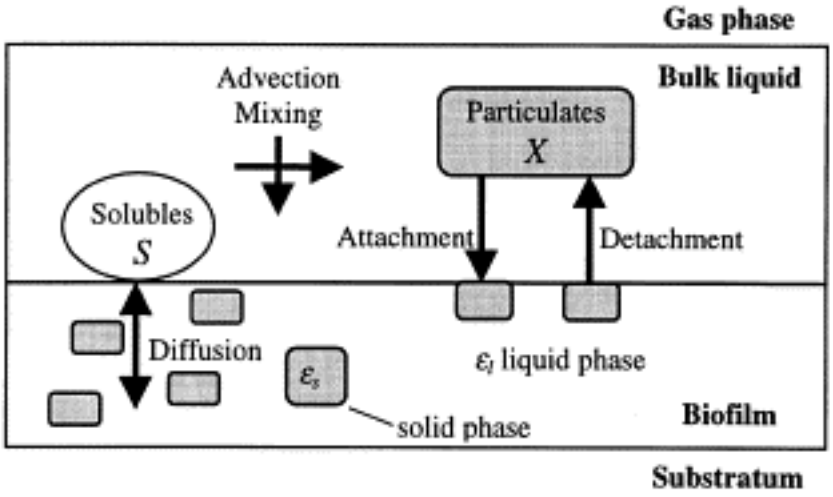

Figure 2.11. Ideal biofilm system in the simplified mixed-culture biofilm model [74].

This approach provided a quick estimation of competition within the biofilm. Besides, a transition-state model has been released to study the biofilm with mixed species, by including backwashing induced periodic detachment, it allows biofilm undergoes changeable conditions. Another feature is that all the bacteria can excrete soluble microbial products which could be utilized by heterotrophs [75]. This model almost contains the important characteristics of all previous models. The biofilm can reach a global steady state and biomass species distribution within the biofilm could be illustrated by this approach.

2.3.2 Multidimensional continuum biofilm models

One-dimension continuum models are simple but could be widely used to investigate biofilms when emphasis is put more on biofilm growth and related biochemical processes. However, biofilms are not one-dimension matters and their mechanism understanding is lacking. Therefore, multidimensional biofilm models have been established to capture the heterogenous structure of biofilm and expend research scope to include mechanical properties. Similar to previous work, some of the research continues to investigate the single- or multi-species biofilm growth, meanwhile, few studies focus more on the deformation of biofilm.

A three-dimension model for biofilm formation has been introduced by Eberl et al. in 2001 and the decoupled calculation in [74] was used for this system. Therefore, the bulk liquid region Ω_1 (without biomass) and solid biofilm region Ω_2 (with biomass) should be distinguished in this system. The nutrients transport by diffusion and convection in the bulk liquid region and would be consumed in the solid region. However, a density-dependent diffusion coefficient was adopted to calculate the nutrients transport in solid region to avoid instantaneous spreading of biomass. Numerical experiments for single species biofilm formation were performed by using this new spatio-temporal model, the results show that the irregular and rough biofilm morphology forms when the system is nutrient limited [76]. Later, the model has been applied to describe the antibiotic disinfection of biofilms in which the active and inert biomass were included [77]. Furthermore, the model was extended to illustrate a mixed-culture biofilm system consists of pathogenic and probiotic species [78]. In this case, the mixed biofilm grew in a laminar flowing channel and the probiotic biofilm could control the pathogens by changing the growth condition, such as local pH. Besides, the heterogenous biofilm structure such as finger-like and mushroom like biofilm have been modelled by Klapper et al. by defining the biofilm as a viscoelastic fluid material [59, 79, 80].

A finite element modelling of biofilm growth and deformation based on a material mechanics has been introduced by Hubert et al. [81]. In this case, the biomass grown in the form of aggregates. The biomass was modelled as an isotropic incompressible hyperelastic material, thus the density of the biomass body kept constant. Therefore, the expansion and deformation of the aggregate were driven by the material stress-strain relations. Besides, based on finite element method, a 2D fluid-structure interaction model for investigating the oscillation of biofilm streamer has been developed by Taherzadeh et al. [82]. As displayed in figure 2.12, the biofilm streamer consists of a circular biofilm base and oscillating tail with the measured dimensions from experimental work [23]. The connecting boundary between them is fixed and the tail is allowed to move freely with moving boundaries. The streamer tail is described by an

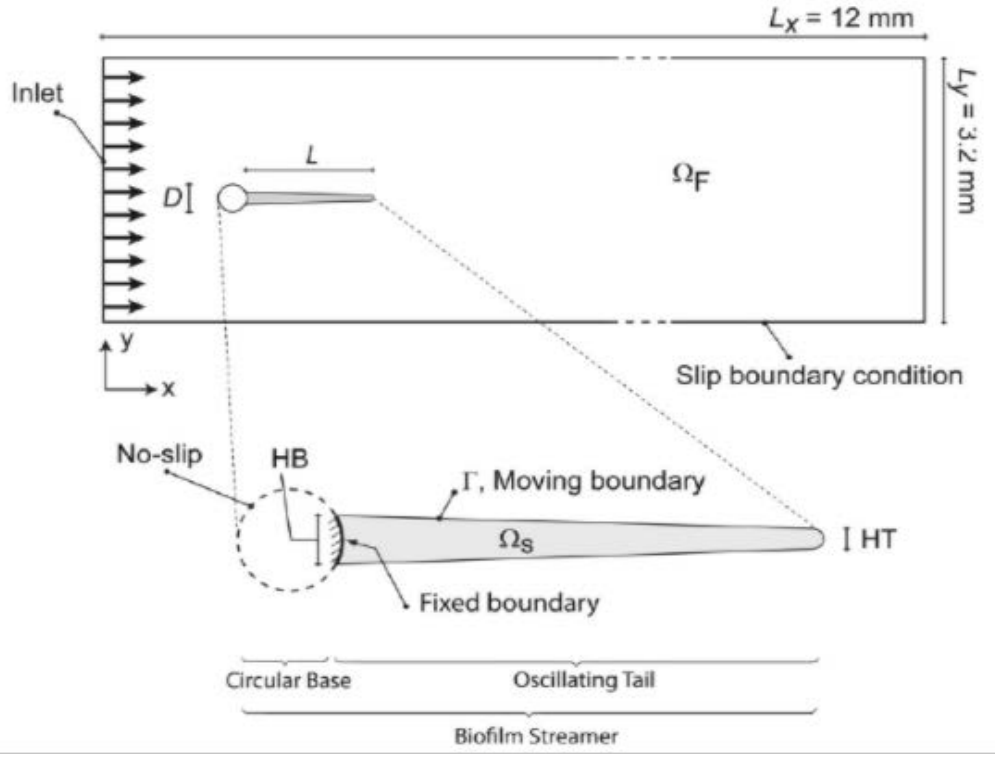

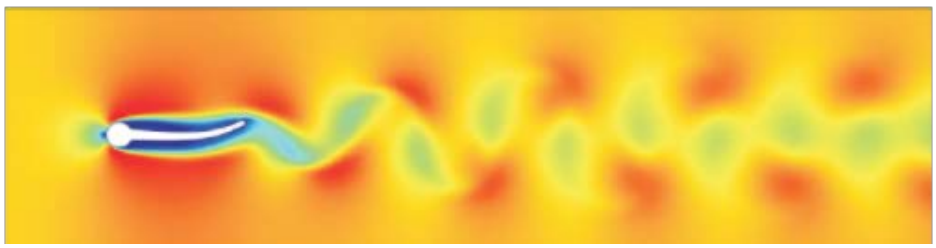

Figure 2.12. The description of the two-dimensional biofilm streamer model and its motion in the flow [82].

elastic materials model combined with a nonlinear elastodynamics model. Therefore, biofilm density, Young's modulus and Poisson's ratio are implemented as the input parameters to

calculate the deformation of the biofilm streamer. A uniform fluid flow is applied along the x-direction and solved by the incompressible Navier-Stokes' equations. The predicted oscillation amplitude of biofilm streamer under elevated fluid velocity agreed with the experiment measurement in the range of Reynolds number of 80-160. Furthermore, the oscillation of streamers with different lengths have been investigated as well. The results indicated the drag force increased with the length of biofilm streamer. The fluid-structure interaction between biofilm and moving fluid have also been investigated by using phase field method [83]. According to the first and second thermodynamics law, the energetics variational approach is adopted to model the fluid. The conservative and dissipative force are determined by the system energy. The bacterium is treated as a Newtonian fluid and the EPS is assumed to be a viscoelastic substance. The deformation and detachment of biofilm have been simulated, the results indicate the lower viscosity of EPS in the biofilm can cause the biofilm to bend and form biofilm streamer. Besides, biofilm with higher viscous ESP have greater resistance to deformation and detachment by the flow (figure 2.13).

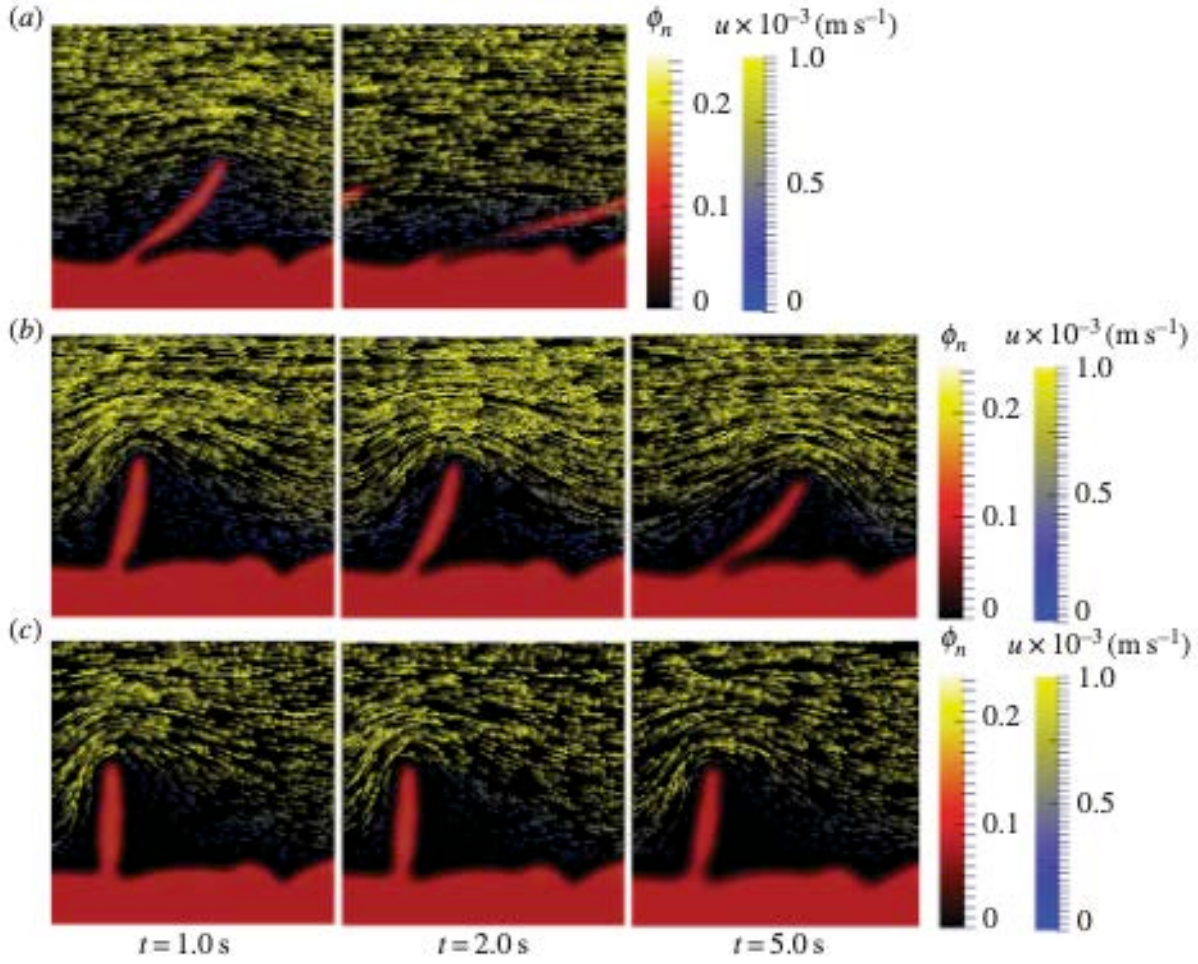

Figure 2.13. Biofilm deformation over time at flow velocity of 0.001 m/s. (a) EPS viscosity is 1 kg m^{-1} s^{-1}. (b) EPS viscosity is 10 kg m^{-1} s^{-1}. (c) EPS viscosity is 100 kg m^{-1} s^{-1} [83].

2.3.3 Discrete models of biofilm

Biofilm research based on discrete models started from 1990s [66]. As early as 1981, a metal-particle aggregation process was simulated by the diffusion-limited aggregation (DLA) approach [84]. Later, Fujikawa and Matsushita found that when the *Bacillus subtilis* spices grew at a low initial nutrient concentration, as show in figure 2.14A, the morphology of the biofilm was similar to the dendritic pattern in DLA model [85]. Inspired by these interesting experimental observations, the DLA model has been used to produce the dendritic biofilm growth pattern [86]. The key principle of this model is displayed in figure 2.14B: a seed particle was set as the origin of a square lattice on the plane, the biofilm growth was modelled by releasing another particle, this new particle is far from the origin and could move randomly. When it reaches the site adjacent to origin, it could be frozen in this site. Consequently, the branched structure of biofilm could be obtained by repeating this procedure as shown in figure 2.14C. The biofilm patterns predicted by this model appeared to be similar to the experimental observation; however, this graphic model did not include the biological processes since the bacteria grow through division.

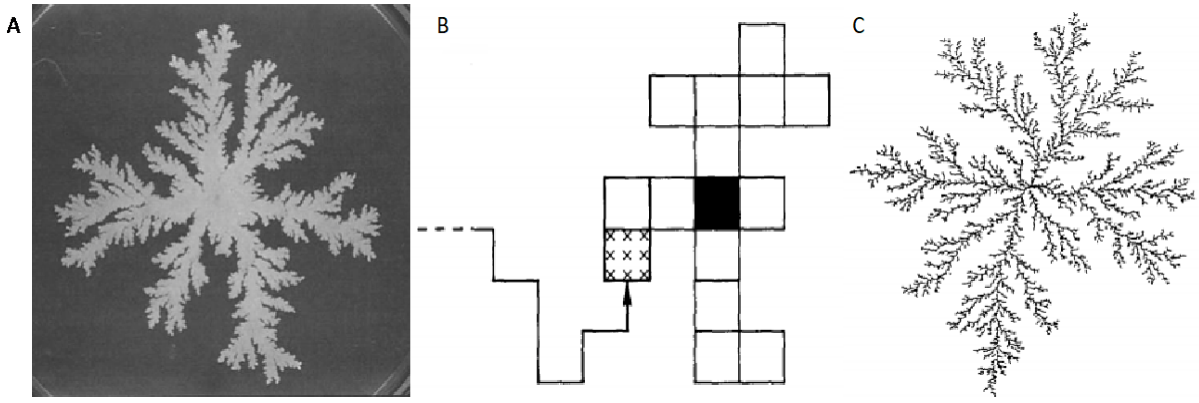

Figure 2.14. (A) A typical DLA-like colony patterns: *Bacillus subtilis* biofilm grew at initial nutrient concentration of 1 g/l for three weeks [85]. (B) 2D diffusion-limited aggregation growth model. (C) Computer simulation of a randomly branched structure which consists of 100000 particles [86].

Thereby, a simpler version of cellular automata (CA) model was introduced by Wimpenny and Colasanti [87] in which the bacteria division was taken into account. Different from the DLA model, the microbial cells replaced the seed particles in the CA model. Each cell could occupy a square lattice and reproduce itself to occupy the neighbouring square lattice. The growth of biofilm is controlled by the resource units which diffused with the same algorithm as the seed particles in DLA model. The microbial cell could search its neighbouring unoccupied squares and accumulate the resource units. When the resource units exceed the yield coefficient, a new

microbial cell could be produced. This model has been adopted to illustrate the specific biological issue, such as the biofilm growth at different nutrient concentration. However, there has no growth inside the biofilm since the substrate particles did not diffuse into the biofilm in this model. Therefore, this CA model has been further improved by considering more realistic bacteria growth [88]. In which case, the bacteria are modelled as walkers with location and internal energy, then internal energy decrease at a constant rate. The diffusion equation is adopted to solve nutrient diffusion in a triangular lattice. Walker can consume nutrient to increase internal energy, when the internal energy exceeds a threshold value, the walker would divide into two walkers. On the contrary, if the surrounding nutrient was not sufficient, the walker will be frozen there. The biofilm growth patterns driven by increased peptone level and agar concentration were shown in in figure 2.15.

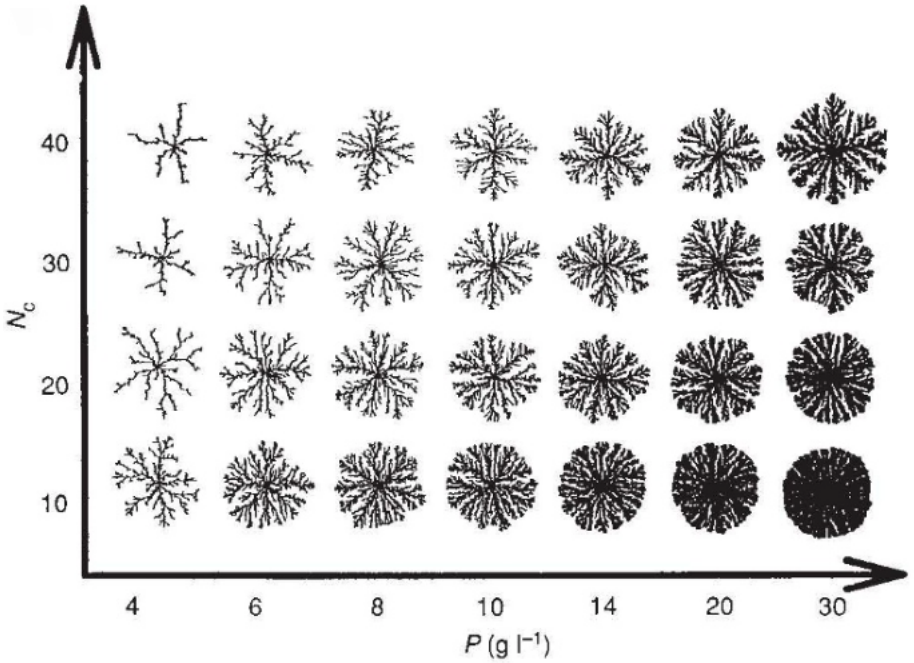

Figure 2.15. Generic modelling of biofilm growth patterns are organized as function of peptone level (P) and agar concentration (N_c) [88].

Later, a combined differential-discrete cellular automaton model was established by Picioreanu et al. to simulate the growth of biofilm [89]. Compare with other pioneer CA models, the main contribution of this model is the biological parameters, which commonly used in traditional biofilm models, such as growth rate and nutrient concentration, have been implemented in this hybrid model. Biomass density and substrate concentration were two main parameters to determine the state of this microbial system. The substrate concentration field is solved by using differential equations, whereas the biofilm growth is simulated by CA model [90]. As shown

in figure 2.16, the physical space (bacteria, polymers and carrier) has been divided into small compartments. An assumption for this model is the consumption of substrate will merely lead to the growth of biomass. When the biomass exceeds the maximum value, it will divide into two parts. One of them will stay at the same lattice, and the other one is treated as a new element and put in a randomly selected neighbouring lattice space. If there has no free site in adjacent space, the new cell will replace one of their neighbours, then the replaced neighbour needs to look for a free site in the same way. This model was applied to simulate biofilm growth attached on a solid surface, the biofilm morphology, density and porosity are automatically generated by the model as the output results [90].

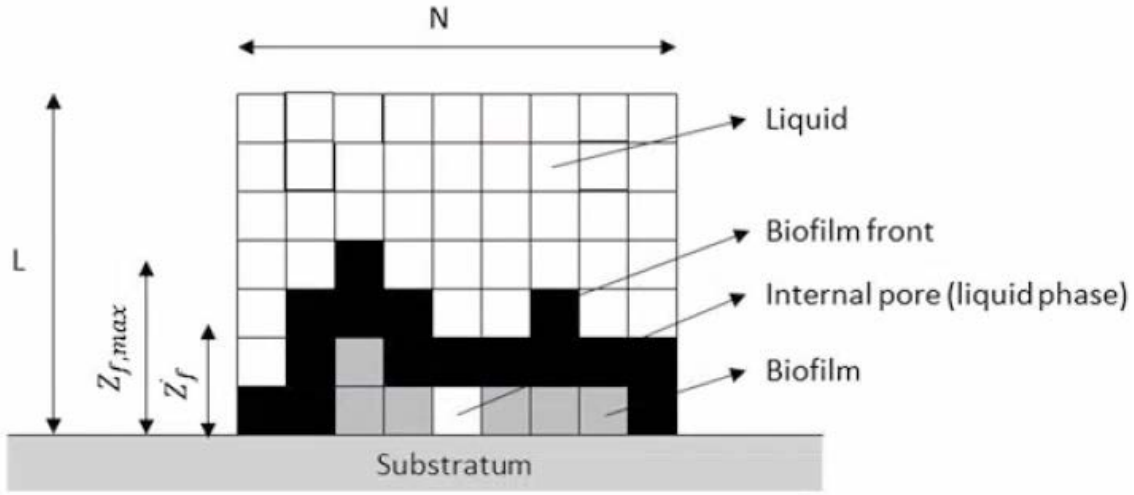

Figure 2.16. Construction of the hybrid cellular automata model, cells filled with biomass [91].

Afterwards, the model has been further extended by considering the fluid flow [92]. This fully quantitative multidimensional model (2D and 3D) can be utilized to describe the dynamic biofilm development and their highly heterogenous structures. The fluid field was firstly calculated by solving the Navier-Stokes equations to obtain the fluid velocity and pressure:

$$\nabla \cdot \mathbf{u} = 0 \tag{2.8}$$

$$\frac{\partial \mathbf{u}}{\partial t} + \mathbf{u} \cdot \nabla \mathbf{u} = -\frac{1}{\rho} \nabla P + \upsilon \nabla^2 \mathbf{u} \tag{2.9}$$

where $\mathbf{u}$ is the vector fluid velocity, ρ and υ are fluid density and kinematic viscosity. Secondly, the captured velocity is used to resolve the substrate diffusion:

$$\frac{\partial C_s}{\partial t} + \mathbf{u} \cdot \nabla C_s = -R_s(C_s, C_x) + D \nabla^2 C_s \tag{2.10}$$

where C_s is the substrate concentration, C_x is the concentration of biomass, R_s is the consumption rate of substrate and D is the nutrient diffusion coefficient. Afterwards, the biomass growth was calculated by a kinetic model:

$$\frac{\partial C_x}{\partial t} = R_x(C_s, C_x) \tag{2.11}$$

where R_x is the biomass formation rate. Then biomass spreading is solved by the cellular automata approach which has been introduced in [89]. Before biomass redistribution, the biofilm deformation energy, which induced by the shear stress acting on the biofilm surface, was calculated to determine the break point. It should be noted that there is a significant separation of time scales during biofilm development. The time scale of biological processes including biofilm growth and biofilm decay ranges from hours to days, the substrate could transport in the scale of minutes, while the hydrodynamic process happens in seconds [92]. Therefore, to reduce the computational time, each process is solved by assuming the others are at steady state [66]. In addition, an extension of this hybrid model has been presented by Picioreanu et al. to study the fluid shear induced biofilm erosion and sloughing, in which biofilm is modelled as an isotropic elastic material [93]. In this model, the laminar flow should be analysed by incompressible Navier-Stoke equations before biofilm breakup. Then the normal and tangential fluid shear stresses could be provided to calculate the equivalent stress, biofilm detachment occurs when the calculated equivalent stress is greater than the cohesion strength, which is defined as internal stress to resist the tensile stress. An assumption for biofilm detachment process is the detached biomass disappear from the system immediately, that is, the grid cells which comprise detached biomass will only have liquid inside after detachment. Therefore, the model didn't allow the illustration of biofilm reattachment and the secondary detachment of detached biofilm flocs.

2.3.4 Individual based biofilm models

Individual based model (IbM, also known as agent-based model) is widely used to simulate a complex system of populations, such as the modelling of forest succession and animal populations [94]. Broadly speaking, IbM is also a type of discrete element modelling. Since the independent individuals in the model are allowed to have their own behaviour and can interact with each other, this modelling approach has been addressed to describe the microbial system-biofilm. BacSim is the first two-dimensional agent-based model to simulate the growth of biofilm [95, 96]. Bacteria are represented as circles in the model and more realistic biological processes, such as cell division, death, metabolism, maintenance and substrate uptake were

included. Later, BacSim was updated to version 2 and introduced in [18]. The improved model is a quasi-3D model since the depth of the simulation domain is kept at a small value equals to twice the bacteria diameter. Therefore, the bacteria are represented as spheric particles (3D) while the 2D lattice is used to solve the diffusion-reaction of substrates. Similar to the biomass-based model (BbM) in [89], biofilm growth is assumed to be the result of diffusion, reaction, bacteria growth, division and spreading. Bacteria cells grow by consuming the nutrient and divide when the volume reaches the maximum value. A minimum distance is set among the cells to shove the growing bacteria cells to obtain the new morphology of biofilm. In order to have a comparison, the same input parameters are adopted into IbM. In principle, the results agree with the outputs of BbM, but the details of biofilm morphology and the growth of minority species are different [18]. Therefore, the IbM may be better for investigating the biofilm system within multispecies or biofilm growth in small scale since it allows individual variability and requires high computational effort [66]. In order to overcome this drawback, a scaled-up model termed particle-based model has been established to describe the biofilm system with large-scale heterogeneity [19]. Then basic idea of this model is to replace the small size bacteria agents with super-particles, the diameter of those large particles is around 10-20 μm and the principle of biomass spreading is inherited from the previous model of Kreft et al. [18, 95, 96]. This model could present the biofilm with multispecies by using different type of active biomass in the system, and only one type of inert biomass is taken into account. Thus, each particle consists of one type of active biomass and a fraction of inert biomass. The density of particle is constant in this particle-based model. Therefore, the particle size increases with the growing biomass. When the mass reaches the maximum value, the particle will divide into to daughter particles and the biomass is transferred unevenly. Besides, similar to one-dimensional modelling [71], a simple biomass detachment is implemented in some cases: the thickness of the biofilm could be set as constant, then the particles which move out of this limitation will be removed from the simulation domain [19]. Effectively, the particle-based model is the scaled-up version of traditional individual based model, therefore, it allows to model the heterogeneity of biofilm at large-scale.

In addition, to investigate how the biofilm structure is affected by the EPS, the BacSim is extended to allow the production of EPS. EPS are initially generated as a shell around the bacterial particles and then excrete as cell-sized particle into the system [20]. The numerical simulation found that the production of EPS reduced the growth of producers but accelerated the growth of non-producers. Later, an individual model which combines all those approaches

have been introduced to explain the structure of multispecies biofilms [97]. In this model, the changes in cells are not only due to biomass growth but also the biomass decay, where the biomass decay will reduce the size of the biomass cells. Thus, the division happens when the radius of cells exceeds a threshold value. This framework is extended to describe biofilm erosion and sloughing by using an empirical detachment speed function without the requirement of mechanistic model. Compared with the detachment model in [93], this simplified detachment model could save the computational time and cost with numerical efficient [98]. Furthermore, EPS have been also modelled as a continuum field in [99]. Meanwhile, the microbial cells are simulated by using discrete element method and can interact with the continuum entities. That is, bacteria are embedded in their EPS matrix. The EPS is treated as a viscous fluid, and EPS region could expand by releasing the pressure which is produced by the biomass growth. On the contrary, the EPS region will shrink when biomass decay occurs. Cell spreading here is caused by the global advection (Darcy's law) and particle shoving. This model was applied to describe the consolidation of biofilm and the microbial colonies growth in EPS matrix. However, the model could be refined because of the lack of experimental data, such as the kinetics parameters of EPS formation and the mechanical properties of EPS matrix [99].

Later, an open-source software named 'individual-based Dynamics of Microbial Communities Simulator'(iDynoMiCS) has been introduced by Lardon et al. [100]. Most features of previous work have been merged in iDynoMiCS and was used to simulate the growth of microbial system by using individual microbes. This advanced model allows to study the interaction among new types of agents, such as archaea, protozoa, algae and fungi. In addition, EPS excretion process has been improved. The produced EPS is continuously transported into environment and distributed to the neighbouring EPS particles which have a radius smaller than the certain radius. If there are no EPS particles nearby, then a new EPS particle will be created. Besides, based on the smoothed particle hydrodynamic methods [101], the small size EPS particles are used to recreate a viscous fluidic biofilm matrix, which is an alternative to the continuum treatment in [99]. Recently, a mechanistic individual-based model developed at Newcastle University (NUFEB) has been introduced by Jayathilake et al. [102]. This model was developed based on the open-source software: Large-scale Atomic/Molecular Massively Parallel Simulator (LAMMPS). The biological processes such as bacteria growth, division, decay and the diffusion and reaction of nutrient are established and implemented as a package of LAMMPS. Besides, the model allows physical interaction among the individual particles.

Therefore, the EPS adhesion force, contact force and shear induced biofilm detachment could be described. Additional thermodynamic principles are applied to simulate biofilm growth and the growth yield is estimated by the chemical energy [103].

The NUFEB modelling framework is presented in figure 2.17. A representative volume element was chosen from the large system which need to be studied. Then the partial differential equations were used to discretize the environment of the volume element, spherical individual cells were represented in this space. Three functional group of microorganisms including heterotrophic bacteria, ammonia oxidizing bacteria and nitrite oxidizing bacteria have been considered in the model. Each agent in different group has species-dependent rules and kinetics. Bacteria grow and divide by consuming nutrient from the environment, the extracellular polymeric substance is produced by heterotrophic bacteria. Physical interactions among the particles are adopted by using Hertzian or spring models [102]. The details of biological process and mechanical interactions in this model would be introduced in chapter 3. The individual-based models have the capacity to predict dynamics in complex systems since the microorganism system is heterogeneous and stochastic [104]. However, there are still some limitations about IbM. For example, it is very computationally expensive when simulate large-scale microbial systems. It is tricky to get accurate modelling parameters for individual cells from experimental measurements [104].

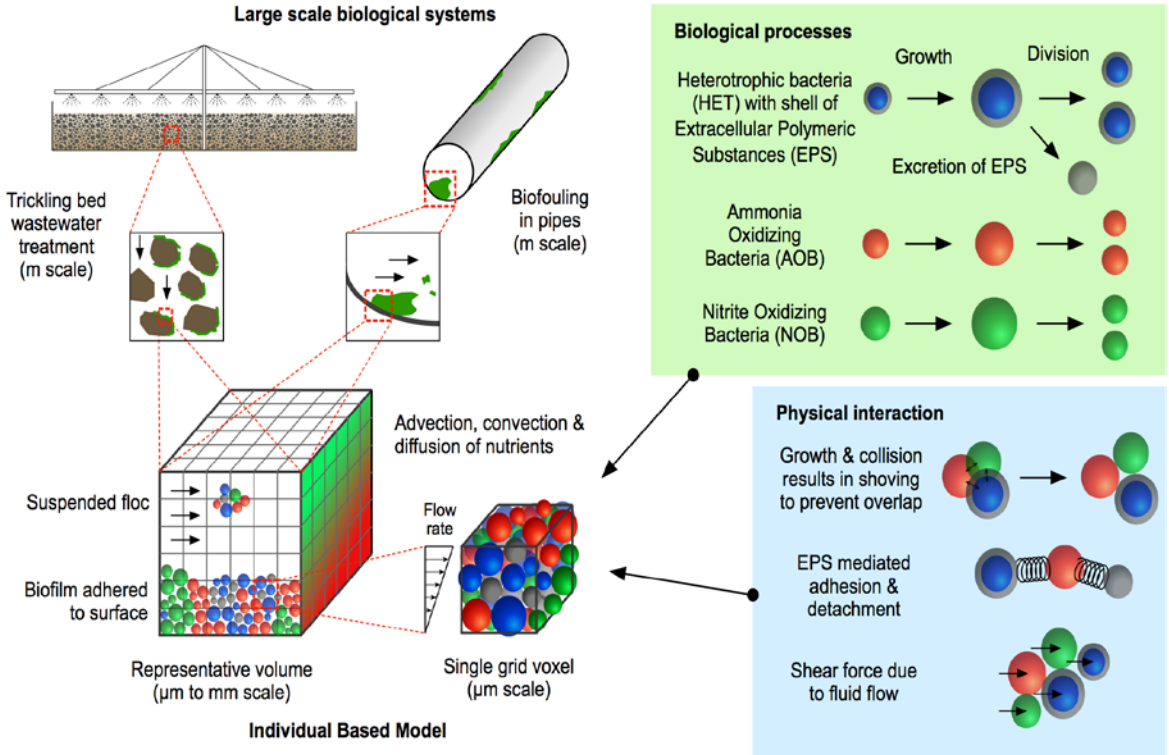

Figure 2.17. Summary of individual-based modelling (NUFEB) [102].

2.4 Mechanical properties of biofilms

Knowing the mechanical properties of biofilm, such as elastic modulus, shear modulus and cohesive strength, allow better understanding of biofilm system. Biofilm structure and the mechanical stability could be determined by those physical properties. A lot of work has been done to measure these mechanical properties; however, there is big variation of the results which depends on the microbial species and experimental approaches. Mechanical properties of biofilms are dominant factors for the biofilm deformation and detachment in the fluid flow.

2.4.1 Viscoelasticity of biofilms

A number of studies suggested that biofilms often behave as viscoelastic material [13, 54, 105, 106]. These experiments demonstrated that biofilms exhibit an instantaneous elastic response and a time-dependent viscous deformation. In addition, results from flow cell experiments show a residual strain which is completely irrecoverable during biofilm relaxation [15, 54, 107]. Viscoelasticity is time-dependent mechanical property of a material, which contains both elastic (solid) and viscous (fluid) characteristics [108]. Figure 2.18 displays the typical stress-strain curves of elastic and viscoelasticity. For an elastic material, when a stress is applied, it deforms immediately and would return to its original shape once the stress is removed (Figure 2.18A). Thus, the loading and unloading curves are superimposed. However, in case of viscoelastic material, these two curves are not coincident due to the energy loss which dissipates in the form of heat [109]. Hence a hysteresis loop is formed during loading and unloading (shaded in Figure 2.18B). The area of the loop is equal to the amount of energy loss [110].

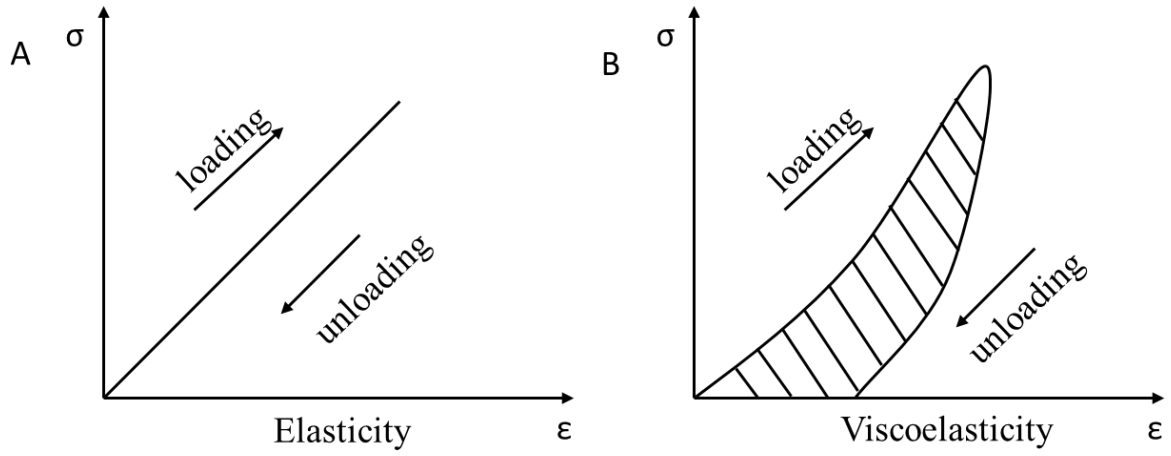

Figure 2.18. Typical stress-strain curves of elasticity and viscoelasticity.

The creep-recovery and stress relaxation tests are especially useful to test the viscoelastic characteristics. In the creep-recovery test, a constants stress is applied and maintained for a period of time and then remove the stress. As shown in figure 2.19, the viscoelastic material is subjected to a constant stress during the time from t_0 to t_1, which causes a time-dependent increase in strain (creep). After the force is removed, the material will recover the deformation continuously (recovery). For the viscoelastic solid materials, a complete recovery could be achieved overtime (Figure 2.18A and 2.19A), this kind of materials have been widely used as vibration isolation and noise damping. However, in case of viscoelastic fluid materials, the recovery would not be complete due to the irreversible viscous deformation (Figure 2.18B and 2.19B) [111]. In the stress relaxation test, the material was strained initially, by holding this constant strain, a decrease in stress could be observed overtime.

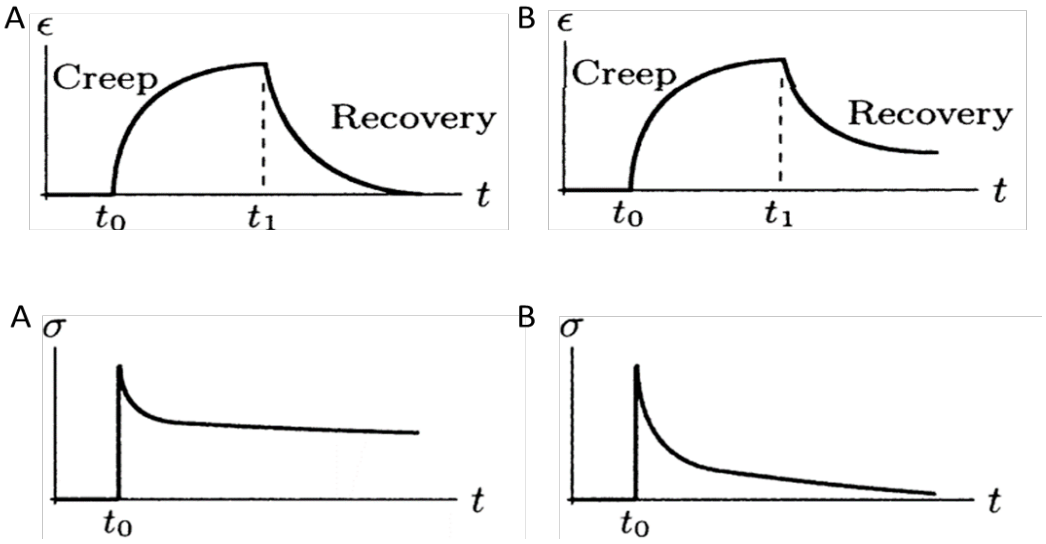

Figure 2.19. (A) and (B) show the strain ε response to an applied constant stress σ of the viscoelastic solid material and viscoelastic fluid material. The stress is applied at time t_0 then removed at time t_1. (C) and (D) shows the stress relaxation test of the viscoelastic solid material and viscoelastic fluid material [112].

A wide range of techniques has been adopted to measure the viscoelastic properties of biofilm. For example, the uniaxial compression (figure 2.20(a)) has been carried out to measure bulk properties of biofilm [14, 113]. In these experiments, the force required for biofilm compression is measured, and the apparent Young's modulus could be determined from the slope of the force-displacement curve. In addition, the compression test could also be performed by using microindentation method (figure 2.20(e)), in which the mechanical properties of biofilm could be measured at microscale [55, 114]. In the microindentation experiment, a known force is

applied at the biofilm surface with an indenter, the indenter compresses the biofilm gradually and locally to obtain the stress-strain curve [115]. However, the main drawback of the compression test is that the normal compressive force is not the most relevant loading which biofilms undergo in nature environment [111]. In nature, most biofilms expose to various degrees of hydrodynamic conditions [116]. Therefore, the shear stress seems to be the relevant loading which a biofilm is most likely to undergo. Rheometer has been commonly used to investigate viscoelastic properties of biofilm (figure 2.20(b)) [117, 118]. Creep test could be conducted by applying a shear stress and monitoring the resulting strain, relaxation test could performed by applying a strain and measuring the shear stress [111]. The flow cell (figure 2.20(c)) has also been employed to deform biofilm with controlled flow with the biofilm deformation captured by microscope or OCT [16, 55, 58, 59]. In the flow shear stress experiment, the biofilm grown under steady flow and then experience a fluctuational shear stress by changing the flow velocity. The flow cell is simple and cheap to operate and could be used to capture the simple stress-strain curve [111]. Atomic force microscopy (figure 2.20(d)) is also a well-known technique which could be applied to quantify the adhesion force between cells, cells and surface [119]. The adhesion and cohesion energy of biofilm have been measured by using AFM [120, 121].

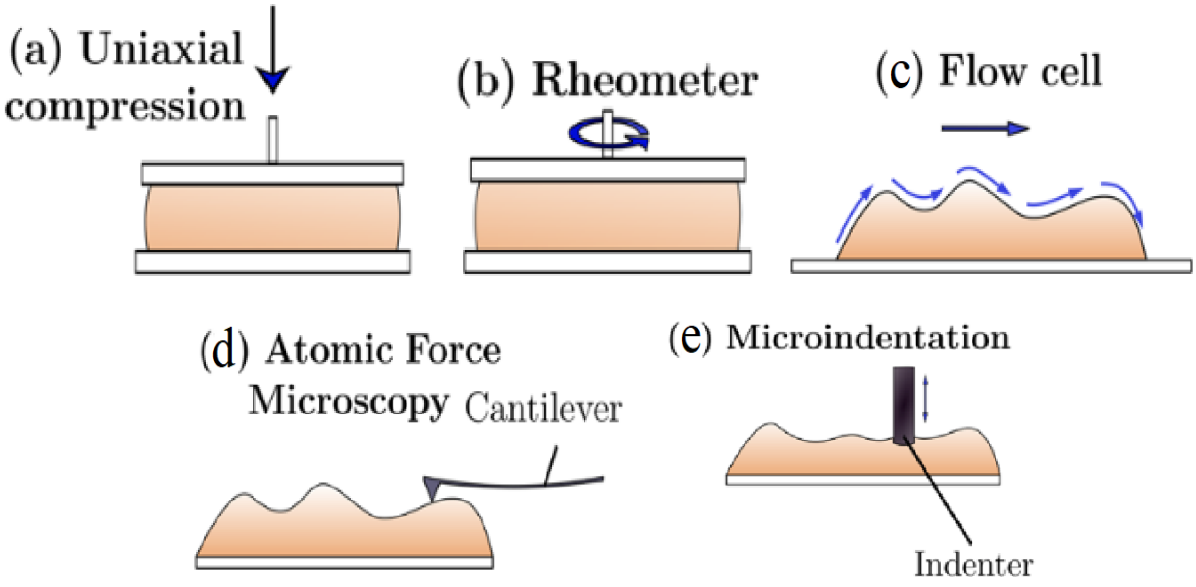

Figure 2.20. The method of measuring the mechanical properties of biofilm. (a) Uniaxial compression test, (b) shear stress in a rheometer test, (c) flow-cell method, (d) atomic force microscopy-nanoindentation test, (e) microindentation test [115].

The main results of biofilm mechanical properties using different methods are displayed in Table 2.1. Different viscoelastic models could be adopted to extract the viscoelastic parameters of biofilms. Some commonly used viscoelastic models have been explained as follows.

Table 2.1 Summary of reported biofilm mechanical properties with different measurements [111, 122].

	Measurement method	Range of the value	Reference
Young's modulus	Uniaxial compression	6000-50000 Pa	[14, 113]
	Fluid cell	0.69-353 Pa	[16, 54, 59, 123, 124]
Shear modulus	Fluid cell	1.1-280 Pa	[15, 16, 54]
	Rheometer	0.6-1600 Pa	[117, 118]
Viscosity	Fluid cell	3500-190000 Pa·s	[15, 16]
	Rheometer	10-500000000 Pa·s	[105, 125, 126]
Cohesive energy	Atomic force microscopy	0.0001-0.0021 Pa	[120]
Adhesive force	Atomic force microscopy	0.39-8.12 nN	[121]

2.4.2 Models of viscoelasticity

For a linear elastic material, stress σ is proportional to strain ε:

$$\sigma = E\varepsilon \tag{2.12}$$

where E is the elastic modulus. However, for fluids, stress is a function of strain rate which can be expressed as:

$$\sigma = \eta \frac{d\varepsilon}{dt} \tag{2.13}$$

where η is the viscosity of the material which defined as the resistance to flow [127]. Therefore, the liquid with higher viscosity is more difficult to deform. Since the viscoelastic material has both elastic and viscous properties, thus it could be described by the model which combines spring and dashpot.

Kelvin-Voigt and Maxwell model are commonly used simplest constitutive models for viscoelastic materials. A spring connected in parallel with a dashpot in the Kelvin-Voigt model, therefore, the strain experienced by the spring is the same with the strain experienced by the dashpot (Figure 2.21A):

$$\varepsilon = \varepsilon_E = \varepsilon_\eta \tag{2.14}$$

while the total stress is the sum of the stresses applied on spring and dashpot:

$$\sigma = \sigma_E + \sigma_\eta \tag{2.15}$$

Substituting equation (2.12) and (2.13) into equation (2.15), the stress in Kelvin-Voigt model could be expressed as:

$$\sigma = E\varepsilon + \eta \frac{d\varepsilon}{dt} \tag{2.16}$$

For the simplest Maxwell model, a spring connected in series with a dashpot, both spring and dashpot are subjected to the same stress with independent strain (Figure 2.21B):

$$\varepsilon = \varepsilon_E + \varepsilon_\eta \tag{2.17}$$

$$\sigma = \sigma_E = \sigma_\eta \tag{2.18}$$

Therefore, the strain rate in Maxwell model could be expressed as:

$$\frac{d\varepsilon}{dt} = \frac{1}{E}\frac{d\sigma}{dt} + \frac{\sigma}{\eta} \tag{2.19}$$

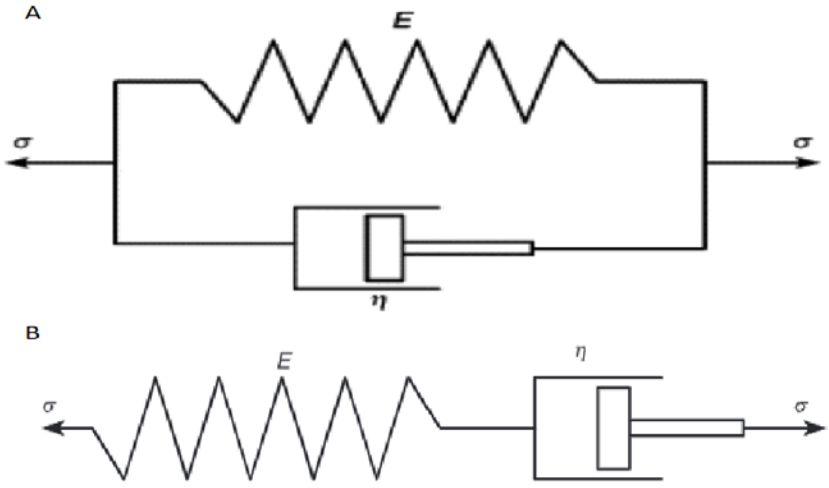

Figure 2.21. The schematic diagram for (A) Kelvin-Voigt model and (B) Maxwell model [128].

When a stress is applied, the spring and dashpot in Kelvin-Voigt model cannot deform independently since the spring is restricted by the dashpot. Therefore, the spring would not return to its original position immediately during relaxation [128]. However, in the Maxwell model the spring extends immediately since the two elements have independent strain. Therefore, the model has an unlimited deformation as time increase when a stress is applied, it

is not real for the viscoelastic material [128]. Theoretically, the complex model, which combines Kelvin-Voigt and Maxwell model such as generalized Kelvin-Voigt, Maxwell model and Burgers model, could potentially describe the viscoelasticity more accurately. But it will require a number of fitting parameters [129].

3 The development of individual based modelling

3.1 Introduction

In this chapter, the details of individual based models have been illustrated. The biofilm modelling was initially developed as one-way individual-based biofilm modelling (NUFEB model), then extended to two-way coupled model. The difference between those two models is the treatment of fluid flow. In the one-way modelling, the fluid flow is described by a simplified drag model which is based on Stokes flow passing a sphere. In other words, the agents can be moved by the fluid shear force but not affecting the flow pattern. This modelling is computational efficient and is still useful to understand the flow induced biofilm deformation and detachment when the detailed flow patterns are not of concerns. When the flow patterns around the biofilm are becoming important, the individual-based biofilm modelling (NUFEB model) has been improved by coupling it with a computational fluid dynamic model. This will then enable studying the interactions between the flow and biofilms.

3.2 Individual-based modelling of biofilm

The NUFEB model presented here is the first step towards the development of a comprehensive IbM which integrates biology, chemistry and physics to enable the prediction of the emergent properties of a wide range of bacterial communities [102]. This model combines biological processes with mechanical interactions between individual bacteria, bacteria-EPS and EPS-EPS. This IbM model has been implemented in the mechanically sophisticated Large-scale Atomic/Molecular Massively Parallel Simulator (LAMMPS), which is an open-source C++ molecular dynamics (MD) code developed by Sandia National Laboratories (http://lammps.sandia.gov/). LAMMPS has been widely adopted to simulate atoms or, more generally, as a parallel particle simulator at different length scales for a wide range of non-living materials (e.g. metals, semiconductors, polymers) [130-132] due to its parallel, modular and extensible nature. However, it has never been employed to simulate microbial communities until the presence of NUFEB model.

The IbM model implemented in LAMMPS consists of two types of sub-model: the biological sub-models which deals with biological processes (growth, division, decay, death), and the physical sub-models which handle physical processes (adhesion, contact, detachment) [102]. This 3D model allows the simulations of both single- and multi- species biofilm growth and their response to a given fluid shear force. In the individual based model, a micro-scale

Cartesian box could be defined as the simulation domain with length, width and depth. The simulation box is divided into Cartesian grid elements ($\Delta x \times \Delta y \times \Delta z$), each element has the local nutrient concentration and fluid flow velocity. In this model, both EPS producers and non-EPS producer bacteria were considered. For example, three typical types of bacteria in wastewater were modelled: Heterotrophic bacteria (HET), Ammonia Oxidizing Bacteria (AOB) and Nitrite Oxidizing Bacteria (NOB). Besides, EPS which produced by heterotrophic bacteria and dead cells (I) are also considered in this model. The bacterial cells are represented as spherical particles, each individual contains their own mass, radius, type and location [102].

The bacteria are placed in the simulation box randomly with a set of initial nutrient concentrations. Then the growth and division of bacterial cells are calculated, and the nutrient concentration is updated due to nutrient consumed by bacteria. Overlap among particles will be generated after bacteria growth and division. In the previous modelling work [18], a minimum distance was applied between neighbouring cells to minimize the overlap during growth. While, in NUFEB model the shoving of the cells is resolved in a mechanical way. Residual stress within the biofilm generates with the emergence of overlaps, then the location of the particles will be updated to release the stress to achieve the new mechanical equilibriums in the system. As explained in literatures [93, 133], the time scales of biological process, substrate transport and hydrodynamic processes are totally different. Therefore, in this model, each process is executed sequentially by assuming the other processes are at the steady stage. The pseudocode is shown below:

Set initial condition for bacterial cells: number of the particles with ID, type, density, location and radius.

Set the initial nutrient concentration in the simulation box.

1. Biomass growth and decay, the growth rates are determined from the local substrate concentration.
2. The local nutrient concentration is calculated by using diffusion-reaction equation.
3. EPS production and bacterial cells division.
4. Biomass spreading by mechanical relaxation, the positions of the cells are updated when the system reaches the new mechanical equilibrium.
5. Go back to step 1 and reiterate the steps above.

Those sub-models and related equations described in detail below.

3.2.1 Growth and decay of bacterial cells

The growth of the bacterial cells is calculated by following equation:

$$\frac{d_{m_i}}{d_t} = \mu_i m_i \tag{3.1}$$

where m_i is the mass (kg) of the bacterial cell and μ_i is the growth rate (s^{-1}). Then the growth formula is further described with the Monod kinetic equation which is a mathematical model for the microorganisms' growth [134]:

$$\mu_i = \mu_{max} \frac{S}{S+K_S} \tag{3.2}$$

where μ_{max} is the maximum specific growth rate, S is the concentration of available substrate (kg m^{-3}), the substrate affinity K_S (kg m^{-3}) refers to the substrate concentration at $\mu_i = \frac{1}{2}\mu_{max}$. u_{max} and K_S are empirical constants which are determined by the microbial species and growth conditions. Substitute the equation (3.2) into equation (3.1), the bacterial growth equation is given by:

$$\frac{d_{m_i}}{d_t} = u_{max} \frac{S}{S+K_S} m_i \tag{3.3}$$

In this model, biofilm decay is assumed to be the first order kinetics (constants) and includes the maintenance rate. The growth and decay rates for different functional groups are listed in table 1. For the functional biomass group i (i = HET, AOB, NOB, EPS and I), $\mu_{m,i}$ is the maximum specific growth rate and b_i is the decay rate. S_j is the nutrient concentration for soluble component j (j = S, NH_4, NO_2, NO_3, O_2). η_H is the reduction factor for heterotrophs during anoxic growth. $K_{j,i}$ is the affinity constant between the nutrient j and biomass group i.

Table 3.1 Growth and decay rates for Heterotrophic bacteria, Ammonia Oxidizing Bacteria, Nitrite Oxidizing Bacteria, Extracellular Polymeric Substance and Dead cells.

Process	**Rate (1/s)**	
Aerobic growth of HET	$\propto_{m,HET} \frac{S_S}{K_{S,HET}+S_S} \frac{S_{O2}}{K_{O2,HET}+S_{O2}}$	R_1
Aerobic growth of AOB	$\propto_{m,AOB} \frac{S_{NH4}}{K_{NH4,AOB}+S_{NH4}} \frac{S_{O2}}{K_{O2,AOB}+S_{O2}}$	R_2
Aerobic growth of NOB	$\propto_{m,NOB} \frac{S_{NO2}}{K_{NO2,NOB}+S_{NO2}} \frac{S_{O2}}{K_{O2,NOB}+S_{O2}}$	R_3
Anoxic growth of HET on NO_3	$\eta_H \propto_{m,HET} \frac{S_S}{K_{S,HET}+S_S} \frac{S_{NO3}}{K_{NO3,HET}+S_{NO3}} \frac{K_{O2,HET}}{K_{O2,HET}+S_{O2}}$	R_4
Anoxic growth of HET on NO_2	$\eta_H \propto_{m,HET} \frac{S_S}{K_{S,HET}+S_S} \frac{S_{NO2}}{K_{NO2,HET}+S_{NO2}} \frac{K_{O2,HET}}{K_{O2,HET}+S_{O2}}$	R_5
Decay of HET	b_{HET}	R_6
Decay of AOB	b_{AOB}	R_7
Decay of NOB	b_{NOB}	R_8
Decay of EPS	b_{EPS}	R_9
Decay of Dead	b_I	R_{10}

The nutrient concentrations, which used to calculate the growth rate in table 1, are the local nutrient concentration in the Cartesian grid element where the bacterial cell occupies. Therefore, the total growth/decay for each particulate component could be expressed as [102]:

$$\frac{dm_{HET}}{dt} = [(R_1 + R_4 + R_5) - (R_6)]m_{HET} \quad (3.4a)$$

$$\frac{dm_{AOB}}{dt} = [(R_2) - (R_7)]m_{AOB} \quad (3.4b)$$

$$\frac{dm_{NOB}}{dt} = [(R_3) - (R_8)]m_{NOB} \quad (3.4c)$$

$$\frac{dm_{eps\_H}}{dt} = \frac{Y_{eps}}{Y_{HET}}(R_1 + R_4 + R_5)m_{HET} \quad (3.4d)$$

$$\frac{dm_{eps}}{dt} = -R_9 m_{EPS} \quad (3.4e)$$

$$\frac{dm_I}{dt} = -R_{10} m_I \quad (3.4f)$$

m_{EPS_H} is EPS bound to HET bacteria, Y_{eps} and Y_{HET} are EPS formation coefficient and yield coefficient for HET growth. The Bacterial cells shrink when the system is nutrient-limited. Those shrinking cells will become dead agents with the diameter of the cell reduce to a user-specified minimum diameter. Their type will be changed to the dead type (I) and their biomass will convert to substrate to feed other agents.

3.2.2 Nutrient mass balance

The nutrient is treated as a continuous medium in our individual based modelling. For each soluble component (S, NH_4, NO_2, NO_3, O_2) in the simulation box, the mass balance of nutrient is solved by using the advection-diffusion-reaction equation:

$$\frac{\partial S}{\partial t} + \vec{U} \cdot \nabla S = D\nabla^2 S + R \quad (3.5)$$

$$D\nabla^2 S = D\ \frac{\partial^2 S}{\Delta x^2} + D\ \frac{\partial^2 S}{\Delta y^2} + D\ \frac{\partial^2 S}{\Delta z^2} \quad (3.6)$$

where *t* is the time (s^{-1}), *D* is the effective diffusion coefficient ($m^2\ s^{-1}$), *R* is the nutrient uptake rate ($kg\ m^{-3}\ s^{-1}$).

As shown in figure 3.1A, the substrate concentration in the bulk liquid layer is constants, it was separated from the biofilm with the boundary layer, and the nutrient will be transported into biofilm by diffusion [18], according to the initial value of the nutrient concentration which can be set by the operator, the concentration level in next time step can be obtained by discretising the diffusion-reaction equation. As illustrated in figure 3.1B, equation (3.5) has been discretized on a Marker-And-Cell (MAC) uniform grid, the dimension of the grid ($\Delta x \times \Delta y \times \Delta z$) in the simulation box could be defined by the user. The nutrient concentration at the centre of the grid is *S*, based on the Forward Euler method and Central finite difference method, discretized equations could be expressed as:

$$\frac{S_{i,j,k}^{n+1}-S_{i,j,k}^{n}}{\Delta t}+\frac{Ux_{i+\frac{1}{2},j,k}+Ux_{i-\frac{1}{2},j,k}}{2}\cdot\frac{S_{i+\frac{1}{2},j,k}^{n}-S_{i-\frac{1}{2},j,k}^{n}}{\Delta x}+\frac{Uy_{i,j+\frac{1}{2},k}+Uy_{i,j-\frac{1}{2},k}}{2}\cdot\frac{S_{i,j+\frac{1}{2},k}^{n}-S_{i,j-\frac{1}{2},k}^{n}}{\Delta y}+$$
$$\frac{Uz_{i,j,k+\frac{1}{2}}+Uz_{i,j,k-\frac{1}{2}}}{2}\cdot\frac{S_{i,j,k+\frac{1}{2}}^{n}-S_{i,j,k-\frac{1}{2}}^{n}}{\Delta z}=D_{i+\frac{1}{2},j,k}\cdot\frac{S_{i+\frac{1}{2},j,k}^{n}-2S_{i,j,k}^{n}-S_{i-\frac{1}{2},j,k}^{n}}{\Delta x^{2}}+D_{i,j+\frac{1}{2},k}\cdot$$
$$\frac{S_{i,j+\frac{1}{2},k}^{n}-2S_{i,j,k}^{n}-S_{i,j-\frac{1}{2},k}^{n}}{\Delta y^{2}}+D_{i,j,k+\frac{1}{2}}\cdot\frac{S_{i,j,k+\frac{1}{2}}^{n}-2S_{i,j,k}^{n}-S_{i,j,k-\frac{1}{2}}^{n}}{\Delta z^{2}}+R \tag{3.7}$$

The time of diffusive substrate transfer is much faster than the bacterial growth, therefore, the transported concentration becomes steady soon, then this value could be used in equation (3.3) to calculate biofilm growth rate.

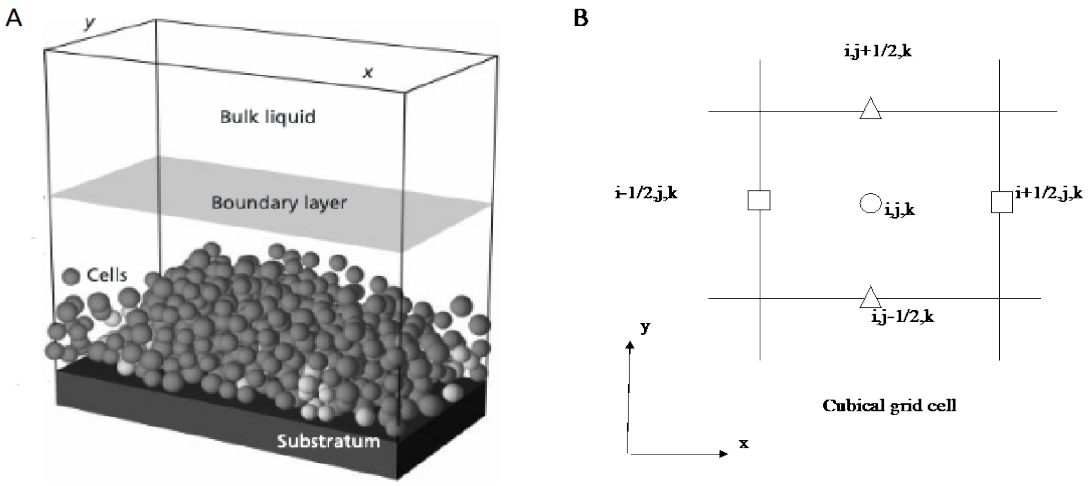

Figure 3.1. (A) Schematic of the nutrient diffusion [18] and (B) Marker-And-Cell (MAC) scheme [102].

When solve nutrient concentration transport equation, the effective diffusion coefficient D is changed with the local biomass, for a location of (x, y, z), the effective diffusion coefficient of nutrient S_j could be expressed as [135]:

$$D(x,y,z)=[1-\frac{0.43X^{0.92}(x,y,z)}{11.19+0.27X^{0.99}(x,y,z)}]D_s \tag{3.8}$$

where $X(x, y, z)$ is the biomass concentration and D_s is the diffusion coefficient of nutrient S_j in water.

The nutrient uptake rate of each soluble component in the grid element occupied by the biomass could be determined by the growth rates in table 1, biomass growth yield Y_i and average biomass density X_i. The physical description of the yield coefficient is the ratio of the increase in biomass and the consumption of related nutrients (kg biomass/ kg substrate). The biomass density in a grid element (i, j, k) is calculated as below:

$$X_i(i,j,k) = \frac{1}{\Delta x \Delta y \Delta z} \sum_{P=1}^{N_i} m_{i,p} \tag{3.9}$$

N_i is the number of the cells in biomass group i within the grid element. Therefore, the nutrient uptake rates could be obtained by resolve the following equations:

$$R_s = \left[-\frac{1}{Y_{HET}}\right] R_1 X_{HET} + \left[-\frac{1}{Y_{HET}}\right] R_4 X_{HET} + \left[-\frac{1}{Y_{HET}}\right] R_5 X_{HET} + R_6 X_{HET} + R_7 X_{AOB} + R_8 X_{NOB} + R_9 X_{HPS} + R_{10} X_I$$

$$R_{O_2} = \left[-\frac{1 - Y_{HET} - Y_{EPS}}{Y_{HET}}\right] R_1 X_{HET} + \left[-\frac{3.42 - Y_{AOB}}{Y_{AOB}}\right] R_2 X_{AOB} + \left[-\frac{1.15 - Y_{NOB}}{Y_{NOB}}\right] R_3 X_{NOB}$$

$$R_{NH_4} = \left[-\frac{1}{Y_{AOB}}\right] R_2 X_{AOB}$$

$$R_{NO_2} = \left[\frac{1}{Y_{AOB}}\right] R_2 X_{AOB} + \left[-\frac{1}{Y_{NOB}}\right] R_3 X_{NOB} + \left[-\frac{1 - Y_{HET} - Y_{EPS}}{1.17 Y_{HET}}\right] R_5 X_{HET}$$

$$R_{NO_3} = \left[\frac{1}{Y_{NOB}}\right] R_3 X_{NOB} + \left[-\frac{1 - Y_{HET} - Y_{EPS}}{2.86 Y_{HET}}\right] R_4 X_{HET}$$

3.2.3 Division of bacterial cells

Bacteria cannot grow continually, as mentioned in literature [44], they will divide in the exponential phase. In the modelling, this behaviour is implemented by sensing the mass of the cells: if the mass of the single bacterium increases exceeds the user-specified value which is normally set as twice the mass of the initial input, the mother cell will divide into two daughter cells, as shown in figure 3.2. An unequal splitting ratio is used for redistribution of biomass to

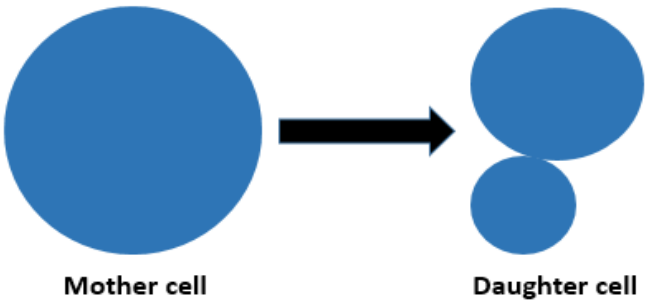

Figure 3.2. Division of the bacterial cells.

break the synchrony growth: 40 %-60 % of the biomass of mother cell could be randomly redistributed to one of the daughter agents while the other one inherits the remaining mass hence

to keep the mass balance. Considering isotropic biomass spreading, one of the daughter agents occupies the location of mother agent and the other one is placed next to it in a random direction.

3.2.4 EPS production

The previous modelling work basing on the common view that EPS can be excreted by HETs rather than AOB and NOB microorganisms. After being released outside of the microbes, EPS will help biofilm to form a complete structure. It has been demonstrated that the heterotrophic bacteria have a faster biofilm formation rate than other bacteria because of the higher growth rate and the ability to produce EPS [136].

As shown in figure 3.3, EPS production is treated in following way: at first stage, EPS is accumulated as an extra shell around HET particles; secondly, when the ratio of the outer radius (EPS) to internal radius (heterotrophic bacteria) exceeds a certain threshold value (usually equal to 1.25), then the EPS will be separated from the HET cells to form a pure EPS particle. The new EPS cell is placed around HET agent randomly which is similar to cell division.

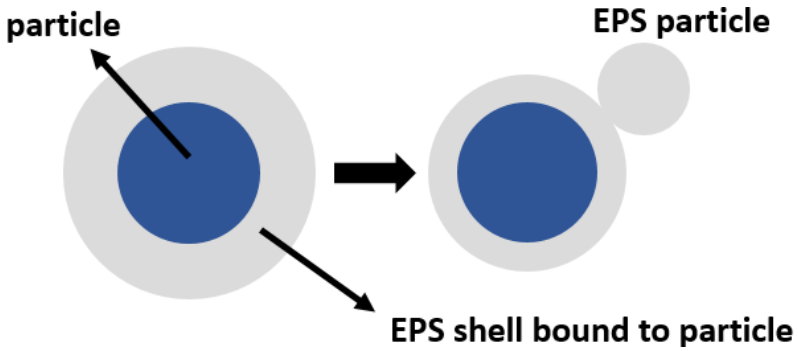

Figure 3.3. Schematic of production of EPS in NUFEB model.

3.2.5 Mechanical sub-models

The mechanical interactions between particles are calculated by using the discrete element method, which was proposed by Peter A. Cundall in 1971 to measure the acceleration in rock slopes [137]. Later, such a method has been further developed to study other materials consisting of discrete particles [138]. This has also been adopted for NUFEB model. In our modelling, the Newtonian equations of motion for particles are solved in a Lagrangian framework. The equation of translational movement of particle i is expressed as:

$$m_i \frac{d\vec{v_i}}{dt} = \vec{F_i} = \vec{F}_{a,i} + \vec{F}_{c,i} + \vec{F}_{d,i} \tag{3.10}$$

Where $\vec{F}_{a,i}$ is adhesion force, $\vec{F}_{c,i}$ is contact force, $\vec{F}_{d,i}$ is drag force.

3.2.6 EPS adhesive force

The released EPS mass from the HET particles is utilized to calculate the adhesion force between the particles, adhesion force generates with the existence of EPS mass. As illustrated in figure 3.4, the EPS link behaves as a spring to implement adhesion forces among the particles, it should be noted that if the particles do not have the EPS mass, there is no adhesive force between the two particles (e.g., the green particles in figure 3.4). The stiffness of the spring (k^{eps}) is defined per unit mass, and the effective EPS mass (m_{ij}^{eps}) could be calculated between the agents. Therefore, the effective spring stiffness is $k^{eps}m_{ij}^{eps}$. The distance between the two particles i, j is determined by solving the equation below:

$$\vec{\delta} = (d_{ij} - d_c)\,\frac{\overrightarrow{d_{ij}}}{d_{ij}} \tag{3.11}$$

where d_{ij} is the distance between the centres of two interacting particles, d_c is the sum of the two radii. Hence, the adhesion force can be expressed as:

$$\vec{F}_{eps,ij} = k^{eps}m_{ij}^{eps}\,\vec{\delta} \tag{3.12}$$

$$\vec{F}_{a,i} = \sum_{j=1}^{N}\vec{F}_{eps,ij} \tag{3.13}$$

The adhesive model applies when the distance between the particles is less than two times of the radii sum ($d_{ij} < 2d_c$). Adhesive force will become zero when the distance exceeds $2d_c$ as the bond between particles is assumed to be broken.

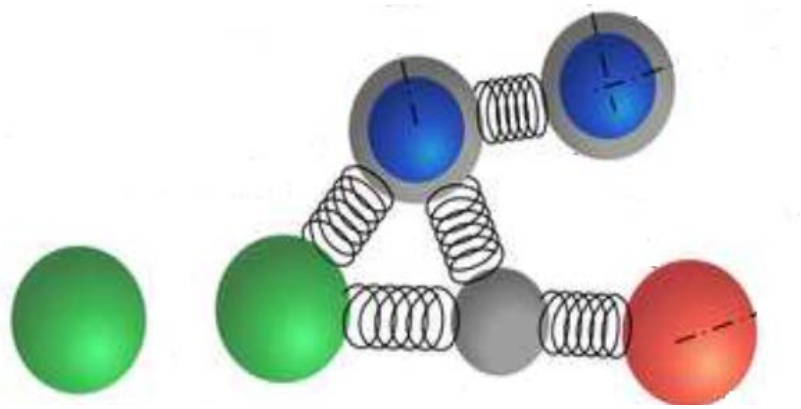

Figure 3.4. Adhesion force among agents [102].

3.2.7 Contact model

For the two particles i, j with mass m_i , m_j and radii r_i , r_j, when the distance between them d_{ij} is greater than their contact distance $d_c = r_i + r_j$, there is no contact force among the particles. Contact force between the particles occurs when $d_{ij} < d_c$. As illustrated in figure 3.5, the normal force consists of a contact force and a damping force, while the tangential force comprises a shear force and a damping force. Normal and tangential force acting on the particle i could be expressed as [139]:

$$\vec{F}_{nij} = f\left(\frac{\delta}{d_c}\right)(k_n \delta \vec{n}_{ij} - m_{eff}\gamma_n \vec{v}_n) \tag{3.14}$$

$$\vec{F}_{tij} = f\left(\frac{\delta}{d_c}\right)(-k_t \overrightarrow{S_t} - m_{eff}\gamma_t \vec{v}_t) \tag{3.15}$$

$$\vec{F}_{c,i} = \sum_j^n (\vec{F}_{nij} + \vec{F}_{tij}) \tag{3.16}$$

where δ is the normal overlap between the two particles, r_i and r_j are the diameter of two particles in the vicinity, k_n and k_t are the elastic constants for normal contact and tangential contact, γ_n and γ_t are respectively the normal damping coefficient and tangential damping coefficient, $m_{eff} = m_i m_j/(m_i + m_j)$ is the effective mass among the two particles, $\overrightarrow{S_t}$ is the vector of tangential displacement between the two agents, n_{ij} is the normal vector between the two particles, $\vec{v}_n$ and $\vec{v}_t$ are the normal component and tangential component of the relative velocity vector between the two particles. In LAMMPS, the linear spring-dash model is adopted when $f\left(\frac{\delta}{d_c}\right)$ = 1, in which the normal force is a linear function of the overlap distance. The Hertzian contact model, $f\left(\frac{\delta}{d_c}\right) = \sqrt{\delta}\sqrt{\frac{r_i r_j}{r_i + r_j}}$ is used where the normal force is a function of the overlap area. Therefore, the contact force between the two collided DEM particles *i*, *j* could be rewritten in Hookean style and Hertzian style (LAMMPS Manual):

$$\vec{F}_{ij} = \left(k_n \delta \vec{n}_{ij} - m_{eff}\gamma_n \vec{v}_n\right) - \left(k_t \overrightarrow{S_t} + m_{eff}\gamma_t \vec{v}_t\right) \tag{3.17}$$

$$\vec{F}_{ij} = \sqrt{\delta}\sqrt{\frac{r_i r_j}{r_i + r_j}}\left[\left(k_n \delta \vec{n}_{ij} - m_{eff}\gamma_n \vec{v}_n\right) - \left(k_t \overrightarrow{S_t} + m_{eff}\gamma_t \vec{v}_t\right)\right] \tag{3.18}$$

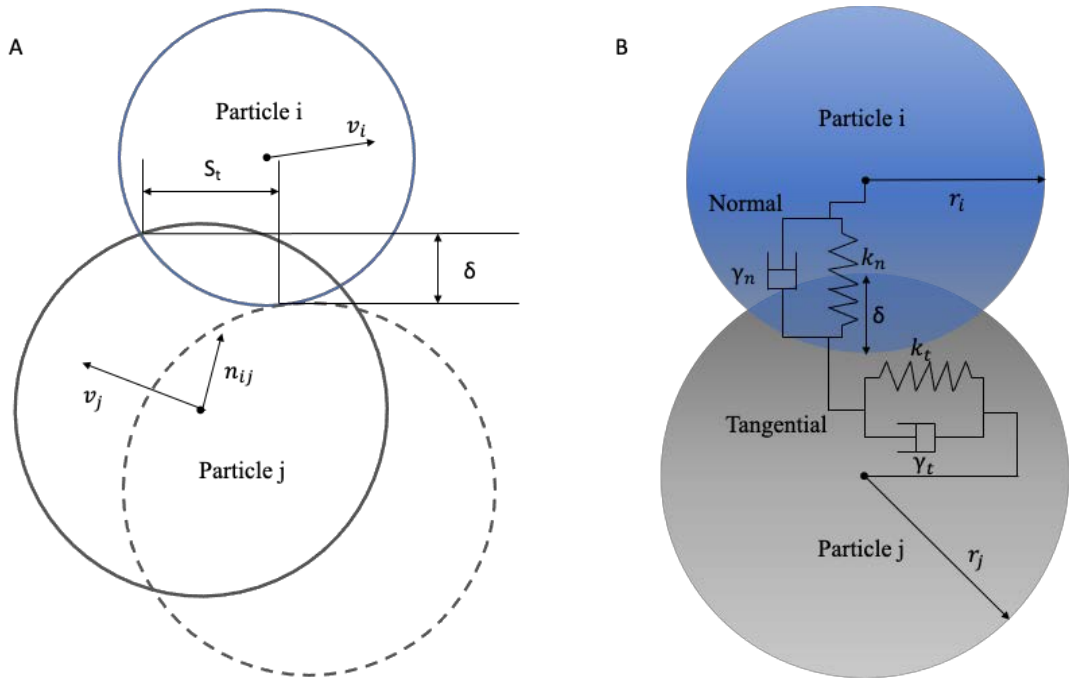

Figure 3.5. (A) Normal displacement δ and tangential displacement S_t [140]. (B) Collision model between two particles.

3.2.8 Drag model

The Stocks' law could be applied to study the motion of spherical particles in the laminar flow [141]. In this individual-based modelling, drag force is calculated as the force due to Stokes flow around a sphere:

$$\vec{F}_{d,i} = 3\pi d_i \eta \overrightarrow{v_r} \tag{3.19}$$

where d_i is the diameter of the particles, η is the dynamic viscosity of the fluid, $\overrightarrow{v_r}$ is the velocity vector between the particles and the fluid.

3.3 Two-way coupling fluid-structure interaction biofilm model

The two-way coupling model is established by extending the CFD-DEM solver SediFoam with microbial cells. SediFoam is coupling OpenFOAM (Open-source Field Operation and Manipulation) and LAMMPS [142]. CFD-DEM approach has been widely used for particle-laden flows such as sediment transport and gas-solid fluidization [143, 144]. In this two-way coupled model, CFD is utilized to solve the fluid field while the particle motion is tracked by DEM on a Lagrangian framework. Figure 3.6 displays the flowchart of CFD-DEM approach. The equations of fluid and particle motion are calculated independently at each simulation time

step. In CFD module, an averaging algorithm based on diffusion is developed to achieve the mapping from particle-scale quantities to macroscopic quantities [145]. The averaging procedure is carried out based on the updated particle state from DEM, then the fluid equations are solved based on finite volume method [142]. The equations of fluid motion, particle motion and fluid-particle interaction force are introduced in detail below.

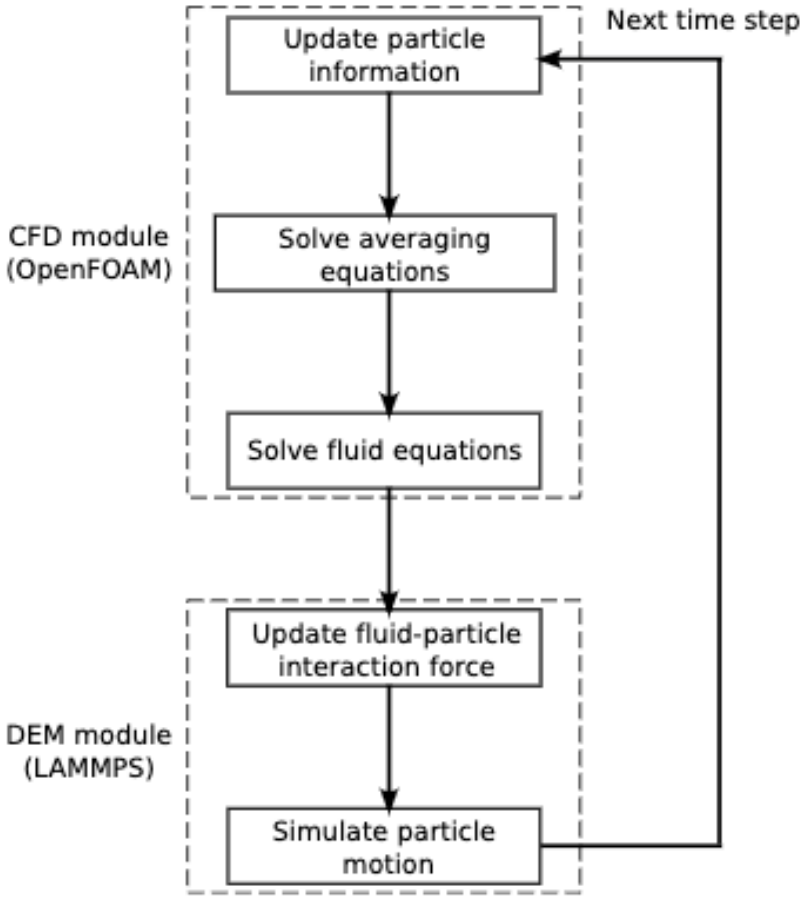

Figure 3.6. The flowchart of the CFD-DEM approach.

3.3.1 Discrete element method for particle motion

In the CFD-DEM approach, motion of particle i is calculated based on Newton's second law as the following equations:

$$m_i \frac{d\vec{v}_i}{dt} = \vec{F} = \vec{F}_{c,i} + \vec{F}_{coh,i} + \vec{F}_{fp,i} \tag{3.20}$$

where $\vec{v}_i$ is the velocity of the particle; m_i is the particle mass; $\vec{F}_{c,i}$ is the contact force among collided particles, $\vec{F}_{coh,i}$ is inter-particle cohesive force, $\vec{F}_{fp,i}$ is the fluid-particles interaction force. The details of contact model are introduced in section 3.2.7. The fluid-particle interaction

force $\vec{F}_{fp,i}$ is calculated by OpenFOAM and then substitute to DEM model to update the particle information.

3.3.2 Cohesive model

The cohesive force among the biofilm particles is represented by the following formula [146, 147] :

$$\vec{F}_{coh,i} = -\frac{A}{6}\frac{64r_i^3 r_j^3(s+r_i+r_j)}{(s^2+2r_i s+2r_j s)^2(s^2+2r_i s+2r_j s+4r_i r_j)^2}\vec{n}_{ij} \tag{3.21}$$

where A is the cohesive strength, s is the separation distance between the particle surface. A minimum separation distance s_{min} is implemented when the separation distance between the two particles equals to zero ($s = 0$).

3.3.3 Locally-Averaged Navier-Strokes equations for fluids

The fluid flow is described by locally-averaged incompressible Navier-Stokes equations. Assuming constant fluid density ρ_f, the governing equations for the fluid are [142]:

$$\nabla \cdot \left(\epsilon_s \vec{U}_s + \epsilon_f \vec{U}_f\right) = 0, \tag{3.22a}$$

$$\frac{\partial(\epsilon_f \vec{U}_f)}{\partial t} + \nabla \cdot \left(\epsilon_f \vec{U}_f \vec{U}_f\right) = \frac{1}{\rho_f}(-\nabla p + \epsilon_f \nabla \cdot \vec{R} + \epsilon_f \rho_f \vec{g} + \vec{F}_{fp}) \tag{3.22b}$$

ϵ_s is solid volume fraction while ϵ_f is fluid volume fraction which equals to (1-ϵ_s). $\vec{U}_s$ and $\vec{U}_f$ are particle velocity and fluid velocity, respectively. $\vec{F}_{fp}$ is the fluid-particle interaction force. ∇p is the pressure gradient, $\vec{g}$ is gravity and $\vec{R}$ is the stress tensor consisting of viscous stress and Reynolds stress.

Equation (3.21) and (3.22) are discretized by the collocated volume grids. The solid volume fraction and fluid volume fraction ϵ_s, ϵ_f are spatial dependent in the simulation. The microbial particles are immersed in the fluid. For each grid element (g) in the simulation, the solid volume fraction is the ratio of the total particle volume within the grid element over the volume of the grid element V_g [145]:

$$\epsilon_{s,c} = \frac{\sum_{i=1}^{n_{p,g}} V_{p,i}}{V_g} \tag{3.23}$$

Where $n_{p,g}$ is the number of particles in the grid element, $V_{p,i}$ is the volume of particle i, V_g is the total volume of the grid. In addition, the continuum Eulerian field of ϵ_s, $\vec{U}_s$ and $\vec{F}_{fp}$ should be computed by using the coarse graining algorithm to solve the equation. The details of this averaging procedure are described in [145, 148]. Therefore, only the averaged flow feature

could be captured by the locally-averaged Navier-Stokes equations. That is, the detailed flow features at small scales, such as boundary layer at the particle surface, could not be resolved by the CFD-DEM approach[147].

3.3.4 Fluid-particle interaction

The fluid-particle interaction force $\vec{F}_{fp,i}$ consists the drag force and lift force. For the particle i, the drag force model is expressed as [147]:

$$\vec{F}_{fp,i}^{drag} = \frac{V_{p,i}}{\epsilon_{f,i}\epsilon_{s,i}} \beta_i \left(\vec{U}_{f,i} - \vec{u}_{p,i}\right) \tag{3.24}$$

where $V_{p,i}$ is the volume of the particle i, $\vec{U}_{f,i}$ and $\vec{u}_{p,i}$ are the fluid velocity and particle velocity, respectively. $\epsilon_{f,i}$ is fluid volume fraction while $\epsilon_{s,i}$ is solid volume fraction, β_i is the drag correlation coefficient which is used to convert terminal velocity correlation to drag correlation [149]:

$$\beta_i = \frac{3}{4}\frac{C_{d,i}}{V_{r,i}^2}\frac{\rho_f|\vec{U}_{f,i}-\vec{u}_{p,i}|}{d_{p,i}} \epsilon_{f,i}\epsilon_{s,i} \tag{3.25}$$

where $C_{d,i} = \left[0.63 + 4.8\sqrt{\frac{V_r}{R_{e_{p,i}}}}\right]^2$ is the drag coefficient, $d_{p,i}$ is the diameter of particle i, $R_{e_{p,i}}$ is the particle Reynolds number expressed as:

$$R_{e_{p,i}} = \rho_s d_{p,i}\left|\vec{U}_{f,i} - \vec{u}_{p,i}\right|/\mu \tag{3.26}$$

Where ρ_s is the density of particle, μ is the dynamic viscosity of fluid flow, $V_{r,i}$ is the terminal velocity correction for particle i [150]:

$$V_{r,i} = 0.5\left[A - 0.06R_{e_{p,i}} + \sqrt{(0.06R_{e_{p,i}})^2 + 0.12R_{e_{p,i}}(2B - A) + A^2}\right] \tag{3.27}$$

The function of void fraction A and B are defined as:

$$A = \epsilon_{f,i}^{4.14} \tag{3.28a}$$

$$B = \begin{cases} 0.8\epsilon_{f,i}^{1.28} & \text{if } \epsilon_{f,i} \le 0.85 \\ \epsilon_{f,i}^{2.65} & \text{if } \epsilon_{f,i} \le 0.85 \end{cases} \tag{3.28b}$$

In addition, the lift force on the particle i is calculated by the following formular [147, 151, 152]:

$$\vec{F}_{fp,i}^{lift} = C_l(\rho_f \mu)^{0.5} d_{p,i}^2 \left(\vec{U}_{f,i} - \vec{u}_{p,i}\right) \times \frac{\omega_i}{|\omega_i|^{0.5}} \tag{3.29}$$

where C_l is the lift coefficient equals to 1.6, $\omega_i = \nabla \times \vec{U}_{f,i}$ is the curl of flow velocity interpolated to the center of particle i.

4 Biofilm formation and detachment due to the simple shear flow

4.1 Introduction

Bacterial biofilms are microbial communities attached to the wet surface and encased within a self-produced matrix which terms extracellular polymeric substance [153]. Biofilm is the typical mode of bacterial survival in nature since the formation of biofilm helps the bacteria to live in adverse environments [154]. In addition, it was found that the bacteria, which embedded in the biofilm, have an extremely high resistant to antibiotics than when they are in planktonic state [8]. Biofilm formation is the result of a series of biological, chemical and physical events, mainly including bacterial cell transport to the surface, initial reversible and irreversible attachment, biofilm growth and EPS extraction, biofilm maturation, dispersion and detachment of biofilm [25]. The emergence of biofilms poses various threats to human health since they are responsible for nearly 65 % of all hospital infections [155]. For example, biofilm on in-dwelling medical devices would cause biofilm-related infection [156]. Apart from these, the formation of biofilm on the metallic materials surface may accelerate the corrosion rate of metals [157, 158]. This kind of biocorrosion was widely found in marine environments and cooling tower system [159, 160]. Therefore, it is desirable to investigate and predict the development of biofilm and their mechanical characteristics. In this case, mechanistic biofilm models could be used as a powerful research tool and an assistant of engineering practice.

Biofilm modelling could include all these major processes during biofilm development. Besides, specified biofilm behaviour could be described by using the mathematical models. A lot of modelling work focused on biofilm detachment since it is an essential process in biofilm life cycle. In the one-dimensional biofilm model, different empirical numerical models were applied to describe the biofilm detachment rate. For example, a commonly used detachment model assumed the detachment rate to be proportional to the biofilm mass and thickness [70]. In addition, a detachment velocity, which was defined as a second-order function of biofilm thickness, was adopted to describe the detachment of biofilm [71]. This detachment model was further extended to multidimension, the velocity was defined in the normal direction to the surface of the biofilm/liquid interface [98]. Besides, the probability of detachment, which depends on the square of biofilm height above the substratum, was applied to simulate the shear

detachment [161]. However, the mechanisms of biofilm detachment, such as erosion and sloughing, were not well understood.

In this study, the individual based model of microbials was implemented into LAMMPS which is an open-source molecular dynamics simulator. IbM is a bottom-up approach which could be used to model a macroscopic system by describing the actions and properties of the individuals comprising the system [20]. Therefore, the agents in the individual based model are defined as independent entities with their own state and behaviour [96]. The present model could combine the biological processes (e.g. bacteria growth and division, EPS extraction) with mechanical interactions (e.g. contact force, EPS adhesion force and drag force) among individual agent within the biofilm system.

The deformation and detachment of biofilm were investigated by using the IbM, the processes of biofilm growth and biofilm deformation were decoupled in this work. Therefore, the deformation and detachment of biofilm is a result of mechanical interactions between EPS and bacterial cells when biofilm exposed to the shear flow. Since the motion of bacteria in the hydrodynamic environments is primarily dominated by the viscous force [162], we assume overdamped dynamics of biofilm formation and detachment in this study. This is different with the simulations in [102] where the motion of particles is governed by Newton's Law. The shear flow was controlled by the inlet shear rate, thus the detachment of biofilm has been studied by increasing shear rate. The extracellular polymeric substances are of critical importance as they function as a house to keep bacterial cells in close proximity [2]. They also help biofilm adhering to another surface, which contributes to the mechanical stability of biofilm. EPS are distributed between cells in a nonhomogeneous pattern in the biofilm [163]. Therefore, the EPS production and distribution within the biofilm may further affect the detachment of biofilm. The analysis of EPS volume is nontrivial which requires using expensive dyes. In this chapter, we also aim to study how the EPS amounts affect the biofilm detachment by using IbM.

4.2 Methodology

4.2.1 Biofilm growth

In the present work, the single-species (heterotrophs) biofilms are considered. The assumptions of the model are as follows. The growth of heterotrophic bacteria will not be limited by the oxygen thus only the carbonic substrate (S_s) was consumed. In addition, the decay and death of bacteria are negligible in this study, therefore, the advection-diffusion-reaction equation (3.5) could be simplified as:

$$\frac{\partial S}{\partial t} + \vec{U} \cdot \nabla S_S = D\nabla^2 S_S - \frac{\mu_{m,HET}}{Y_{HET}} \frac{S_S}{K_S + S_S} X_{HET} \quad (4.1)$$

The manner of bacteria division and EPS production was introduced in section 3.2.3, the main kinetic parameters for biofilm growth are given in Table 4.1.

Table 4.1 Kinetic parameters for biofilm growth.

Parameter	Symbol	Value	Unit	Reference
Simulation domains dimension	L_x, L_y, L_z	300, 40, 100	μm	Chosen
Grid dimensions	N_x, N_y, N_z	90, 12, 30	-	Chosen
Diffusion coefficient for substrate	D_s	1.6E-9	$m^2\ s^{-1}$	[102]
Nutrient concentrations	S_S	1.0E-4	$kg\ m^{-3}$	Chosen
Kinetics and yields				
Maximum specific growth rate	$\mu_{m,HET}$	2.8E-4	s^{-1}	[102]
Substrate affinity	K_S	3.5E-5	$kg\ m^{-3}$	[102]
Yield coefficient	Y_{HET}	6.1E-1	gcod/gcod	[164]

4.2.2 Simulation domain

Initially, there were four heterotrophic bacterial cells with diameter of 1 μm at the bottom left corner of the microchannel. The biofilm was cultured for 4.63 days as shown figure 4.1. Then the biofilm deformation and detachment have been modelled by applying a simple shear flow along the x direction. The growth of biofilm is assumed to be frozen during the detachment process. Therefore, the processes of biofilm growth and biofilm detachment were decoupled in this study, the simulation timesteps for biofilm growth and detachment were set as 10 s and 2.5 s, respectively. In this model, the shear rate ζ is one of the input parameters which could be specified in the model. Therefore, the flow velocity in the simulation box could be calculated as:

$$u_{flow} = \zeta h \quad (4.2)$$

where h is the height in the z direction. Thereby, the flow velocity increases linearly from 0 at the bottom wall to ζL_z (m/s) at the top wall. The Reynolds R_e number could be calculated as follows [23, 165]:

$$R_e = \frac{u_{avg} D_h}{\nu} \quad (4.3)$$

where D_h was the hydraulic diameter, u_{avg} is the average flow velocity in the channel, ν is the kinematic viscosity of water at 20 ℃. The hydraulic diameter could be calculated based on the cross-sectional area:

$$D_h = \frac{4L_yL_z}{2(L_y+L_z)} \tag{4.4}$$

The average flow velocity could be approximated from the maximum flow velocity as $u_{avg} = \frac{1}{2}\zeta L_z$. Thereby, the corresponding Reynolds number ranges from 2.8E-4 to 1.425E-3.

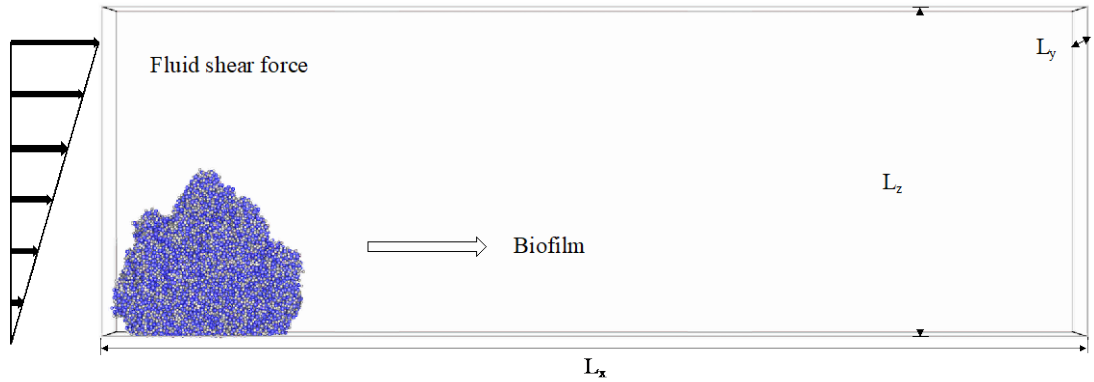

Figure 4.1. Schematic of the simulation domain.

Since the EPS adhesion force and fluid shear force are the primary factors which could affect the biofilm detachment, our simulation was divided into three sections:

1. Biofilms with different EPS amount were grown without shear flow by increasing the EPS formation coefficient (Y_{eps}) from 0.04 to 0.24, then the applied shear rate was kept at 0.2 s^{-1} during deformation and detachment.

2. Biofilm were grown without the shear flow by fixing the EPS formation coefficient at 0.18, the shear rate was elevated from 0.1 to 0.5 s^{-1}.

3. The biofilms were grown under a small shear rate flow, afterwards, the detachment of the biofilms was monitored by increasing the shear rate.

For the global simulation box, the fixed boundary conditions are applied in both x and z walls, while the periodic boundary condition was used in y walls (LAMMPS Manual). Therefore, the detached biofilm flocs move outside the box will be deleted from the simulation box. For the nutrition diffusion, the no-flux Neumann boundary condition was used at the bottom wall, while the Dirichlet boundary condition was adopted at the top wall where the concentration of nutrients is constants.

4.2.3 Overdamped dynamics and mechanical interaction

In LAMMPS, the particle motion is governed by Newton's second law based on the Verlet algorithm [166]: the position is firstly updated to obtain the force field, then the acceleration of the particle has been calculated, finally the velocity could be updated to compute the particle position at the next timestep [166]. The Reynold number is very small in this case which indicates the viscous force is dominated in the system and bacteria cells are in an extremely viscous environment [167]. Therefore, in this chapter, the motion of the particles is assumed to be overdamped. In an overdamped system, the inertia of the particle could be neglected, the total force on the particle is given by:

$$\varphi \frac{d\vec{x_i}}{dt} = \vec{F_i} = (\vec{F}_{a,i} + \vec{F}_{c,i} + \vec{F}_{d,i}) \tag{4.5}$$

where φ is the friction coefficient, the velocity of particles is directly updated by the force field. The contact force $\vec{F}_{c,i}$ (equation 3.18), EPS adhesion force $\vec{F}_{a,i}$ (equation 3.13) and fluid shear force $\vec{F}_{d,i}$ (equation 3.19) were adopted here to describe the mechanical interaction among the particles. The details of relevant sub-models have been explained in chapter 3. The contact force between the particle and the wall is calculated in the same manner as particle-particle interaction (equation 3.18) by assuming the mass of the wall infinite. In addition, the EPS-wall adhesion model was included in this study. EPS-wall adhesion occurs when the EPS particles have overlap with the wall. Similar to the EPS adhesion model, the EPS-wall (bottom wall, z = 0) adhesive force could be expressed as:

$$\vec{F}_{eps,wall} = -k_{anc}\, m_{eps}\, d_{overlap} \tag{4.6}$$

where k_{anc} is the adhesive stiffness (per unit EPS mass), m_{eps} is the mass of EPS which overlapped with the bottom wall, $d_{overlap}$ is the overlap depth which equals to the radius of EPS particle minus its heigh.

In the Hertzian contact model (equation 3.18), k_n is the spring constant in normal direction which could be calculated as (LAMMPS Manual):

$$k_n = \frac{4G}{3(1-v)} \tag{4.7}$$

where v is the Poisson's ratio which is assumed to be 0.5, and G is the shear modulus given by:

$$G = \frac{E}{2(1+v)} \tag{4.8}$$

where E is the Young's modulus. The empirical mechanical parameters are listed in table 4.2.

Table 4.2 Empirical mechanical parameters used in the model.

Mechanical parameters		
Spring stiffness for collision	k_n	100 Pa [122]
Damping coefficient for collision	γ_n	10 m s^{-1} (Chosen)
EPS stiffness (per unit EPS mass)	k^{eps}	5E+9 s^{-2} [102]
Adhesive stiffness for EPS-wall interaction (per unit EPS mass)	k_{anc}	5E+3 s^{-2} (Chosen)
Friction coefficient	φ	1E-3 (Chosen)
Fluid dynamic viscosity	η	1E-3 Pa s (For water)

4.3 Results and Discussion

4.3.1 The detachment of biofilms with different EPS amount

Biofilms consist of different number of heterotrophic bacteria cells and EPS cells were obtained by varying the EPS formation coefficient during biofilm growth. The biofilm volume, the number of HET and EPS particles, the total detached biofilm volume and the total time for all detachment events at various EPS growth yield were summarised in Table 4.3. The shear rate was set as a constant here, equal to 0.2 s^{-1}. The results show that there is no EPS particle in the biofilm system when Y_{eps} is less than 0.1. As introduced in chapter 3, in this model, EPS was produced by heterotrophic bacteria and initially accumulated as a shell around the bacterial cells. When EPS formation coefficient is small (less than 0.1), the thickness of the accumulated EPS bound did not exceed the threshold value, thus no EPS particle was extracted in the biofilm system. However, there still is the adhesion force among the particles which is proportional to the mass of EPS.

Table 4.3 The summary of key input and output parameters for the present modelling.

EPS formation coefficient	HET particles	EPS particles	Volume of biofilm (m^3)	Total detached biofilm volume (m^3)	Total detachment time (days)
0.04	15858	0	1.45E-14	6.82E-15	19.2
0.06	15048	0	1.37E-14	3.01E-15	21.2
0.08	14839	0	1.35E-14	4.89E-15	18.9
0.1	15458	0	1.40E-14	3.50E-15	18.5
0.12	15790	5680	1.68E-14	4.77E-15	14.4
0.14	16318	13163	2.06E-14	5.16E-15	16.7
0.16	16647	19624	2.37E-14	4.53E-15	11.2
0.18	16951	26047	2.67E-14	5.47E-15	8.39
0.2	17454	32676	3.02E-14	1.39E-14	19.1
0.22	17529	39073	3.27E-14	1.43E-14	9.9
0.24	18090	46400	3.69E-14	1.60E-14	21.3

Figure 4.2 shows the preformed biofilms ($0.04 \leq Y_{eps} \leq 0.1$) and the detachment of those biofilms after 21.93 days. It can be seen that the biofilm morphology changed with the EPS production, and there are no EPS particles in the system. It was found that the height of the pre-grown biofilms slightly decreased with raised Y_{eps} when the production of EPS in the biofilm is low ($0.04 \leq Y_{eps} \leq 0.1$). It indicates that the biofilm would become more packed due to the increased EPS production, which results in the higher cohesive and adhesive force. In addition, the shear force in the present model is proportional to the height of the simulation box. Thereby, the higher biofilm would experience a larger shear force. As a result, it was found that the biofilm grown at EPS formation coefficient of 0.04 could detach easily and rapidly, and the secondary detachment was captured in this case. The extracted EPS particles were observed when Y_{eps} is 0.12. Further increased the EPS formation coefficient from 0.12 to 0.24, the number of EPS particles grew rapidly, meanwhile, the HET particles increased slightly during the same time. It was suggested that the bacteria growth might be facilitated by the EPS production. The biofilm volume was computed by summing the volume of all the particles. Correspondingly, the total volume of biofilms increases significantly with EPS formation coefficient, up to 3.69E-14 m^3 at maximum Y_{eps} of 0.24.

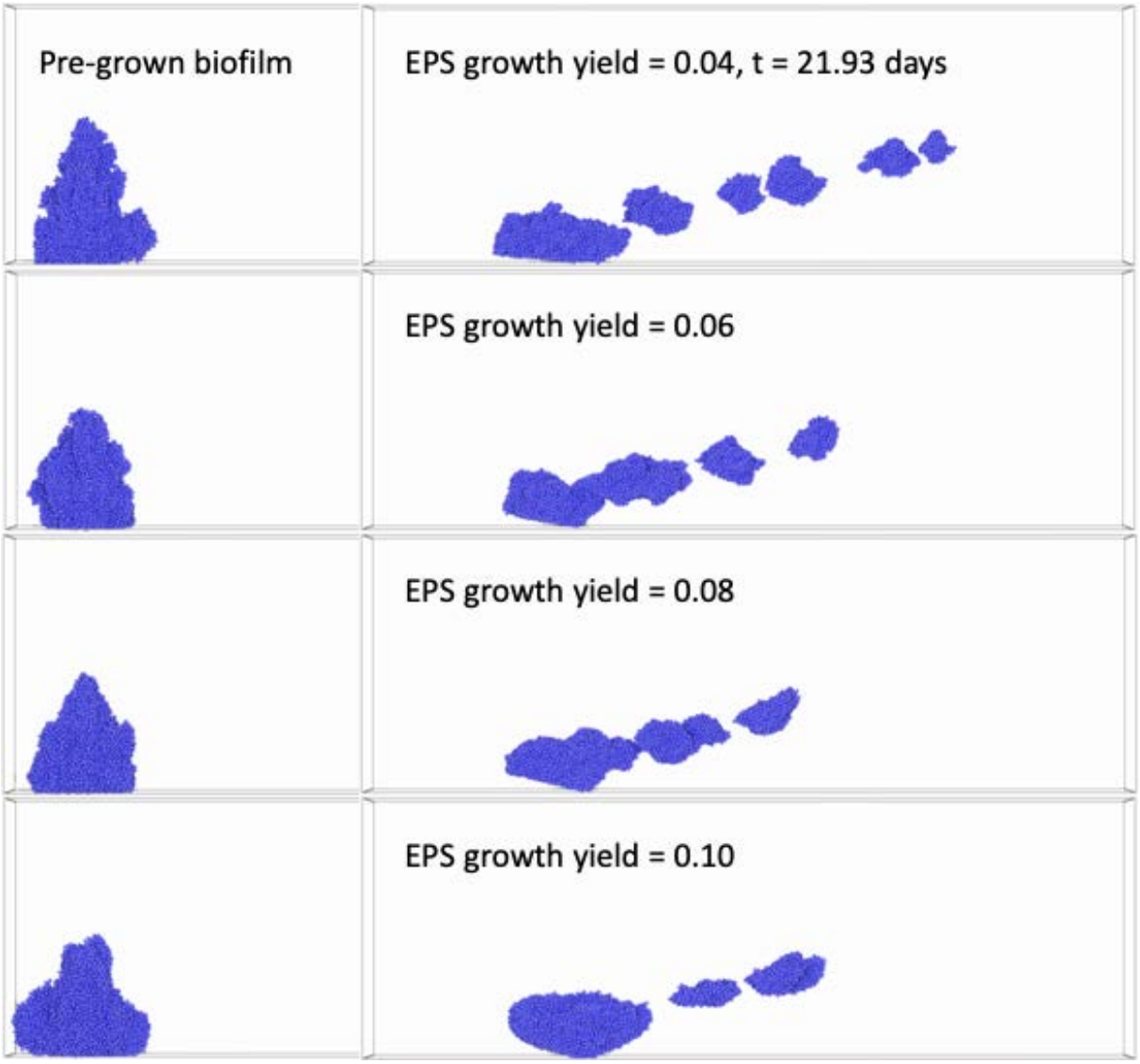

Figure 4.2. Shear force induced biofilm detachment of a pre-existing biofilm after 21.93 days, Y_{eps} ranges from 0.04 to 0.10, shear rate equal to 0.2 s^{-1}.

Figure 4.3 displays the shear force induced biofilm detachment of the pre-grown biofilms, the EPS formation coefficient for biofilms growth ranged from 0.12 to 0.24, those biofilms were subjected to the applied shear force for 21.93 days. As shown in table 4.3, the number of EPS particles was one third of the number of HET particles in the biofilm when Y_{eps} equal to 0.12. When Y_{eps} reached the maximum value (i.e. 0.24), the number of EPS particles become more than twice as much as HET particles. It was observed that the biofilm morphology changes a lot due to the sharply increased EPS amount (figure 4.3). In addition, only biofilm sloughing (detached biofilm flocs were relatively large) was monitored during the whole biofilm detachment processes when the biofilm system was dominated by the viscous force.

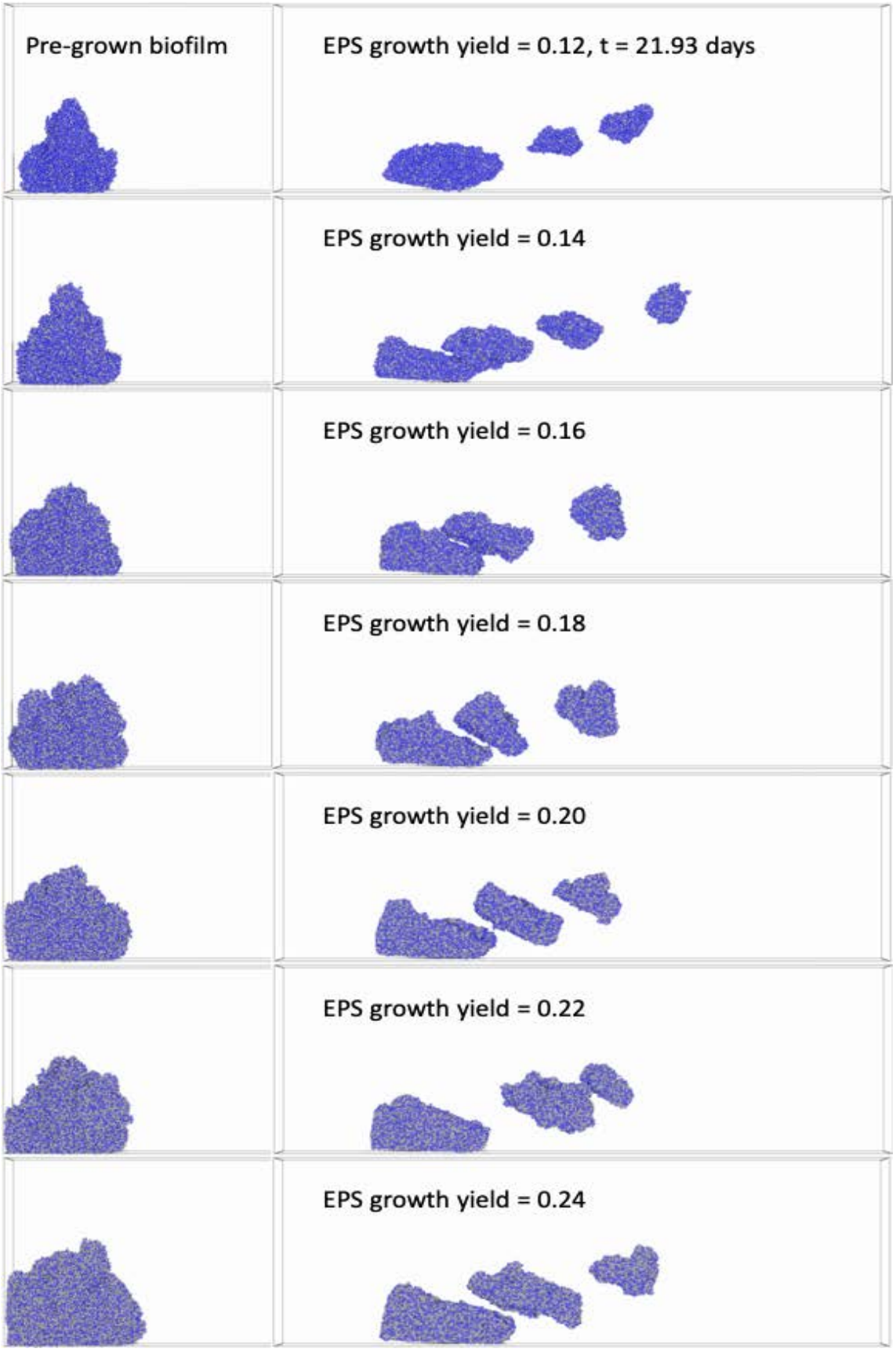

Figure 4.3. Flow induced biofilm detachment of a pre-existing biofilm after 21.93 days, Y_{eps} ranged from 0.12 to 0.24, shear rate equal to 0.2 s^{-1}.

In order to investigate how EPS amount affects biofilm deformation, the detachment rate coefficient, defined as the daily volume of detached biofilm divided by the total volume of preformed biofilm, was calculated. Figure 4.4 illustrates the curve of detachment rate coefficient versus EPS growth yield. The simulation was run for three replicates and the average results were calculated. It was found that there was no clear relationship between the ESP amount and detachment rate coefficient. When the EPS formation coefficient ranged from 0.12 to 0.16, the detachment rate coefficient increased with the Y_{eps}. The coefficient decreased when Y_{eps} reached 0.18. Afterwards, it increased again by further increasing the EPS formation coefficient and reached a peak at Y_{eps} of 0.22. Finally, the detachment rate coefficient decreased when the Y_{eps} rose to 0.24. It may indicate that when the inlet shear rate is the same, the biofilm floc could easily detach from their parent cluster at Y_{eps} of 0.22.

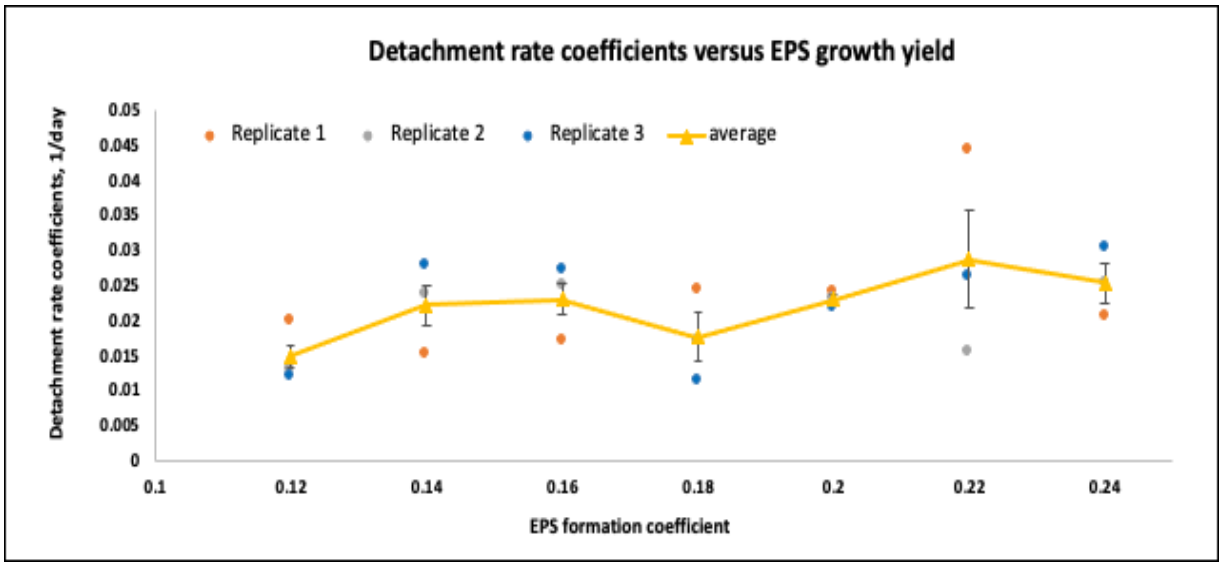

Figure 4.4. Detachment rate coefficients of biofilms with different EPS formation coefficient. The shear rate is 0.2 s^{-1}.

In principle, the increase in EPS amount would result in a higher cohesion within the biofilm, however, it seemed that the increased cohesion did not play an important role in protecting the biofilm from the applied shear flow. This might because of the simplified shear model in this work, in which the shear flow was applied along x direction and the fluid velocity was calculated based on the height of the particles. Additionally, the biofilm did not affect the flow pattern in return. In this case, the detachment of the biofilms can also be affected by its morphology and maximum height.

For a given EPS amount, three simulation replications were performed. The biofilms with different morphology and EPS distribution were obtained from different replicates due to the stochastic nature of the daughter cell size and the distribution of bacteria (division) and EPS (extraction) cells. The results showed the varied detachment rate coefficient in each replicate when the EPS formation coefficient is the same. For example, it was found the detachment rate coefficient was very high when the EPS growth yield is 0.22 in replicate 1 but a bit low for replicate 2. As shown in figure 4.3, the morphology of preformed biofilm looks tilted along the x direction, the protruding fraction easily detach with the shear flow. This further documented that the detachment of biofilms was more affected by the stochastic variation of the preformed biofilm morphology and spatial distribution of EPS within the biofilm.

4.3.2 Shear flow induced deformation and detachment of biofilm grown in static culture

In this case, the preformed biofilm was grown at a fixed EPS formation coefficient of 0.18. Five different shear rates, 0.1, 0.2, 0.3, 0.4, 0.5 s^{-1}, are applied to study how the shear rate affects the biofilm detachment. Besides, in order to reduce the effect of biofilm morphology on biofilm detachment, the initial nutrient concentration and particles position were kept as the same in each case. Figure 4.5 displayed the shear flow induced biofilm detachment of the preformed biofilm over time at a shear rate of 0.1 s^{-1}. It was observed that only deformation of biofilm occurred when exposed to a small fluid shear force. After about 21.93 days, a small floc of biofilm was going to leave their parent cluster. In addition, it can be seen that the whole biofilm slides along the fluid shear force direction while retaining on the flat surface.

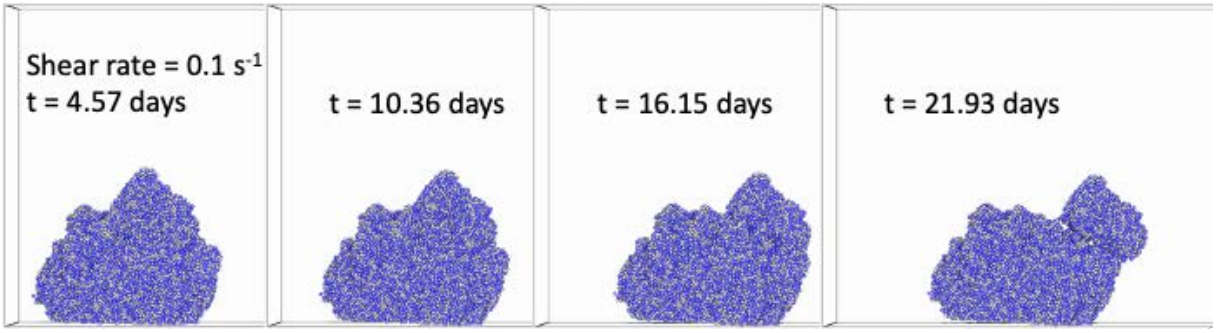

Figure 4.5. Flow induced biofilm detachment of the preformed biofilm over time, shear rate equal to 0.1 s^{-1}, the EPS formation coefficient is 0.18.

Figure 4.6 displays biofilm detachment at higher shear rate (from 0.2 to 0.5 s^{-1}), the time for biofilm in exposure to shear force was 4.57 days and 16.15 days, respectively. During the first 4.57 days, the biofilm deformed along the direction of the shear flow, the deformation increased

with raised shear rate. When the shear rate is 0.2 s^{-1}, biofilm sloughing occurs after 8.39 days. In addition, a bigger biofilm cluster was going to detach on around 20.8 days when the biofilm continuously exposed to the shear flow (figure 4.7A). A small biofilm cluster detached from parent biofilm after 6.54 days when shear rate increases to 0.3 s^{-1}, the second detachment event was captured after around another 6 days (figure 4.7B). By contrast, the volume of the second detached cluster was significantly larger than that of the first detached biofilm floc. After leaving the bulk biofilm, the detached biofilm cluster break again and divided into two small clusters due to the applied shear force (circled in figure 4.6B). Similar phenomena have been monitored at shear rate of 0.4 s^{-1} and 0.5 s^{-1}. At shear rate of 0.4 s^{-1}, the first and second detachment occurred almost simultaneously, around 7 days (figure 4.7C). As shown in figure 4.7D, the time required for biofilm detachment reduces to 5.73 days at the highest shear rate (0.5 s^{-1}). In this case, biofilm detached at a higher frequency. The detached biofilm floc kept moving with the applied shear flow, as show in figure 4.6D, some of the biofilm flocs move out from the simulation box after about 16 days.

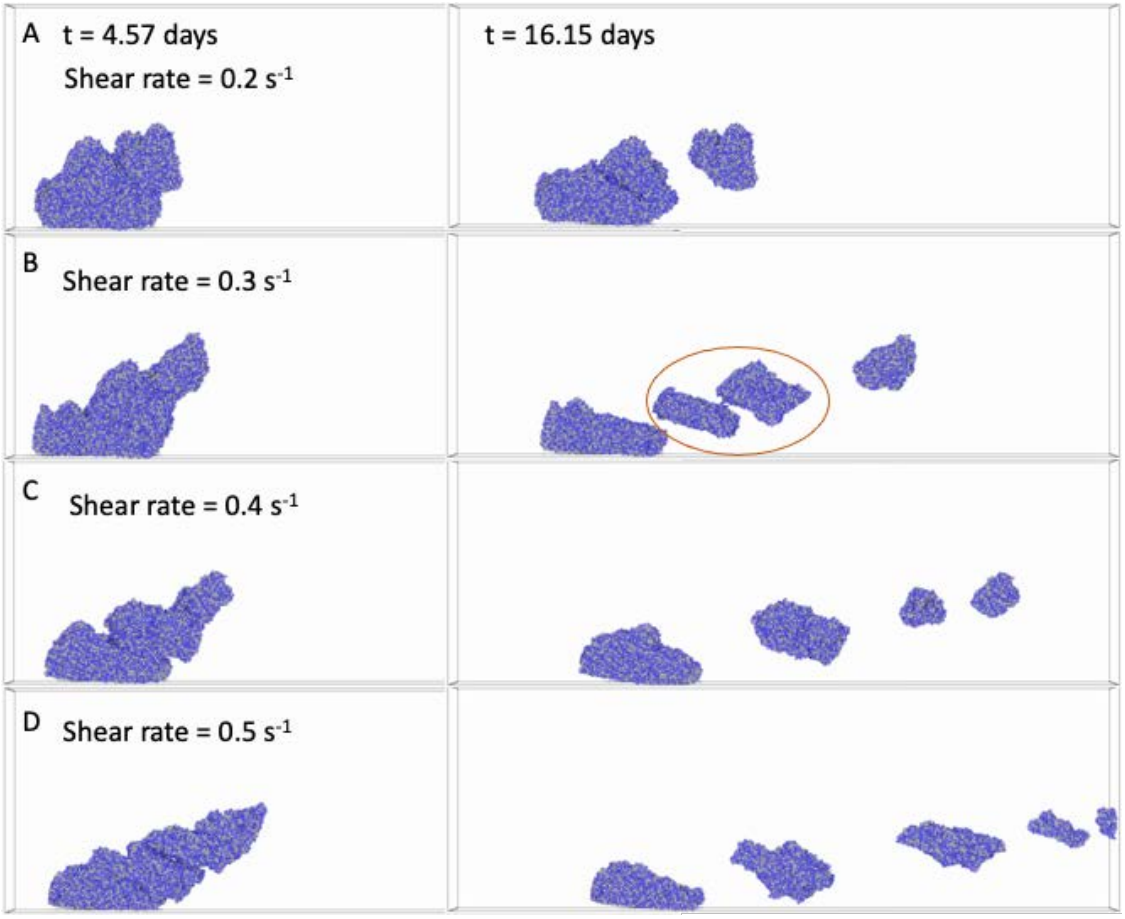

Figure 4.6. Biofilm exposed to the simple shear flow after 4.75 days and 16.15 days. The inlet shear rate varied from 0.2 to 0.5 s^{-1}, the EPS formation coefficient was fixed at 0.18 during biofilm growth.

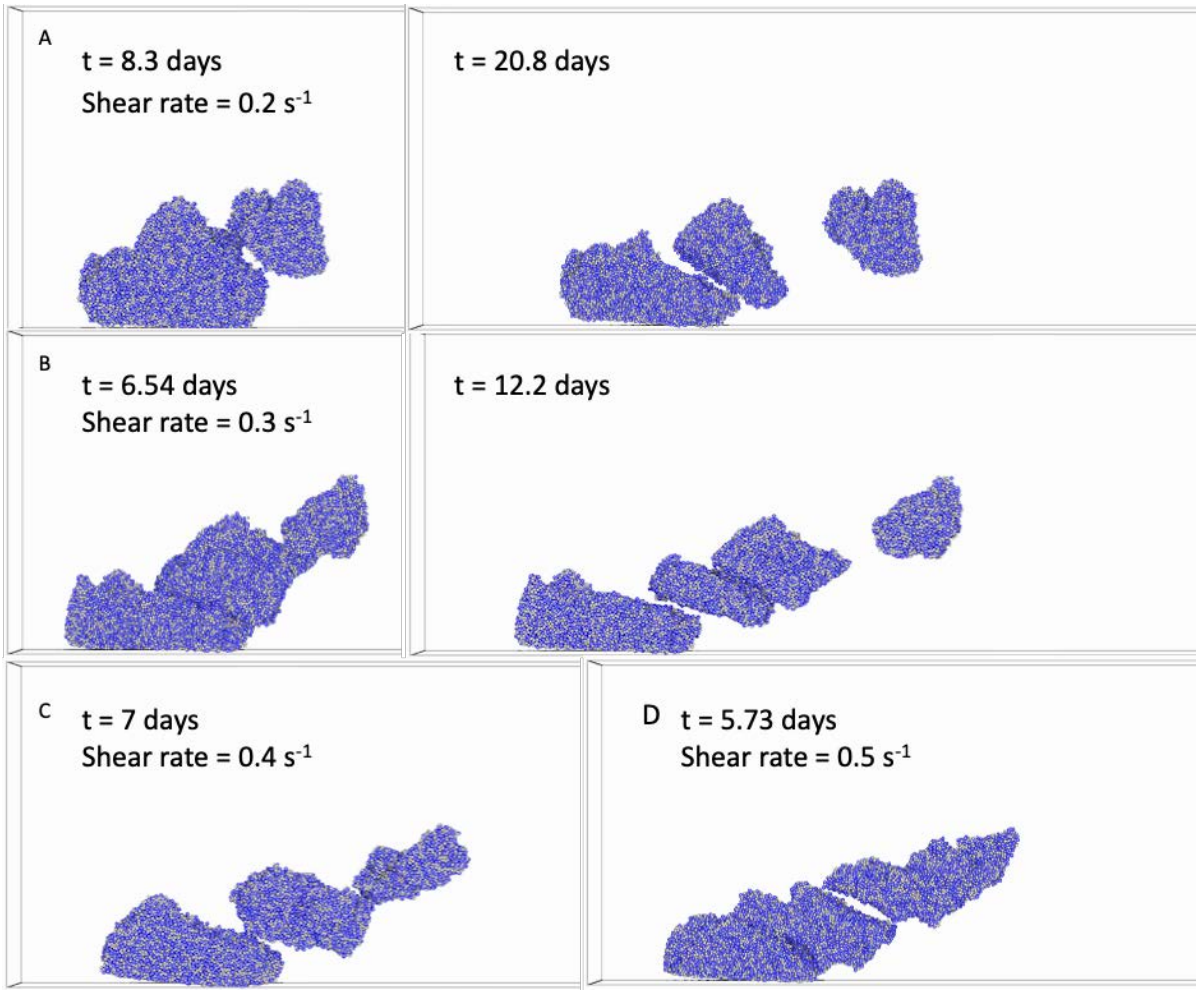

Figure 4.7. Biofilm detachment behavior at different shear flows. EPS formation coefficient for biofilm growth was fixed at 0.18.

It was found that the detachment event was significantly affected by the shear rate when the biofilm was subjected to shear flow. Three replicates of the simulation were performed. The average results with standard deviations were computed and shown in figure 4.8. It was found that the average detachment rate coefficient was proportional to the increased shear rate. This trend has also been captured in each replicate. The results indicate that the biofilm detachment was affected by their stochastic structures as well but mainly determined by the shear rate in this case. This result was similar to the experimental observation from Stoodley et al., who found that the detachment rate coefficient increased with flow velocity [54]. It was worth noting that there seems to be a linear relationship between detachment rate coefficient and the applied shear rate, it may help us to predict the detached biofilm volume in a larger range of shear rate.

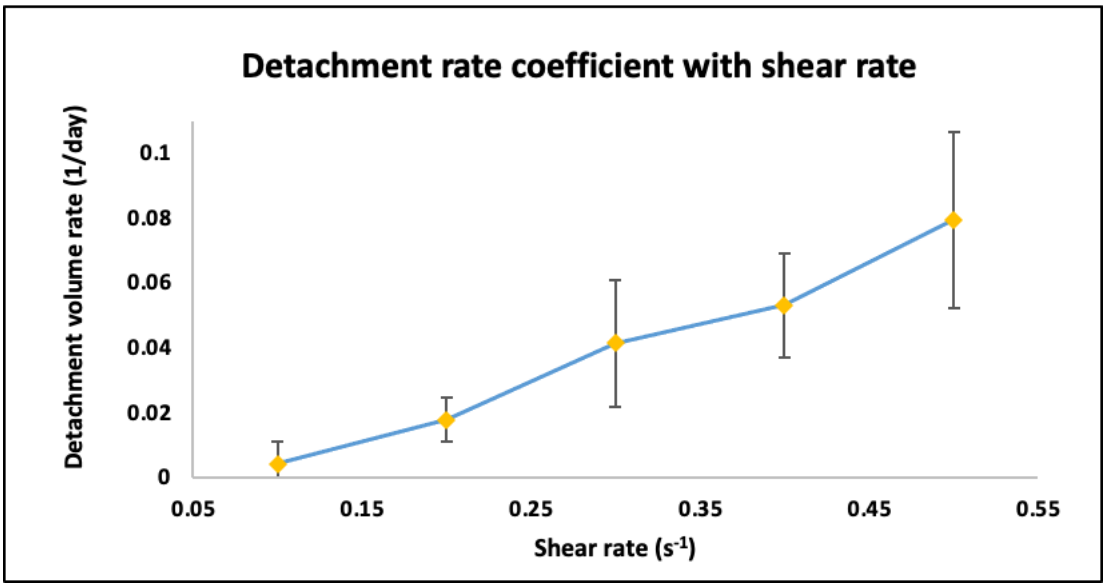

Figure 4.8. The change of detachment rate coefficients with shear rate.

4.3.3 The deformation and detachment of biofilm formed during shear flow

It was found that change in shear stress during biofilm growth could further affect the biofilm detachment [54, 168, 169]. Hence, it is necessary to consider biofilm formed in the shear flow. In this section, the biofilms were grown under a small shear flow during biofilm growth (the shear rate equal to 0.04 s^{-1}) which was then exposed to a high shear flow with the shear rate in the range of 0.1 to 0.5 s^{-1}. Figure 4.9 shown the biofilms grown under static and shear flow conditions, the EPS formation coefficient was kept at 0.18. The morphology of biofilm slightly changed when a small shear flow was applied during biofilm growth.

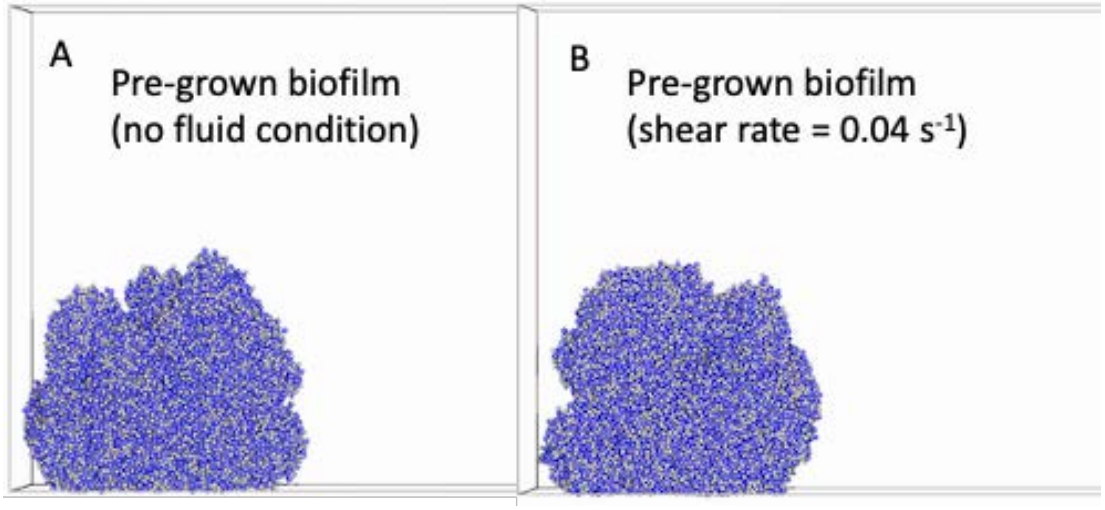

Figure 4.9. Pro-grown biofilm (A) under static condition and (B) under small shear flow. The EPS formation coefficient was kept at 0.18.

Similar to previous work in section 4.3.2, this pro-grown biofilm deformed and slide along the shear flow direction and there has no detachment at shear rate of 0.1 s^{-1} (figure 4.10). When the shear rate increased to 0.2 s^{-1}, the biofilm deformed initially, and a large portion of the biofilm detached at around 13.4 day. This large segment would break again and divide into two small fractions due to the applied shear force (figure 4.11). Similar detachment process has also been found when the shear rate increased to 0.3 and 0.4 s^{-1}. Figure 4.12 displayed the detachment of the biofilm (pre-grown under shear flow) in exposure to the shear flow for 4.57 and 16.15 days. It can be seen that the detached volume increased with the shear rate. At the shear rate of 0.3 and 0.4 s^{-1}, it can be seen that the detached large segment divided into several fractions when subjected to the higher shear force.

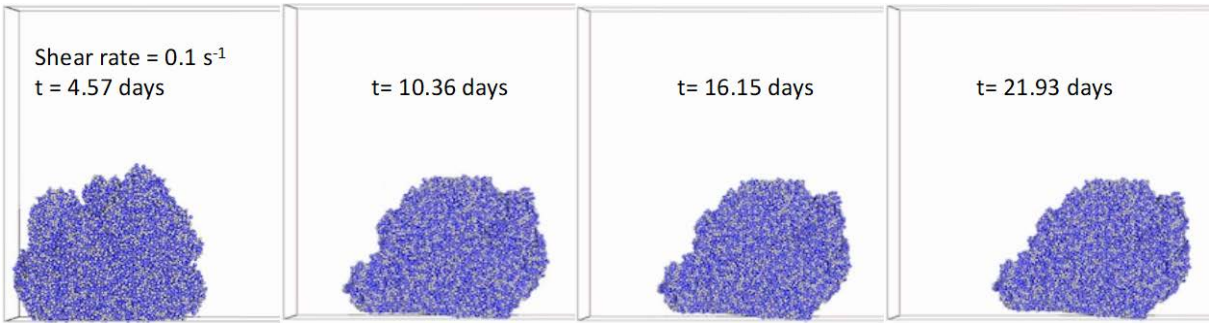

Figure 4.10. Biofilm deformed with the shear flow. This biofilm was pre-grown under small shear flow, then the deformation was monitored by increasing the shear rate to 0.1 s^{-1}.

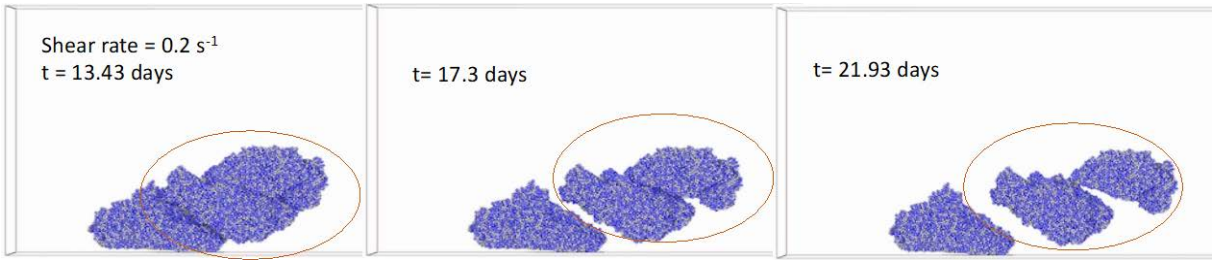

Figure 4.11. A large segment of biofilm detached from the bulk biofilm and broke again due the applied shear force. The shear rate here is 0.2 s^{-1}.

The detachment rate coefficient has also been calculated in this case. As displayed in figure 4.13, for the biofilm grown under a small shear flow, the detachment rate coefficient increased with the shear rate as well. When comparing the detachment rate coefficient for the biofilms grown in static culture, the biofilms grown under a small shear flow seemed to detach more easily at shear rate of 0.2-0.4 s^{-1}.

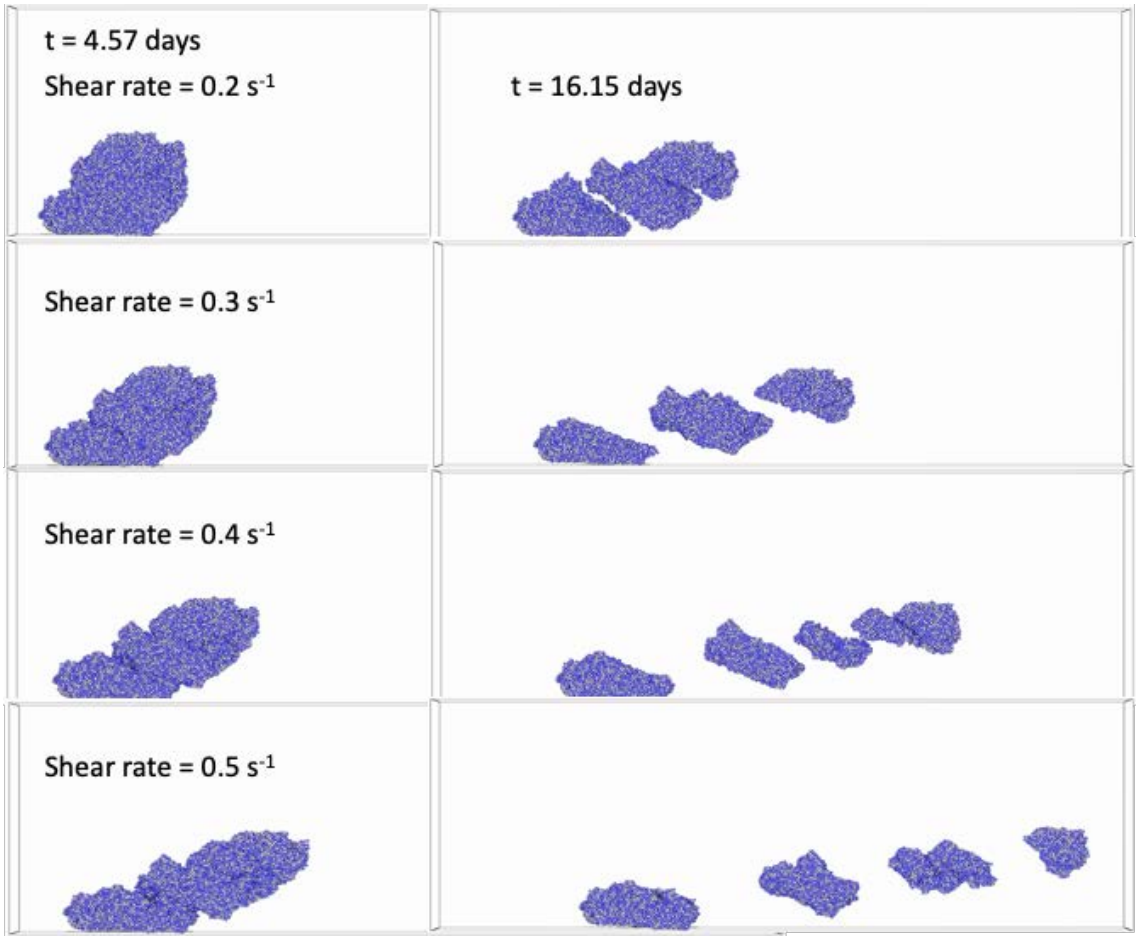

Figure 4.12. Biofilm deformation and detachment at different shear rate. The biofilm was pre-grown under a very small shear flow at the shear rate of 0.04 s^{-1}. Then the deformation and detachment were monitored by increase the shear rate. The shear rate here varied from 0.2 to 0.5 s^{-1}.

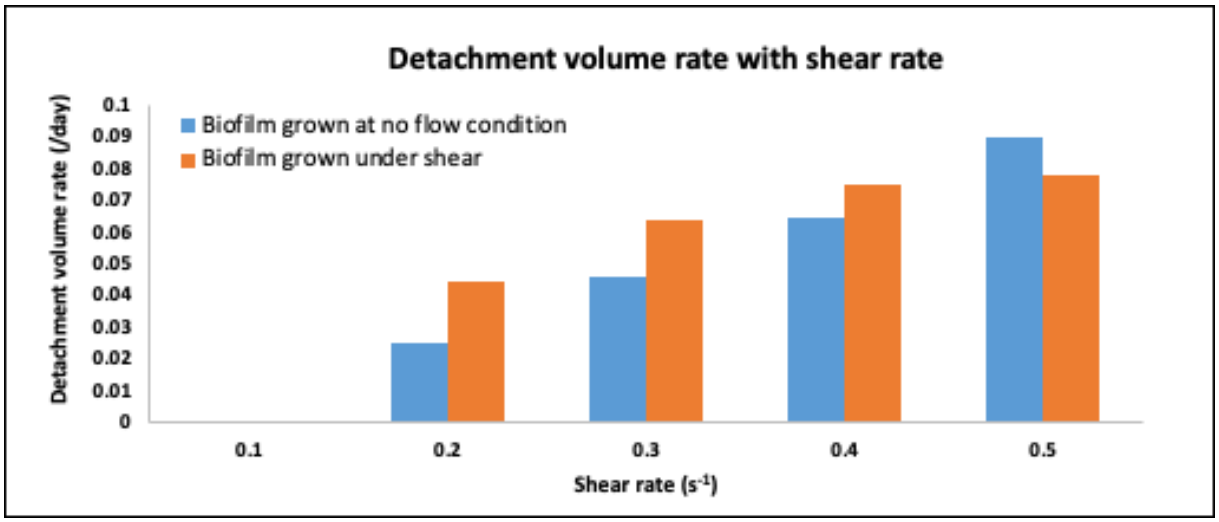

Figure 4.13. Plot of detachment rate coefficients varying with shear rate. The biofilms were grown under shear flow and no shear flow conditions.

It was found that the biofilm slide along the bottom wall during deformation and detachment in all cases, and the sliding distance is directly related to the shear rate (e.g. figure 4.2, 4.3 and 4.8). This phenomenon was caused by strong normal adhesive force between EPS and the bottom wall, in which the first layer of biofilm did not detach from surface but slide along the wall due to the tangential force of flow. Therefore, a frictional force is required in future.

4.4 Conclusion

The detachment of biofilm was predicted based on a mechanistic approach by using the present individual based modelling. The shear flow was applied by using a simple drag model. It was found that when the biofilm exposed to a very small shear flow for prolonged time, the detachment of lager biofilm segments occurred, which was caused by shear failure. The detachment coefficient rate did not have well-defined relationship with the change of EPS amount. The results indicate that when the biofilms exposed to the shear flow with the same inlet shear rate, the detachment of biofilm was primarily determined by the biofilm shape and EPS distribution rather than the EPS amount within the biofilm.

For the biofilm grew at a fixed EPS formation coefficient, the detachment rate coefficient was proportional to the shear rate. The high shear rate led to a large loss of biofilm volume. Besides, when the biofilm grown under a small shear flow, it became easier to deform and detached when the shear rate ranged from 0.2-0.4 s^{-1}.

The results suggested that the present individual based model, which combined biological and physical processes, could successfully mimic the biofilm formation. In addition, the deformation and detachment of biofilms could be predicted by the one-way when the creeping flow was applied ($Re < 1$). However, the steady eddies would generate behind the particles when the Reynolds number is greater than 4 [170]. Therefore, when the biofilms were subjected to the laminar flow with higher Reynolds number, the two-way coupling (CFD-DEM) approach need to be adopted. In which the fluid pattern could be affected by the morphology of biofilm in return. The model will be improved by coupling the present IbM with computational fluid dynamic code-OpenFOAM, which will be presented in Chapter 5.

5 CFD-DEM modelling of biofilm streamer oscillations and their cohesive failure in fluid flow

5.1 Introduction

Biofilms are microorganisms attaching and growing on surfaces, embedded in their extracellular polymeric substances (EPS) [40, 171]. It is well known that biofilms have a significant impact on environment, human health and a wide range of industries. For example, they play an important role in biological waste-water treatment [172]. The presence of biofilms is the major cause for infections of medical devices [173, 174] and the clogging of industrial flow system, such as biofouling in membrane system [175]. They also lead to increased drag on marine vessels [176]. Biofilms can adapt to different environments by forming diverse morphologies [177]. For example, the extracellular matrix can hold the cells together to develop filament-like biofilm structures to resist the fluid shear force and suspended freely with fluid flow [59]. Such filamentous structures of biofilms are referred to biofilm streamers which are ubiquitous in porous media and can accelerate the biofilm induced clogging of medical stents and water purification filters [21, 60, 63]. Valiei et al. fabricated a microfluidic device with an array of micro-pillars to mimic a porous media and they found that biofilm streamers began to emerge between different pillars [62]. It is also found that streamers can form in curved sections of microchannel [24]. A lot of work has demonstrated that biofilm streamers act as precursors to the formation of mature and denser biofilms in porous media, causing rapid and catastrophic clogging in biomedical systems [21, 60, 62, 82]. In which case, the interactions between biofilm streamers and fluid flow are important but remain elusive.

Stoodley et al. have performed experiments to study the flow induced biofilm streamer oscillations, and found that the streamer displacement increased with flow velocity and oscillate in a sinusoidal curve [23]. However, the interaction of local flow with biofilm streamer is difficult to be examined experimentally. Therefore, a continuum model has been developed to study the oscillatory motion of a single biofilm streamer under different flow conditions [82]. Such a continuum model gave reasonable predictions about the overall streamer oscillation characteristics, however, it significantly underestimated the oscillation amplitude of a streamer at low flow velocities. Furthermore, such a model could not predict the breakup of the streamers which has been observed in the experimentation in [23]. In either natural or artificial scenarios, multiple streamers can form at the same time. These streamers can spatially organize in

different patterns. However, there is a lack of computational studies about fluid-structure interactions of multiple biofilm streamers arranged in different spatial configurations. Therefore, this work presents a new computational model to study single and multiple biofilm streamer oscillation and their cohesive failure under different fluid flow. The streamers are modelled using the discrete element method (DEM) and the flow field is computed using Computational Fluid Dynamics (CFD). The DEM was initially developed to study mechanics of granular like materials [144, 178, 179] and has been recently extended to investigate mechanics of living materials such as biofilms [102, 180, 181], cells and tissues [182, 183]. The present model was implemented on SediFoam (https://github.com/xiaoh/sediFoam) which is an open source CFD-DEM tool kit based on LAMMPS [184] (Large-scale Atomic/Molecular Massively Parallel Simulator) and OpenFOAM [185] (Open-source Field Operation and Manipulation). The objectives of the present study are to (1) demonstrate the capability of CFD-DEM of predicting biofilm streamer oscillation in flows, (2) investigate how the spatial arrangement between biofilm streamers effects on the oscillation of streamers, (3) how the flow conditions and spatial arrangement effect on cohesive failure of biofilm streamers.

5.2 Model Domain

Three different case studies were considered: (1) single biofilm streamer (Figure 5.1A); (2) two biofilm streamers in parallel (Figure 5.1B); (3) two biofilm streamers in tandem (Figure 5.1C). The streamer dimensions were taken from experimental measurements reported in [23]. The streamer tail (light blue particles in Figure 5.1A) adhered to its stationary spherical base which was represented as a biofilm cluster (red particle in Figure 5.1A). The biofilm cluster with diameter (D_c) of 0.34mm was fixed in all directions. The length (L) of the streamer is 1.492mm. The simulation box was chosen to be a rectangular channel with the same dimensions (length : 12mm, height: 3.2mm) to another modelling work in [82]. In addition, a small value of width (L_z = 0.5mm) was chosen in the z direction since an empty boundary condition is applied to the front and back wall to simplify the simulation (OpenFOAM User Guide).

A uniform velocity profile was implemented at inlet flow boundary (x = 0). The velocity was fixed at the inlet of the channel and had a zero gradient boundary condition at outlet. The deformation of the streamer was only monitored after it reached constant maximum amplitude. The pressure here was enforced as zero gradient at the inlet patch and zero value at the outlet patch. To avoid boundary effects on the streamers, slip boundary condition was used at the top

and bottom walls such that there is no boundary layer development on the channel walls [82, 186]. Table 1 and 2 show the velocity and pressure boundary condition setting in OpenFOAM.

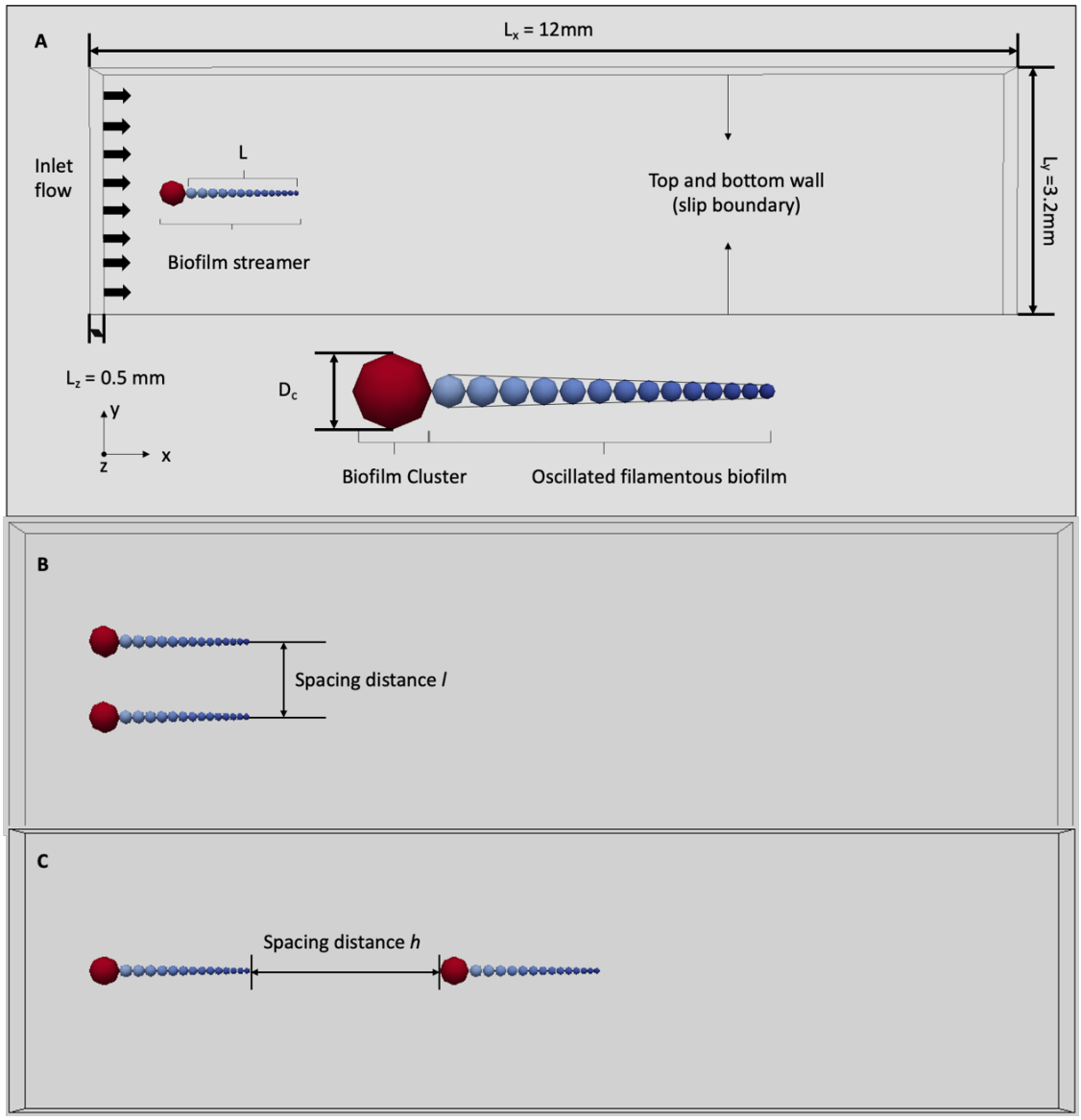

Figure 5.1. Summary of the model for (A) single biofilm streamer, (B) side-by-side biofilm streamers and (C) in-line biofilm streamers.

Table 5.1 Boundary condition for U (velocity)

Patch	Type	value
Inlet (left)	fixedValue	0.1-0.4 m/s
Outlet (right)	zeroGradient	--
Walls (top and bottom)	slip	--

Table 5.2 Boundary condition for P (pressure)

Patch	Type	value
Inlet (left)	zeroGradient	--
Outlet (right)	fixedValue	0
Walls (top and bottom)	zeroGradient	--

5.2.1 Single streamer

The biofilm streamer length (L) was normalized by the maximum width (D_c) in this section. We initially investigated the deformation of a single streamer (L/D_c = 4.4) subjected to flow velocity from 0.1 m/s to 0.4 m/s (corresponding Reynolds number 34-136, which was calculated by using D_c as the characteristic length). However, the streamer length varied in experiments because of different biofilm types and flow conditions [187, 188]. Therefore, it was useful to study the effect of the length of a biofilm streamer on its oscillation. In the present simulations, lower values of L/D_c (i.e. 1 and 2.5) were also investigated.

5.2.2 Two streamers in parallel

Two parallel biofilm streamers were considered to study the interaction between them. As shown in Figure 1B, the spacing distance l (i.e. the centreline distance of the two streamer tails) varied from 0.4 to 1.15 L while the inlet velocity was fixed at 0.4 m/s. The effect of flow velocity on the oscillation of parallel biofilm streamers was also investigated by keeping spacing distance as constant.

5.2.3 Two streamers in tandem

In this case, we varied the spacing distance h (i.e. distance between the tail end of the upstream streamer and the head of the downstream streamer) between 0 and 2L (Figure 1C) at inlet flow velocity of 0.4 m/s. In addition, the streamers oscillation under different flow conditions have been investigated by keeping spacing distance h as constant.

5.3 Methodology and parameters

The conceptual biofilm streamer was constructed by 15 particles with decreasing radii as shown in Figure 1A. Each particle has representative properties of biofilms. In the CFD-DEM approach, the particle motion is calculated based on Newton's second law (equation (3.20). The contact force between two collided DEM particles i, j is calculated by using the Kelvin-Voigt model (equation 3.18). The cohesive force among the biofilm particles is computed by equation

(3.21). The fluid flow is described by locally-averaged incompressible Navier-Stokes equations ((3.22a) and (3.22b)). The fluid particle interaction force is calculated by equation (3.24). The Reynolds number is in the range of 34-136 in this study.

Table 5.3 shows the key input parameters for the simulations. Depending on biofilm types, growth conditions and test approaches, the Young's modulus of biofilms could vary over several orders of magnitude [54, 189-191]. In this work, the equivalent Young's modulus of biofilm was 11Pa which is similar to the biofilm streamer of mixed *P. aeruginosa* strains as reported in [54]. A large cohesive energy was chosen to represent cohesive properties of the biofilm streamer [120, 192] since EPS is the major component in biofilm streamer [22]. The bacteria density was often very similar to water with 1% difference [193], and we have demonstrated that such minor difference has negligible effect on the oscillation of single streamer. Therefore, the density of biofilm streamer was assumed to be the same to water in this work.

Table 5.3 Simulation parameters.

Numerical simulation parameters	
Density of particles	10^3 kg m^{-3}
Elastic constant for normal and tangential contact ($k_n = k_t$)	10 Pa [54]
Cohesive strength	1×10^{-15} J [120]
Fluid dynamic viscosity	1×10^{-3} kg m^{-1} s^{-1}
Fluid density	10^3 kg m^{-3}
Normal damping constants	10^{13} m^{-1} s^{-1}
Tangential damping constants	10 m^{-1} s^{-1}

5.4 Results and discussions

5.4.1 Oscillation of one single biofilm streamer in a fluid flow

The oscillation amplitude and frequency were investigated for the inlet flow velocity between 0.025 and 0.4 m/s. Figure 5.2A shows the streamer configuration and corresponding velocity field at 0.05 s at flow velocity of 0.4 m/s. It can be seen that the vortexes generated when flow passed the biofilm cluster and continuously shed from each side of this cluster, resulted in streamer oscillation. The predicted maximum displacement and oscillation frequency of the streamer tip were 198.5 µm and 220 Hz (Figure 5.2B), respectively, which quantitatively agreed with experimental observations of [23].

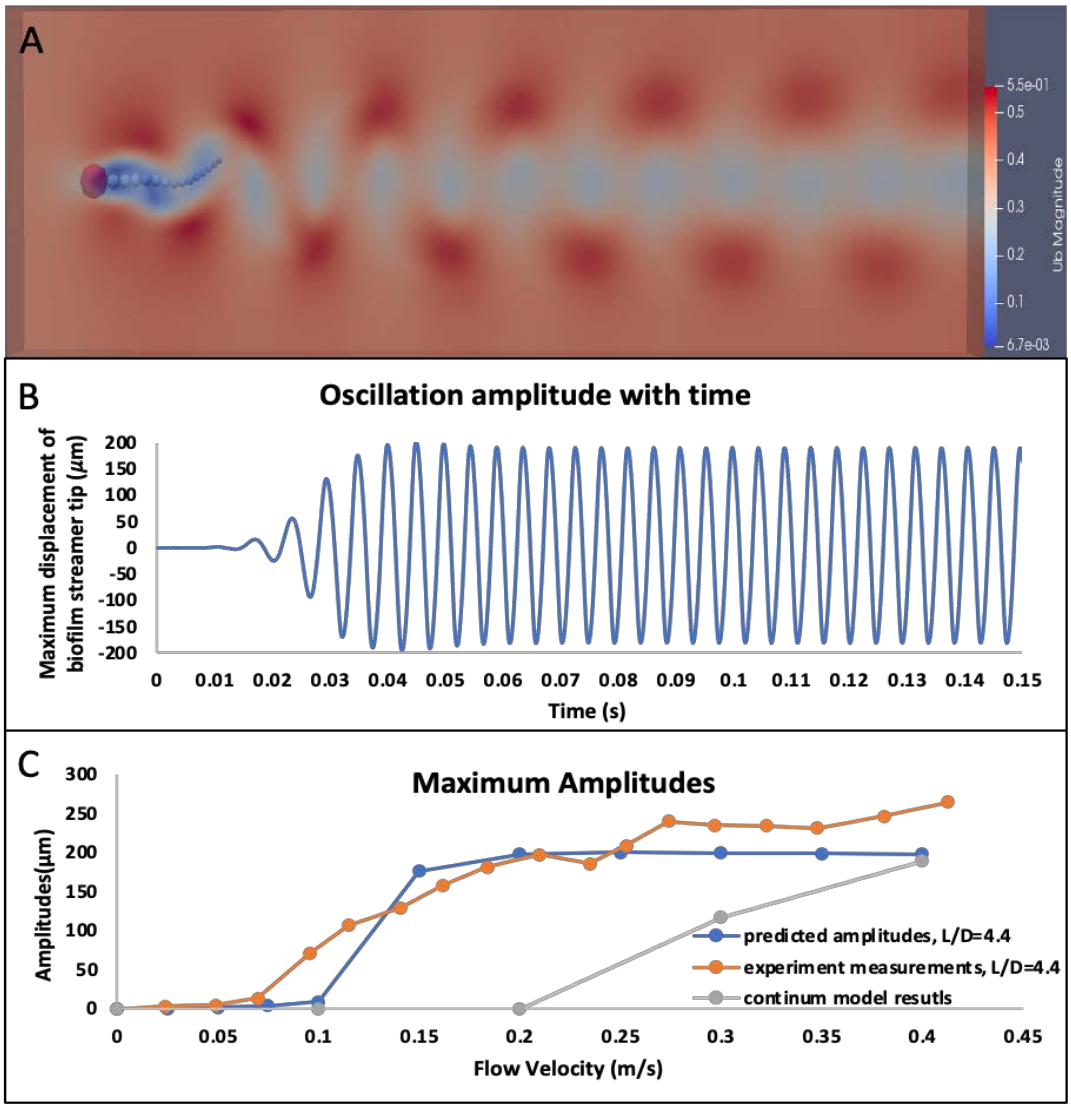

Figure 5.2. (A) Flow patterns behind the streamer; (B) The temporal oscillation amplitudes of inline biofilm streamers tip at flow velocity of 0.4 m/s; (C) Maximum amplitudes of biofilm streamer tip determined by the present study, experiments results as well as numerical simulations reproduced in [23, 82].

Figure 5.2C compares the biofilm streamer oscillation amplitudes determined by experimental measurements [23], a continuum model [82] and the present study. At the considered flow velocities, it seemed that there were three stages of streamer oscillation characteristics predicted by CFD-DEM simulations : (1) Stage 1: biofilm streamer slightly vibrated at very low fluid flow velocity; (2) Stage 2: oscillation amplitude increased sharply when the velocity exceeds 0.1 m/s (comparable to the 0.075 m/s as found in experimental measurements); (3) Stage 3: The increase of maximum amplitude of streamer tip slowed down when the velocity exceeds 0.15 m/s, which was very close to the transition point (0.2 m/s) found in experimental measurements [23]. When the flow velocity rose to 0.25 m/s, the amplitude in the present simulations almost reached plateau, about 200.1 μm and remained steady with further increase in velocity. Meanwhile, the biofilm streamer oscillation amplitude in the experiment was around 209.3 μm at similar velocity (0.253 m/s) and sustainably grew with velocity.

Figure 5.3A displays the oscillation amplitudes of biofilm streamer with different L/D_c subjected to varied flow velocities. The streamer oscillation amplitude was proportional to their tail length under the same flow condition. In addition, the peak displacement of each biofilm streamer occurred when the flow velocity is around 0.25 m/s and slightly decreased with further increase in velocity. Besides, it was noted that for streamers of various lengths, the oscillation amplitudes were all very small (3.25-9.4 μm) when the velocity is under 0.1 m/s (Reynolds number = 34). It could be because the viscous force is dominant at low flow velocity and drains eddy energy to against vortex shedding. Similar results were found by Sumer et al. that when Reynolds number is under 40, there is only a fixed pair of symmetric vortices and no vortex shedding [194]. In our simulations, the oscillation was observed when Reynolds number is far greater than 34 which suggested that the streamer oscillation was directly caused by vortex.

As seen in figure 5.3B, the frequency of streamer oscillation increased with flow velocity which was in agreement with the experimental observations [23]. However, the oscillation frequency appeared independent from the streamer length. Since the oscillation of streamer was caused by the vortex shedding from the upstream biofilm cluster, the dimensionless parameter Strouhal number (S_t) could be adopted to describe the oscillation [23, 82, 195] as:

$$S_t = \frac{f D_C}{u} \tag{5.1}$$

The diameter of the upstream biofilm cluster D_c is used as the characteristic length here, f is the frequency of vortex shedding and streamer oscillation, u is the inlet velocity of the fluid flow. The Strouhal number increased with Reynolds number initially and was close to 0.2 when

the Reynolds number exceed 104 (Figure 5.3C), which was consistent with the results from other simulations of flow past cylinders [196, 197].

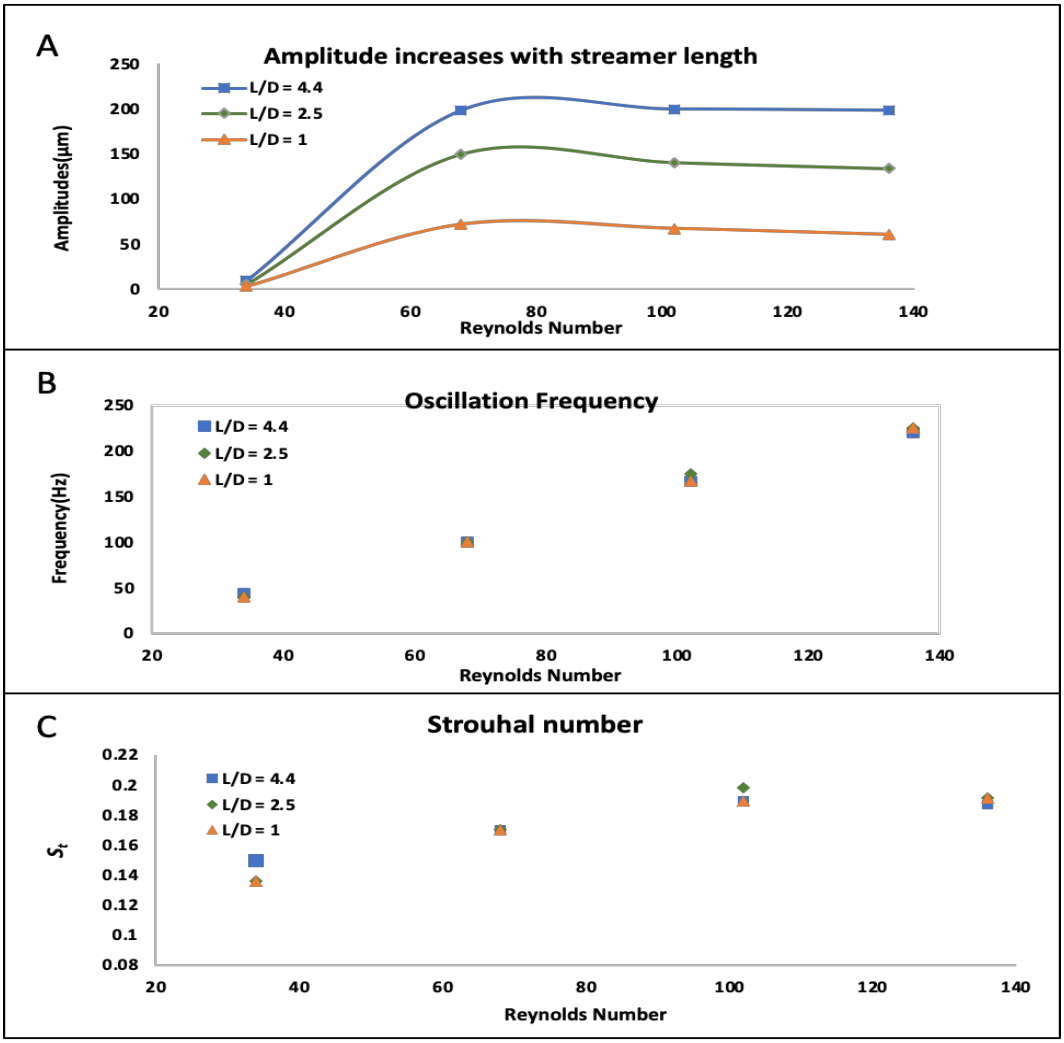

Figure 5.3. The (A) oscillation amplitudes, (B) frequency of streamer of different length and (C) Strouhal number vs. Reynolds number for fluid velocity ranging from 0.1 to 0.4 m/s.

5.4.2 Two streamers in side-by-side arrangement

Different regimes of biofilm streamers interaction depending on the spacing between them have been observed and presented in the following as a function of the ratio of spacing distance to biofilm streamer length l/L. An image of biofilm streamer experiment [23] has shown two parallel streamers which are head-aligned and similar-sized, they flapped in the flow. Likewise, the spacing distance (l/L = 0.4) between two side-by-side biofilm streamers was initially adopted in the model. Vortex shedding formed when flow passed the side-by-side streamer clusters which led to streamers oscillation. As displayed in figure 5.4A, the two biofilm streamers behaved as twin streamers due to in-phase flapping. The maximum oscillation

amplitudes of the two streamers were about the same, 126.2 µm and 126.4 µm, respectively (Figure 5.5A). In addition, the oscillation frequency of both streamers was about 250 Hz (Figure 5.5A).

The maximum amplitude here was smaller than the amplitude of single flapping streamer due to the strong mutual interaction between them which could be caused by coupled near-wakes. When *l/L* exceeded 0.56 (Figure 5.4B), the two streamers oscillated on an out-of-phase mode. In this case, the maximum amplitude and frequency of these two streamers were the same, 154.3 µm and 250 Hz (Figure 5.5B). As presented in figure 5.4C, when further increasing the gap equal to streamer length (*l/L* = 1), the interaction between the two biofilm streamers weakens due to the reduction of mutual interference among them. The maximum amplitude of oscillation slightly grew to 175.15 µm while frequency kept at 250 Hz (Figure 5.5C). These results suggested that as the spacing distance increased, oscillation amplitude of two parallel streamer rose with the remained frequency.

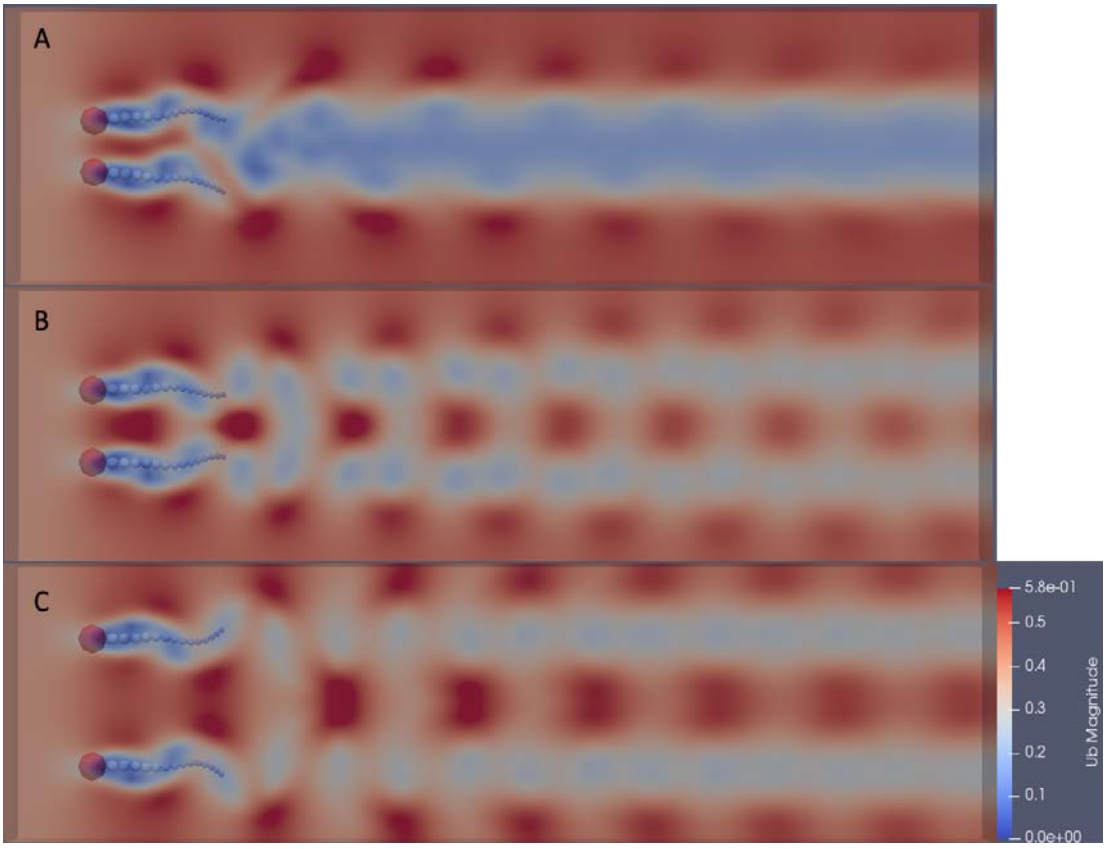

Figure 5.4. Flow patterns behind two side-by-side biofilm streamers with (A) *l/L* = 0.4, (B) *l/L* = 0.56 and (C) *l/L* = 1 at the inlet velocity of 0.4 m/s and t = 0.1 s.

A positive correlation was found between oscillation amplitude and spacing distance (Figure 5.6). The graph shows a sharp rise in oscillation amplitude during the in-phase flapping regime

(0.4 < *l*/*L* < 0.51). On the out-of-phase oscillation mode (*l*/*L* > 0.56), the maximum amplitude of oscillation slightly grew with the spacing distance and finally remained around 175.21 µm. One reason for this phenomenon may be the vortex shed from two biofilm clusters and strongly affect each other on the out-of-phase mode. It is important to note that the oscillation frequency did not change in all cases because of consistent flow velocity. This indicated that the frequency only related to the fluid velocity which agrees with previous results of single streamer oscillation. To further verify this behaviour, the fluid velocity has been decreased for side-by-side streamers at spacing distance *l*/*L* = 1. As a result, the oscillation frequency of these two streamers decreased to 180 Hz when the fluid velocity is 0.3 m/s (Figure 5.7A), further declined to 120 Hz at fluid velocity of 0.2 m/s (Figure 5.7B), which are comparable to what was shown in figure 5.3B. Besides, there was no significant change in oscillation amplitude.

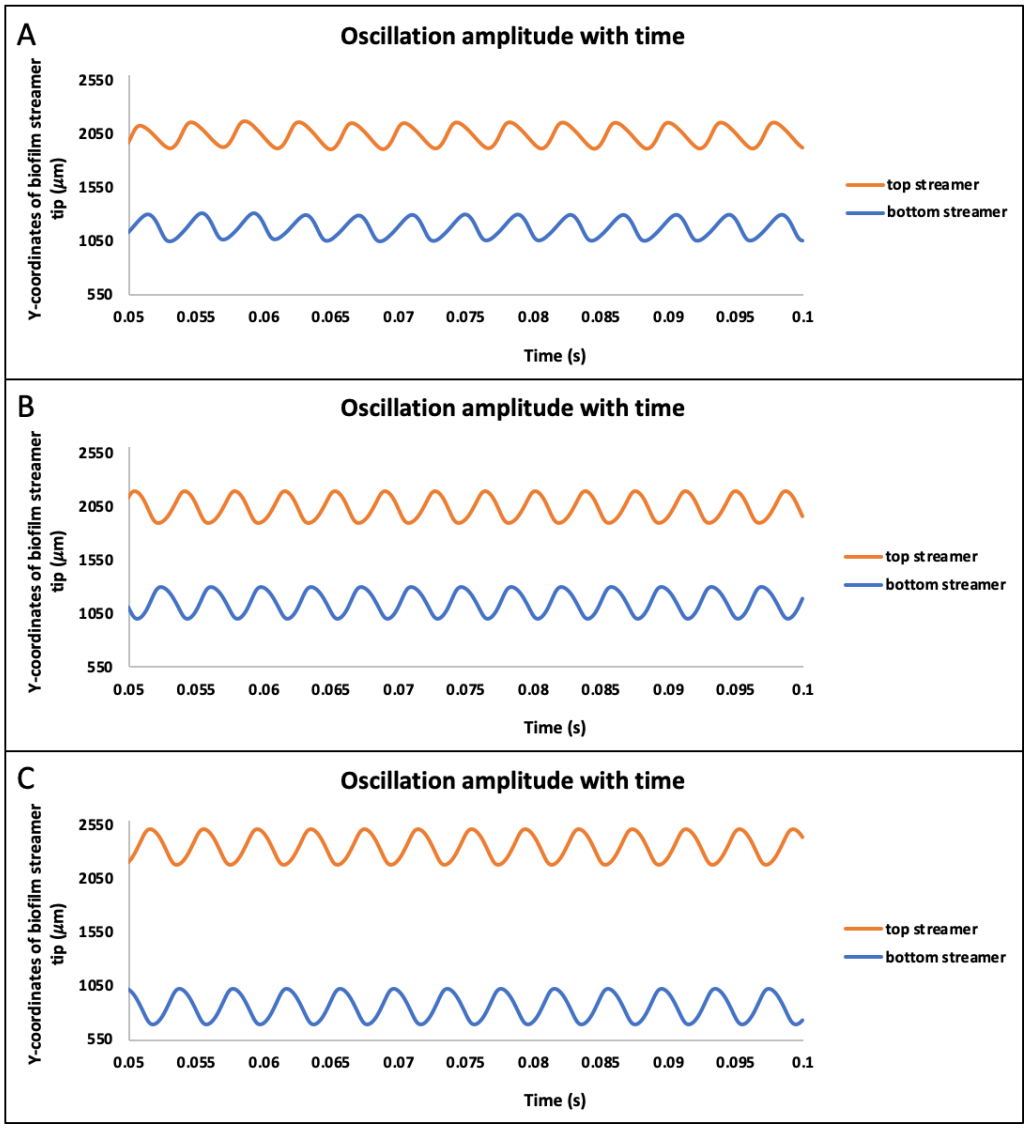

Figure 5.5. Oscillation amplitude and frequency of two side-by-side biofilm streamers with spacing (A) *l*/*L* = 0.4, (B) *l*/*L* = 0.56 and (c) *l*/*L* = 1.13, subjected to the inlet flow velocity of 0.4 m/s.

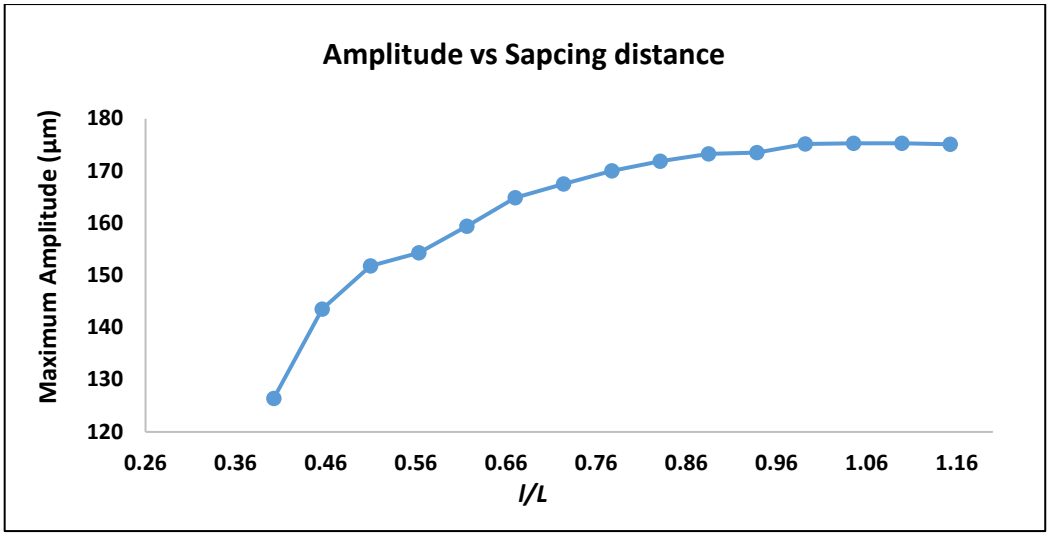

Figure 5.6. Maximum oscillation amplitude of side-by-side biofilm streamers changes with *l/L* at the inlet flow velocity of 0.4 m/s.

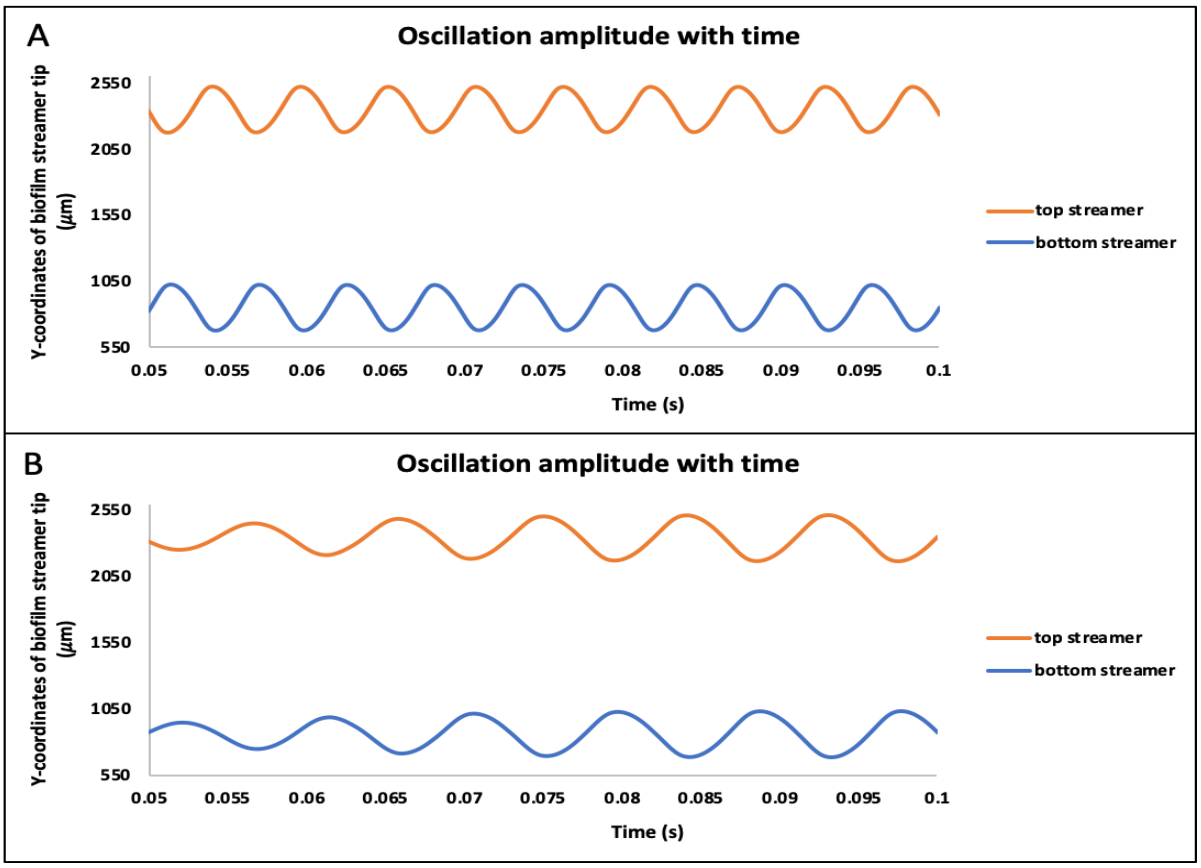

Figure 5.7. Oscillation amplitude and frequency of two side-by-side biofilm streamers with spacing *l/L* = 1 subjected to the inlet flow velocity of (A) 0.3 m/s and (B) 0.2 m/s, respectively.

5.4.3 Two biofilm streamers in tandem arrangement

For the two biofilm streamers in tandem arrangement, when the spacing distance was zero, the tail of upstream streamer initially adhered to the biofilm cluster of the downstream streamer because of their cohesive properties (Figure 5.8). After around 0.035 s, the oscillation started from the downstream streamer because the fluid behind it could move freely. Meanwhile, the upstream streamer tended to oscillate, which finally caused the cohesive failure at the streamer tip. Afterwards, the remaining upstream biofilm streamer oscillated in the flow due to the vortex shedding.

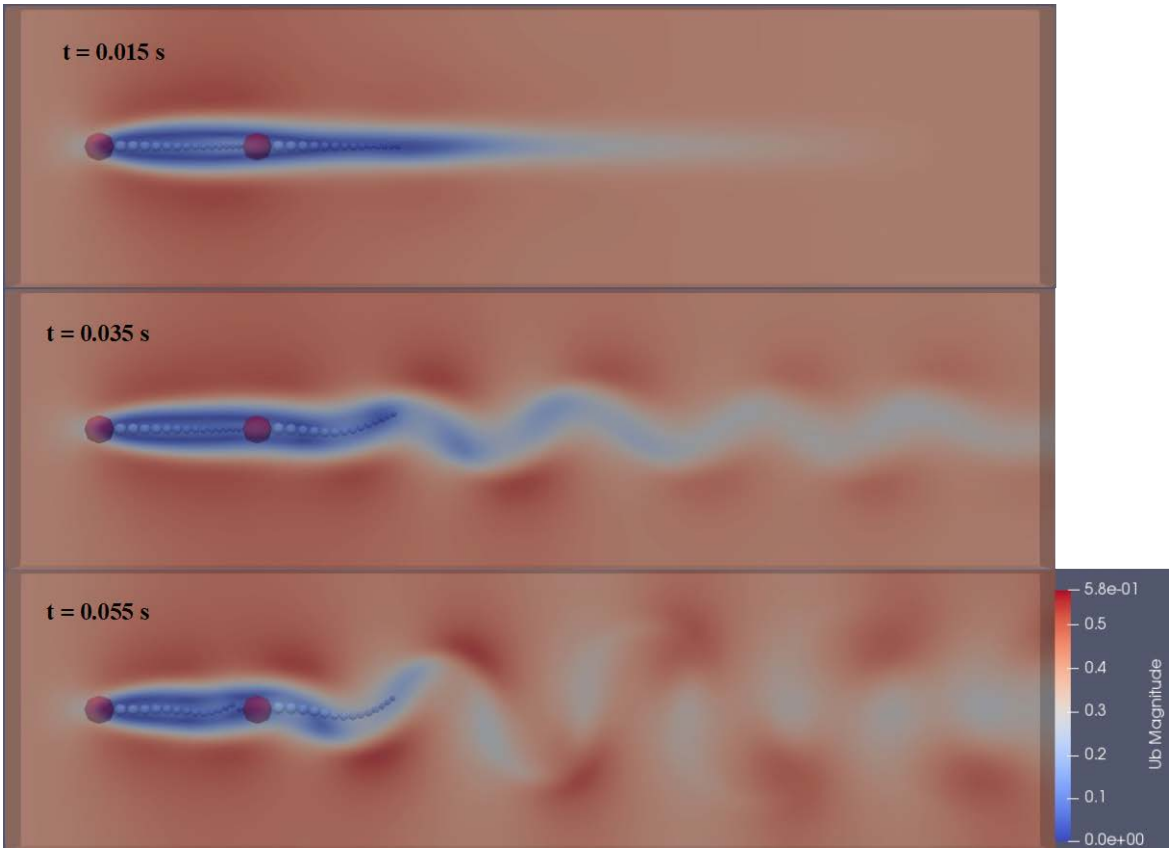

Figure 5.8. Temporal oscillation of in-line streamers with h/L = 0, at flow velocity of 0.4 m/s.

A different behaviour was captured when the spacing distance is increased to h/L = 0.25. As seen in figure 5.9A, it was apparent that the upstream streamer particles are staggered and moved along the opposite direction of the x-axis. This behaviour suggested that the upstream biofilm streamer was affected by a recirculating flow. Consequently, the recirculating zone was found between them which caused upstream biofilm streamer moving against flow (Figure 5.9B). This recirculating zone disappeared over time as shown in figure 5.10. However, the upstream biofilm streamer was still stationary since the shear layer enclosed the gap between

two biofilm clusters. It started beating the flow at time of 0.04 s when the shear layer was about to break which resulted in vortex formation. Subsequently, the already flapping downstream biofilm streamer also experienced the impingement of the vortex which shed from the upstream biofilm cluster. Thereby, the downstream streamer had a large deformation during this period (Figure 5.11). Then the vortex shed from the upstream biofilm cluster gradually merged with those forming from the downstream biofilm cluster and totally coupled at around 0.09 s causing an out-of-phase flapping of the two streamers. The deformation of the downstream streamer weakened after the co-shedding process since the combined vortices became weaker. In the same vein, the results in figure 5.11 shows the maximum displacement of the tip of downstream streamer sharply increased during impingement period, then slowly decreased during the co-shedding period and finally reached a minimum value equal to 187.75 µm. The oscillation amplitude of the upstream streamer kept around 195.6 µm. In addition, oscillation frequency of these two streamers were the same here about 220 Hz.

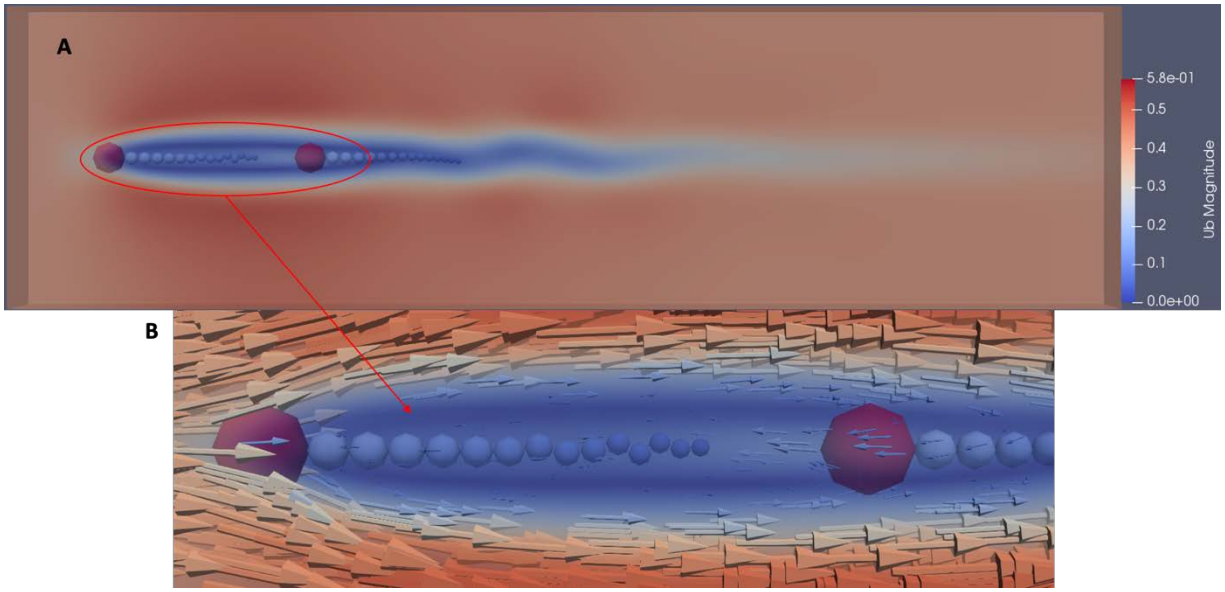

Figure 5.9. The behaviours of inline biofilm streamers (*h/L* = 0.25) at v = 0.4 m/s and t = 0.08 s.

The recirculating zone disappeared when *h/L* reached 0.75. In this case, the two streamers could beat the flow simultaneously (Figure 5.12A). The oscillation amplitude of upstream biofilm streamer remains around 188.9 µm. Similarly, the downstream streamer also had large deformation during the impingement period and flapped gently after the co-shedding period with an oscillation amplitude of 114.45 µm. The frequency of oscillation kept at 220 Hz because of the unchanged flow velocity (Figure 5.12B). The oscillation amplitude of downstream streamer decreased with the increase in spacing distance *h/L*, and the value was always smaller

than that of the upstream streamer (Figure 5.13). This indicates the downstream streamer would undergo a smaller drag force with increased spacing distance. In contrast, the downstream streamer experienced a lower fluid stress which agreed with the drafting effect, which referred to the fact that the downstream object was generally subjected to a drag reduction compared to the upstream object [198].

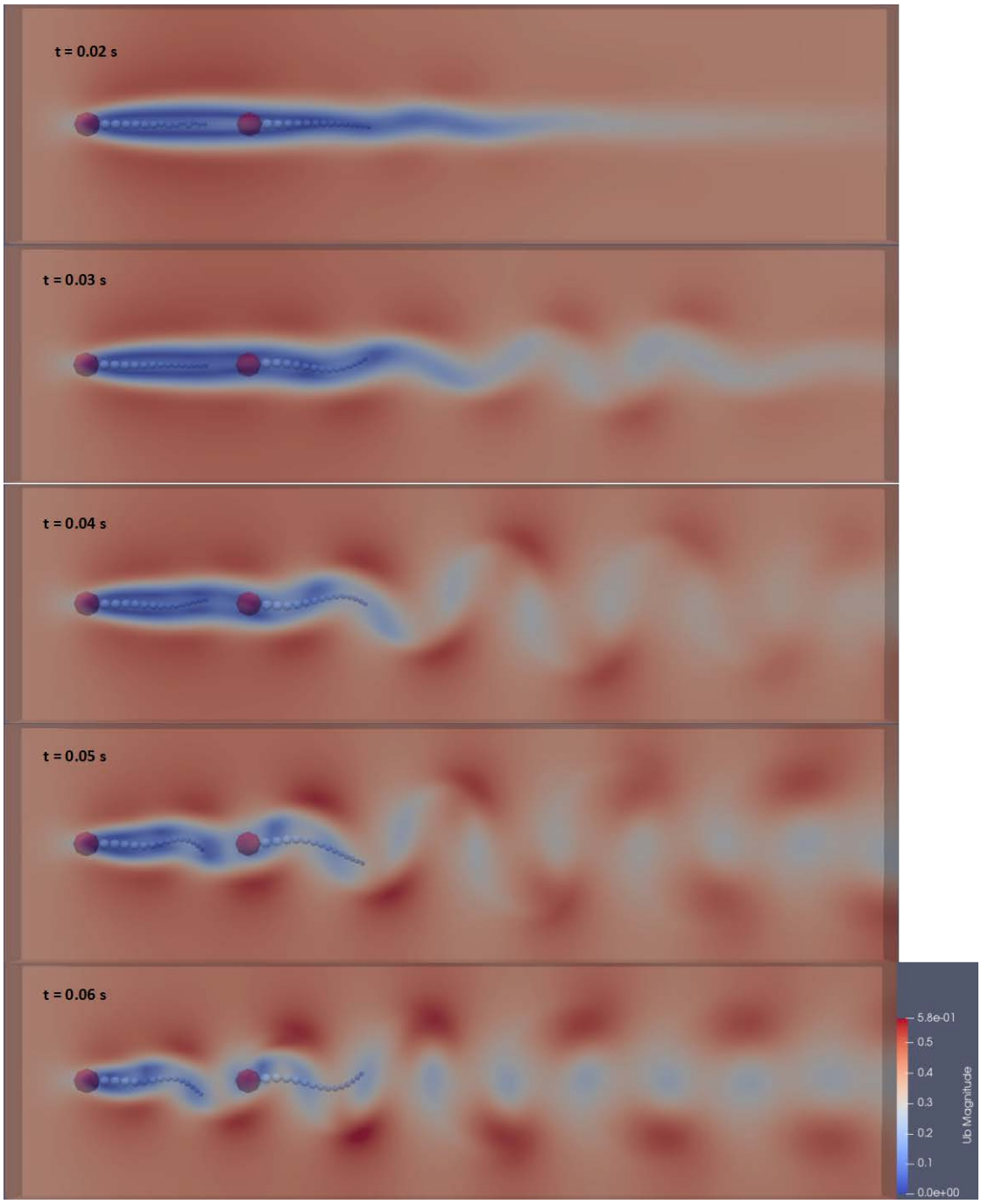

Figure 5.10. Flow patterns behind two inline biofilm streamers with of *h/L* of 0.25 subjected to inlet velocity of 0.4 m/s.

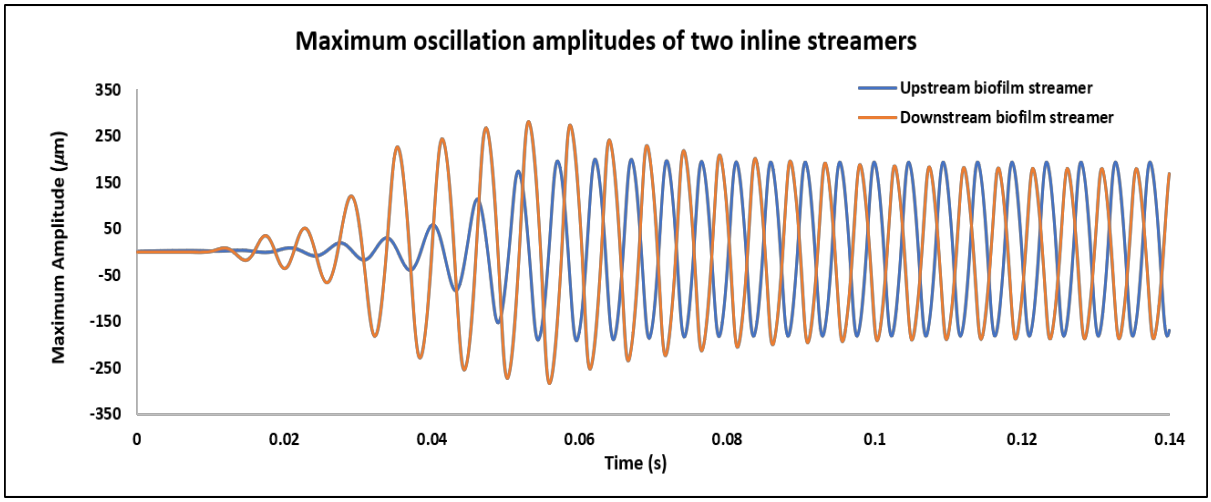

Figure 5.11. Oscillation amplitude and frequency of inline biofilm steamers with spacing distance *h/L* = 0.25 at inlet flow velocity of 0.4 m/s.

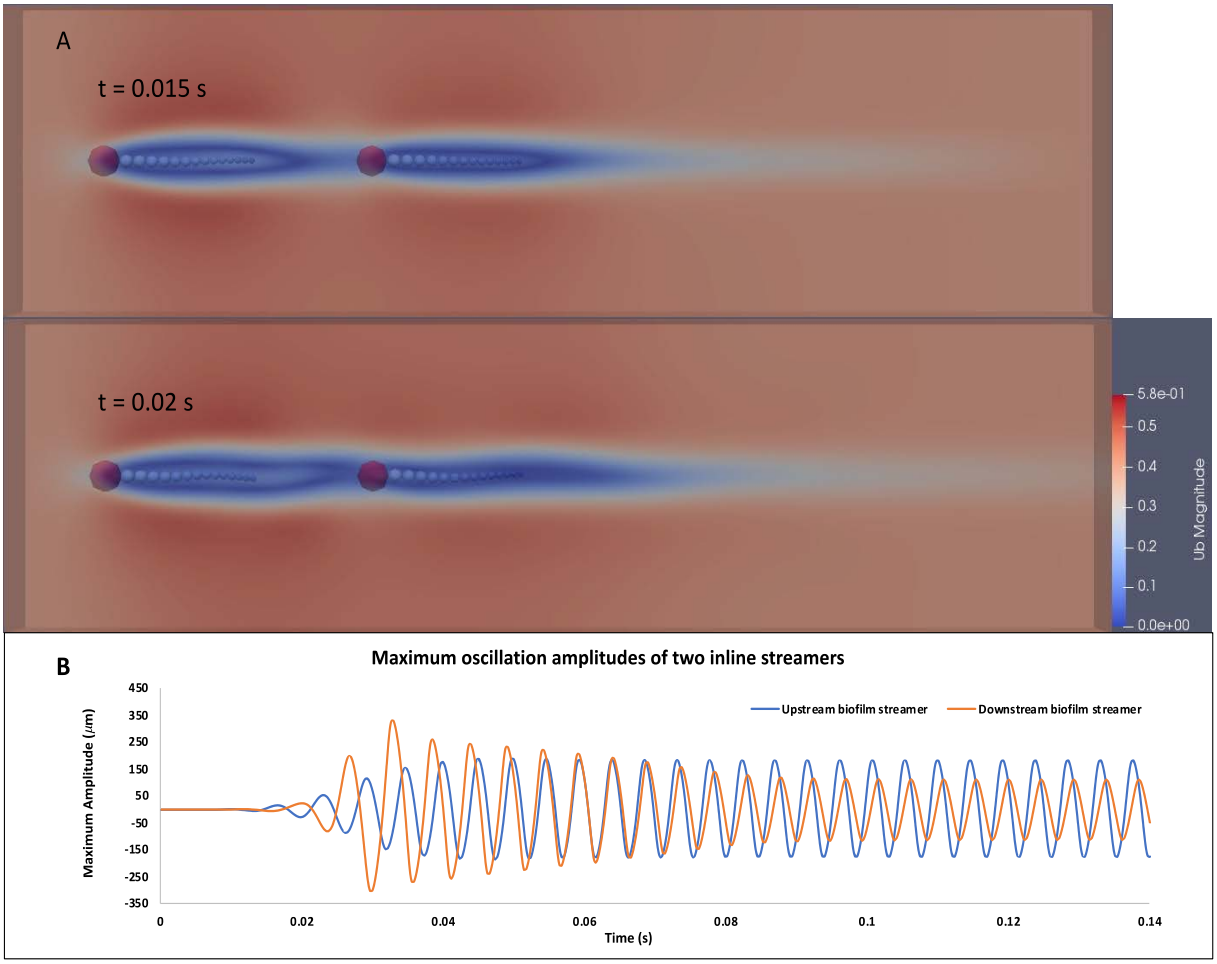

Figure 5.12. (A) The flow pattern and oscillation of inline biofilm streamers (*h/L* = 0.75) at flow velocity of 0.4 m/s at 0.015 s and 0.02 s. (B) The temporal oscillation amplitudes of inline biofilm steamers at flow velocity of 0.4 m/s.

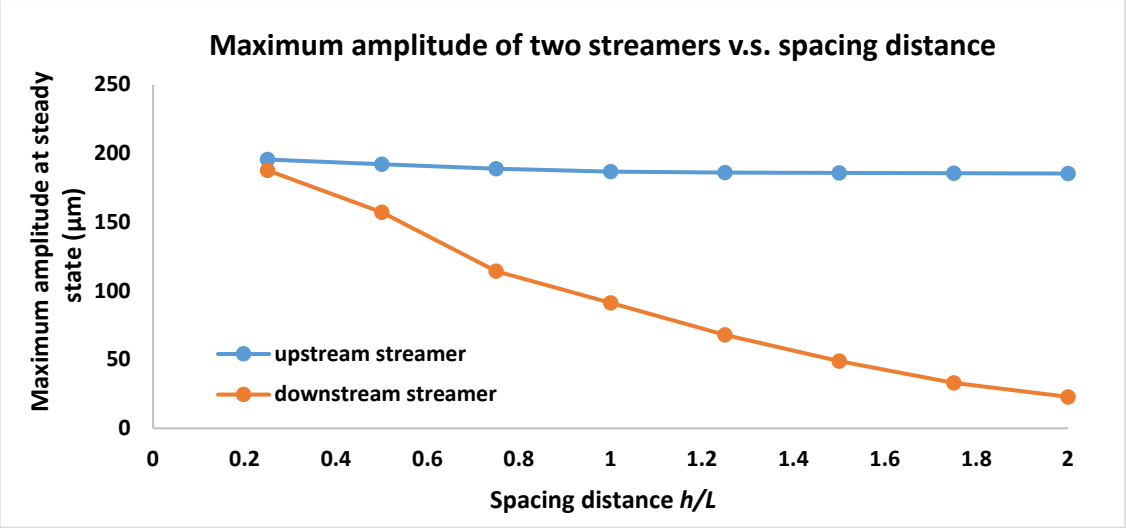

Figure 5.13. Maximum oscillation amplitude of inline biofilm streamers with different spacing distance (*h/L*) at flow velocity of 0.4 m/s.

Biofilm streamer oscillation at different velocity has been investigated by keeping the spacing distance *h/L* as 1. Flow velocity here was varied from 0.2 m/s to 0.4 m/s since the biofilm streamer has significant oscillation when the flow velocity was greater than 0.1 m/s. Consistent with previous results, the frequency of inline streamers oscillation increased with the flow velocity (Figure 5.14 and Figure 5.15). However, it was found that the oscillation amplitude of the upstream streamer was smaller than that of the downstream streamer at flow velocity of 0.2 m/s, which might suggest that the drafting effect could not be straightforwardly inherited by the flapping streamer at smaller flow velocity. This invert drafting effect has also been found in other deformable bodies, such as experimental and numerical researches of flapping soap films [198, 199].

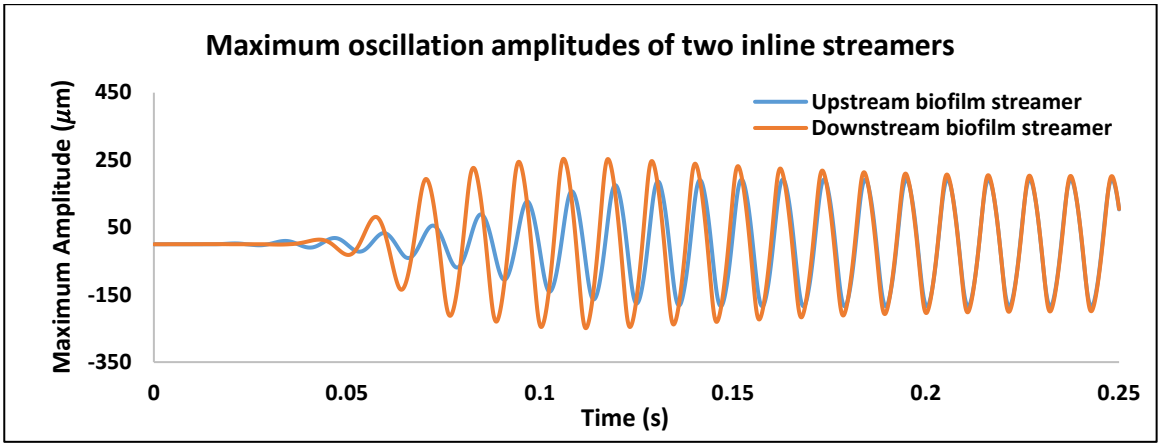

Figure 5.14. Oscillation amplitude and frequency of inline biofilm streamers with spacing distance *h/L* = 1 at inlet flow velocity of 0.2 m/s.

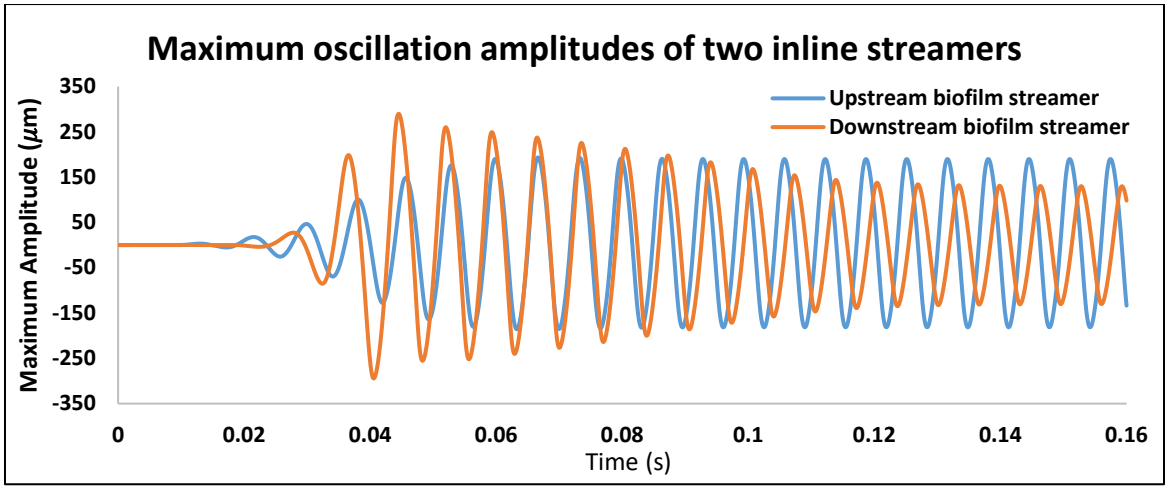

Figure 5.15. Oscillation amplitude and frequency of inline biofilm streamers with spacing distance *h/L* = 1 at inlet flow velocity of 0.3 m/s.

5.4.4 The cohesive failure of streamers

To study the cohesive failure of biofilm streamers, the inlet fluid velocity was increased from 0.4 m/s at a constant acceleration of 16 m/s^2. The critical velocity at which the biofilm streamer was broken up was calculated. Each simulation was stopped once any broken streamer reached the downstream end of the channel and we will only focus on cohesive failure of streamers within this period. For the single isolated streamer, when the flow velocity reached 1.39 m/s, the breakup of the biofilm streamer occurred as seen in Figure 5.16A. For two streamers in parallel, the biofilm streamers started to break up when the flow velocity reached 1.25-1.3 m/s depending on the distance between the two streamers (Figure 5.17A). The two streamers broke almost simultaneously at the same point when they were on the in-phase oscillation mode (Figure 5.16B). The corresponding critical flow velocity was around 1.25 m/s in this case. However, when the two streamers were on out-of-phase mode, those streamers broke at different timepoints. The locations of the breakup appeared to be random. For example, the one of the streamers broke slightly towards the tail. Shortly after that, another streamer broke up at the point towards the head (Figure 5.16C). Overall, the critical fluid velocity for parallel biofilm streamers breakup seemed to be positively correlated to the spacing distance (*Pearson correlation coefficient* = 0.7) (Figure 5.17A). For two streamers in tandem, the upstream streamers always broke first because they were subjected to higher fluid shear forces. The cohesive failure seems taking place slightly towards the head or slightly towards the tail. For the former, the detached streamer segment would impinge into the downstream streamer which caused almost the entire downstream biofilm to break (Figure 5.16D). For the latter, the

detached streamer segment moved away, and the downstream streamer could keep oscillating with the flow (Figure 5.16E). As illustrated in figure 5.17B, when the spacing distance is less than 1.25L, the critical flow velocity to cause cohesive failure of the upstream streamer seemed to decrease with the gap. However, this threshold value remained around 1.5 m/s when further increase of the spacing distance.

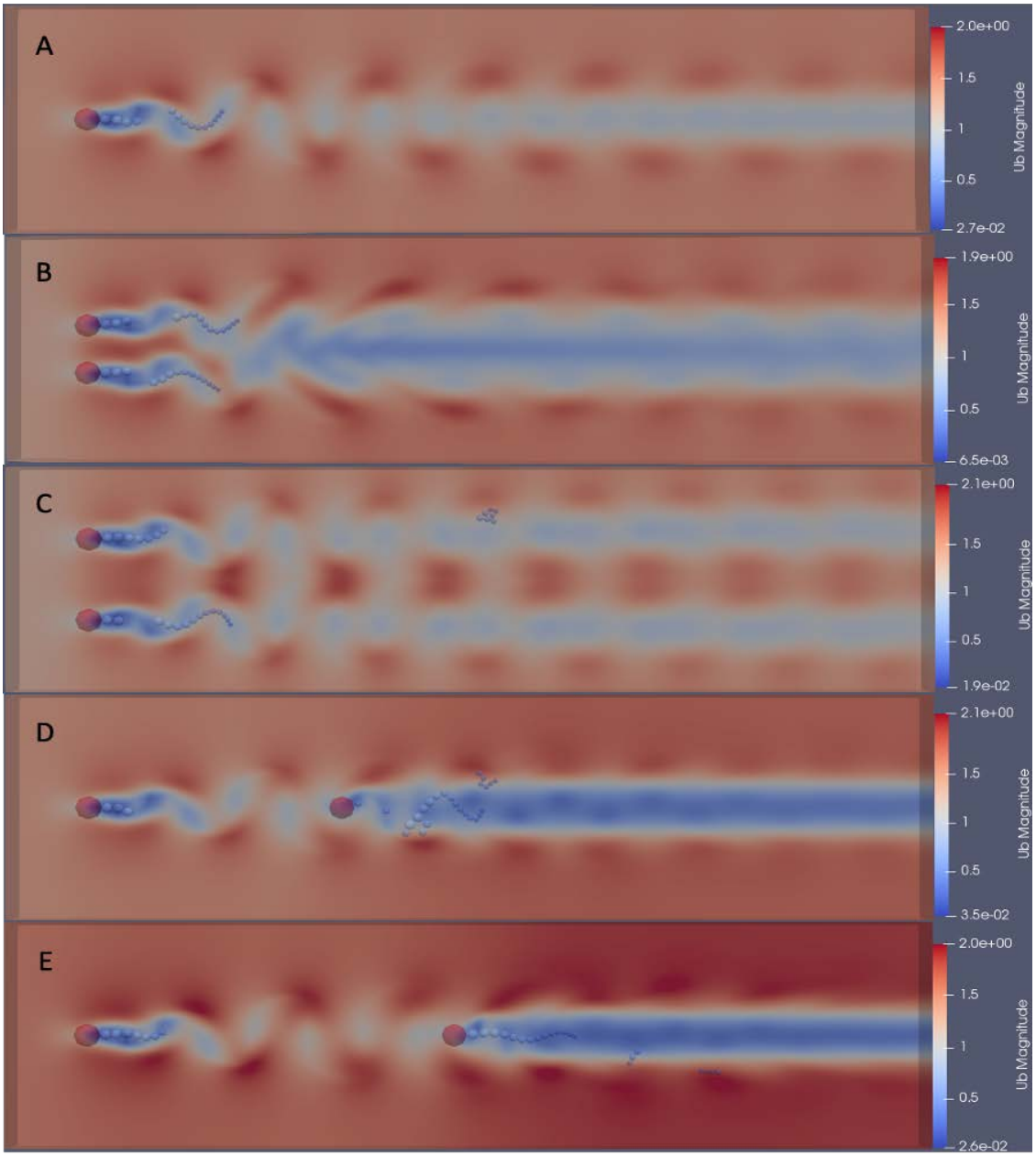

Figure 5.16. The comparisons of cohesive failure of streamers for (A) a single streamer (v = 1.39 m/s). The breakup of two parallel streamers (B) on in-phase mode, where l/L = 0.46 (v = 1. 255 m/s) and (C) on out-of-phase mode, where l/L = 0.78, the critical velocities to cause biofilm streamers to break were 1.25 m/s (top streamer) and 1.32 m/s (bottom streamer). The breakup of two tandem streamers (D) the critical velocity for upstream streamer breakup was 1.45 m/s, where h/L = 1 and (E) the breakup critical velocity for upstream streamer was 1.49 m/s, where h/L = 2.

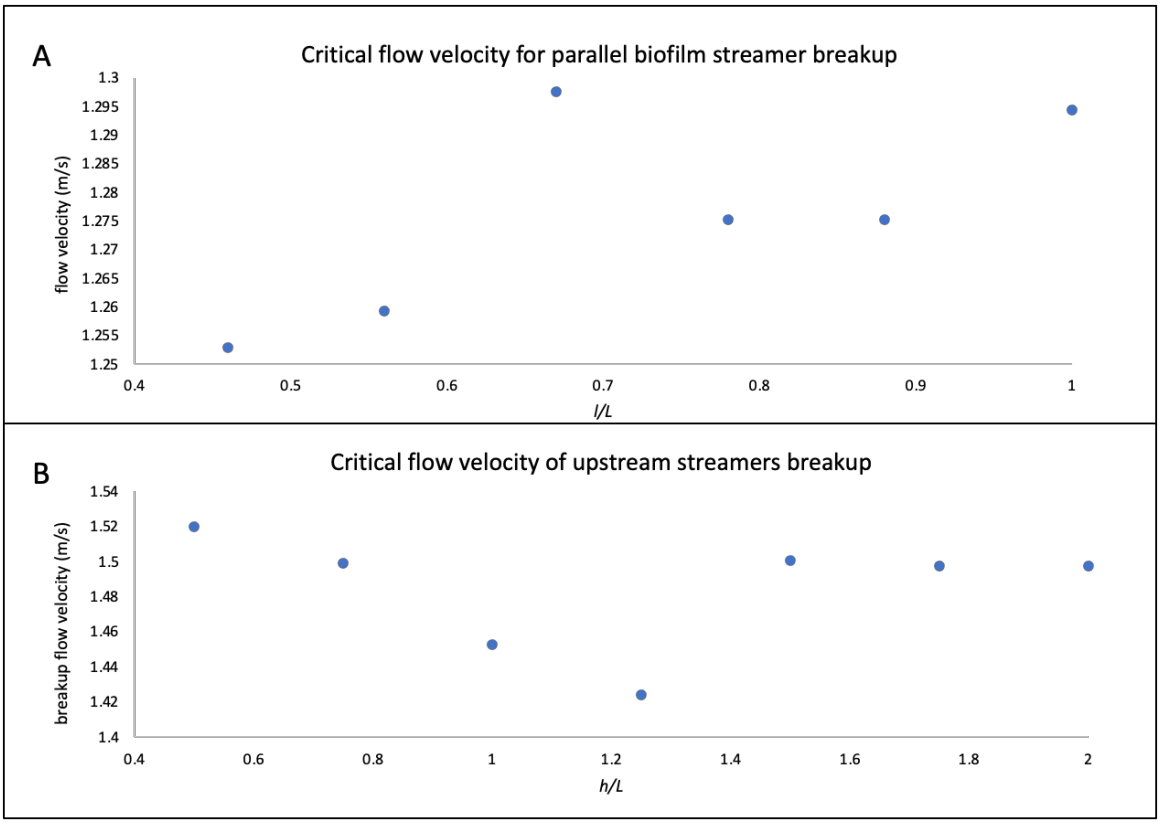

Figure 5.17. Critical fluid velocity for biofilm streamer detachment vs. spacing distance. The critical fluid velocity here is for the first steamer breakup (random in top and bottom streamer) when biofilm streamers in side-by-side arrangement (A). When the streamers in tandem arrangement (B), the critical fluid velocity is for upstream streamer breakup.

5.4.5 Conclusions

In this work, CFD-DEM models have been developed to predict oscillation of biofilm streamers with different configurations in uniform inlet fluid flows. For the single biofilm streamer, the biofilm streamer oscillation predicted by our computational modelling agreed well with the experimental measurements [23]. The simulations have demonstrated that the oscillation frequency of biofilm streamer is affected by the fluid velocity but independent from the length of streamer. The oscillation amplitude of the biofilm streamer is influenced by its length and the flow velocity.

For side-by-side biofilm streamers, in-phase oscillation took place at small gaps ($0.4 < l/L < 0.51$). At intermediate and large spacing distances, streamers flapped on an out-of-phase mode. The oscillation amplitude increased with spacing distance and reached a peak value due to decoupled flapping. However, the maximum amplitude was still smaller compared to single streamer because of strong wake interaction.

For biofilm streamers in tandem, the recirculating zone occurred at small gaps ($h/L < 0.75$). When the fluid velocity was greater than 0.3 m/s, the oscillation amplitudes of the downstream streamer were smaller than that of the upstream streamer. However, an invert drafting effect has been found at lower fluid velocity, in which case the upstream streamer experiences a drag reduction.

With the further increase of fluid velocity, the cohesive failure of biofilm occurred. For the streamers in parallel, the critical velocity slightly increased with the gap distance between two streamers. For streamers in tandem, the upstream streamer always broke first. If the first streamer broke towards the head, the detached streamer segment caused the downstream streamer to break. Otherwise, the detached streamer segment from the upstream streamer had little effect on the downstream streamer.

In future, it will be interesting to gain better understanding of biofilm streamer break-up for streamers with different mechanical properties and arranged in different configurations. It will also be interesting to consider other viscoelastic models to represent different biofilms. If the biofilms may undergo large deformation, we would also need to consider the nonlinear viscoelasticity of biofilms [200, 201].

This model can be potentially up-scaled spatially by choosing appropriate sizes for particles (super-particles) and reasonable number of particles to represent biofilms in more complex environments, such as water filtration with micro-channels. This model could also be useful for the design of feed spacer meshes of membrane systems for water treatment and soil-like porous materials so that biofilm formation can be controlled.

6 Modelling of fluid induced biofilm deformation and detachment by using CFD-DEM approach

6.1 Introduction

Biofilms are formed by microorganisms accumulating at the interfaces and embedding on the extracellular polymeric substance (EPS) which produced by themselves [2]. The EPS majorly consists of polysaccharides [6] and provides many functions to the biofilm, such as adhesion and cohesion which enable biofilms adhere to the surfaces and maintain the mechanical stability of the biofilm system [202]. Biofilms could be found almost anywhere with positive and negative effect on human health and industry. For example, biofilms play an important role in bioremediation since they are able to convert the toxic pollutants to harmless products [6, 203]. Biofilms are also useful in wastewater treatment [204, 205]. However, the accumulation of the biofilms in industrial pipelines and drinking water systems may lead to biocorrosion [59, 206]. The formation of the biofilm allows the pathogenic bacteria to survive in diverse environment [207], thus, the pathogens transmission and biofilm-related infection could occur when the cells detach from biofilm [55]. Thereby, a greater understanding of biofilm detachment in different hydrodynamic conditions may help to control the biofilm-related infection [54].

The fluid shear stress would deform the biofilm, however, the morphology of the biofilm can affect the flow pattern in return. The interaction between the biofilm and the fluid flow is related to the hydrodynamic conditions and mechanical properties of biofilm. However, due to the heterogenous structure of biofilm and the challenge of measurement, the mechanical properties of biofilms are still not well understood [111]. Indentation, rheometer or flow shear tests have been adopted to measure the mechanical properties. Based on the force-displacement curves generated during the indentation tests, the elastic moduli and viscosity could be calculated by fitting the measured data to the empirical contact model [208, 209]. The rheometer with parallel plates have been adopted to measure various biofilms which will enable measurement of linear viscoelastic properties of biofilms [13] or nonlinear viscoelastic properties of biofilms [200]. The mechanical properties of biofilms can also be determined by studying the flow induced biofilm deformation [111]. Several experiments have been conducted by Stoodley et al. to investigate the mechanical properties of biofilm by using the flow cell [15, 16, 54, 210]. The biofilms were grown at the steady state and then exposed to fluctuating shear force. The stress-strain curves were measured by increasing and decreasing the shear stress which was

determined by the fluid velocity. Due to different methods of analysing the mechanical properties of biofilm, the measured elastic modulus and shear modulus can vary a lot, which may be attributed to the heterogenous structure of biofilms.

In principle, EPS provides sufficient mechanical stability for the biofilm system. Thus, the mechanical properties may also depend on the EPS production within the biofilm. The production of EPS is essential during biofilm development since bacteria cells could be immobilized by EPS [2]. The experimental studies reported that the EPS production could be affected by the EPS biosynthetic genes [211, 212]. Besides, mutant strains could cause the overproduction of EPS [213]. Additionally, it was found that when biofilms are subjected to mechanical stresses on an intermediate time scales, the strength of EPS production may increase [105]. However, there is lack of computational modelling to gain better understanding about the contribution of EPS production to biofilm mechanical properties.

Therefore, a three-dimensional individual-based model of biofilm was developed in this study. By coupling the computational fluid dynamics approach with the discrete element method, the model enables us to reveal the fluid induced biofilm deformation and detachment subjected to different flow velocities (or shear rates). Based on the individual-based modelling, the proportion of different microbes could be adjusted by varying the relevant kinetic parameters. Thus, the biofilms with different EPS amount could be obtained to investigate how the EPS production affect the biofilm mechanical properties. In addition, this computational model was also used to conduct loading-recovery test of biofilms. The shear stress and strain can be calculated, which enables us to determine the shear modulus of biofilms. In this study, we model the bacterial mutant that can produce the same type of EPS at different levels.

6.2 Simulation domain

The timescale of the biological processes is much larger compared to that of hydrodynamic process, therefore, flow was applied to a pre-grown biofilm. The pre-grown biofilm was obtained using the individual based model with the same kinetic parameters, as described in chapter 4. Biofilms were grown under in static culture condition (without flow) for 5.3 days. Only heterotrophic bacteria growth, division and EPS production were considered in this study. Then the fluid flow was applied. In this case, the two-way coupling between the solid biofilm and computational fluid dynamic was adopted to investigate the deformation and detachment of biofilm under different hydrodynamic conditions. The simulation domain is displayed in figure 6.1. The pre-grown biofilm was in the left side of the channel, where the heterotrophic

bacterial cells were represented by blue particles while the grey agents were EPS agents, a layer of surface wall was modelled by the red particles to avoid biofilm slide along the bottom wall. The size of the involved particles is in the range of micrometre (1 to 1.3 μm). The fluid flow was applied to the straight channel along the top wall (channel dimensions [L×W×H]: 200×30×50 μm^3). The periodic boundary conditions were applied to the front and back walls to reduce computational effort.

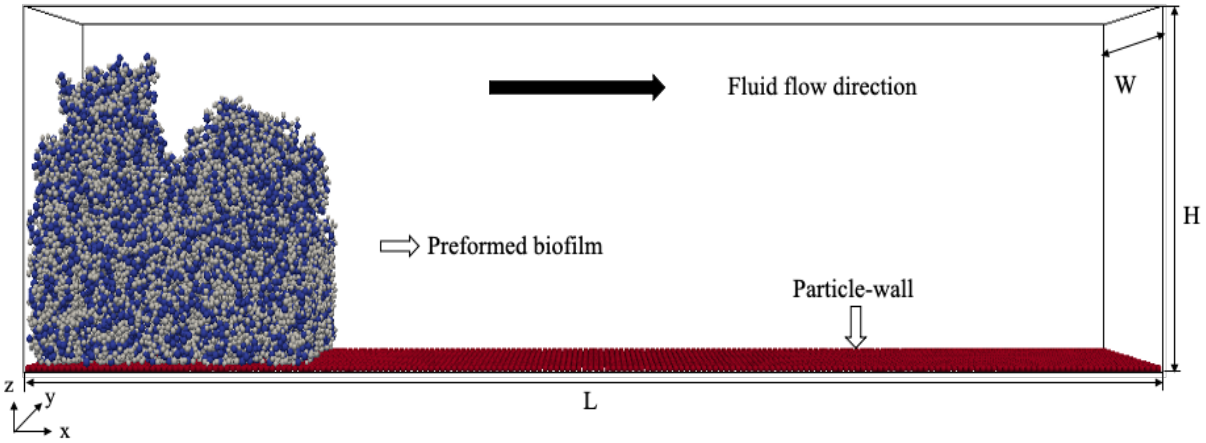

Figure 6.1. Representation of pre-grown biofilm in the channel. EPS formation coefficient is 0.2.

6.2.1 Fluid-induced biofilm detachment

Biofilms with varied EPS amount were considered in the biofilm modeling. The EPS volume ratio in biofilm varies based on bacteria species and growth conditions. A typical EPS volume ratio in drinking water biofilm can vary between 30-86 % [214]. Therefore, the EPS growth yield coefficient was varied from 0.12 to 0.22 (gcod/gcod) which corresponds to EPS/biofilm ratio of 34 % to 68 %. When studying the effect of EPS on biofilm deformation and detachment, the fluid flow with inlet velocity of 0.3 m/s was applied to deform the biofilms for a duration of 40 ms. When investigating the biofilm detachment with the change of flow velocity, we focus on the biofilm with 63 % EPS subjected to inlet flow velocity between 0.1 m/s and 0.4 m/s. The detachment coefficient, which is defined as the ratio of the volume of detached biofilm flocs to the total volume of preformed biofilm, was calculated during initial 14 ms (before biofilm detached from the particle wall). In addition, the erosion of biofilm is defined as the particle number of the detached biofilm floc is less than 1000, while sloughing occurs when the particle number of the detached floc exceeds 1000.

As show in figure 6.2, during biofilm growth, biofilm surface roughness is calculated as the root mean square (RMS) roughness by the following formula [215]:

$$\text{roughness} = \left(\frac{1}{L_x L_y}\iint (h(x,y) - \bar{h})^2 dxdy\right)^{1/2}, \tag{6.1}$$

where $h(x,y)$ is the height of the biofilm in z direction at the location (x,y) on the substratum, $\bar{h}$ is the average height of the biofilm:

$$\bar{h} = \frac{1}{L_x L_y}\iint h(x,y)dxdy, \tag{6.2}$$

The porosity of the preformed biofilm is simply calculated as:

$$porosity = \frac{volume\ of\ voids}{total\ volume} \times 100\% \tag{6.3}$$

where the total volume is computed by multiply the bottom area and the maximum height of biofilm, the voids volume equals to the total volume minus the volume of biofilm. The EPS amount, the mean height and maximum height, the roughness and porosity of different biofilms were shown in table 6.1.

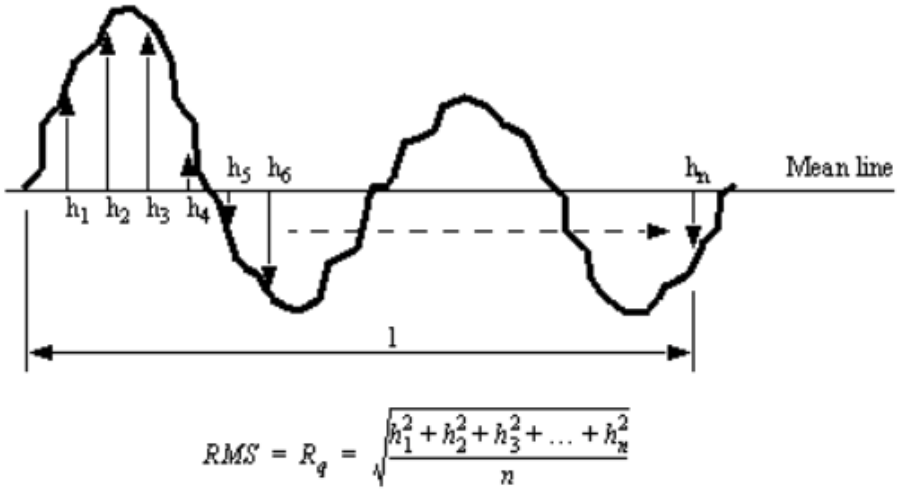

Figure 6.2. Schematic of measuring the root mean square (RMS) roughness of biofilms.

Table 6.1 The dimension of the preformed biofilm. The EPS amount within the biofilm was controlled by the EPS formation coefficient

EPS growth Yield	0.12	0.14	0.16	0.18	0.20
EPS proportion in the biofilm	34 %	49 %	58 %	63 %	68 %
Average height of biofilms (μm)	17.4	19.5	24.6	25	28.5
Maximum height of biofilms (μm)	27.7	33	38.9	36.9	44.4
Biofilm roughness (μm)	4.8	5.8	6.9	5.65	7.49
Porosity of the biofilms (%)	81.2	81.1	81	78.2	79.3

6.2.2 Biofilm deformation-recovery test

The responses of biofilm to a rapid fluctuant shear stress were captured before biofilm failure. The fluid shear stress was applied to the biofilm for 3 ms (loading cycle) and then stopped immediately. Afterwards, the biofilm was allowed to relax for 17 ms (unloading cycle). During the loading period, the fluid shear stress was increased by increasing fluid velocity from 0 m/s at constant acceleration. For the biofilm with 63 % EPS, deformation-recovery tests were carried out by exposing the biofilm to the ramping flow with different accelerations: 20 m/s^2, 30 m/s^2 and 40 m/s^2, respectively. Then the biofilms with 58 % and 68 % EPS were subject to the increasing fluid velocity at the acceleration of 40 m/s^2.

As displayed in figure 6.3, the shear strain in this simple shear test was defined as the angle change between the front edge of biofilm with the left channel wall. The shear modulus could be calculated as follows:

$$G = \frac{\sigma_{xz}}{\alpha} \tag{6.4}$$

where α is the shear strain, σ_{xz} is the fluid induced shear stress on the biofilm which is computed by LAMMPS [216]. In this section, three planes (y = 5 μm, y = 15 μm and y = 25 μm) was selected to measure the deformation angle, as seen in figure 6.4.

In LAMMPS, the tension for each atom is symmetric with 6 components and stored as vector in the following order: $xx, yy, zz, xy, xz\ yz$. For the particle i, the stress tensor could be expressed by (LAMMPS Manual):

$$S_{ab} = -mv_a v_b - W_{ab} \tag{6.5}$$

where a and b take on values x, y, z to generate the components of the tensor, $mv_a v_b$ is the kinetic energy contribution for the atom, W_{ab} is the virial contribution due to intra and intermolecular interactions includes pairwise energy, bond energy, angle, dihedral, improper interactions and KSpace contribution from long-range Coulombic interactions [217]. The stress matrix could be determined by dividing the global tensor matrix by the total volume of the biofilm. The details of the stress calculation are illustrated in the LAMMPS manual (https://lammps.sandia.gov/doc/compute_stress_atom.html).

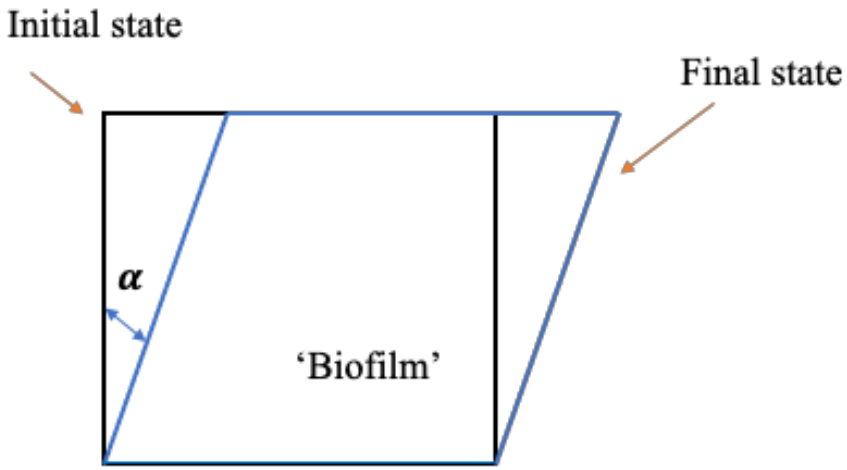

Figure 6.3. Schematic diagram illustrating biofilm deformation and the deformation strain.

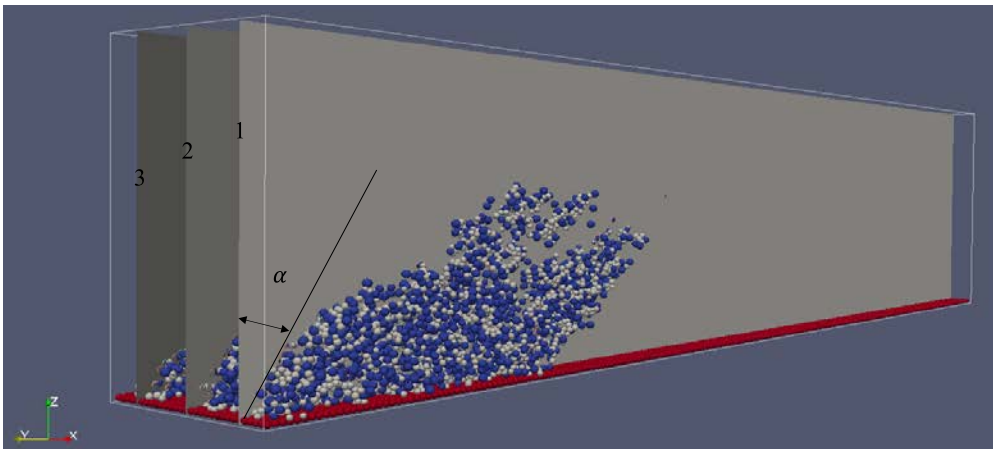

Figure 6.4. The measurements of shear deformation angle.

6.3 Methodology and parameters

During biofilm deformation and detachment, the translational motion of each DEM agent is calculated based on Newton's second law (equation (3.20)), the contact force is calculated by using equation (3.18). The fluid flow is solved by locally-averaged incompressible Navier-Stokes equation (equation (3.22a) and (3.22b), only viscous stress was computed since the Reynolds number is small here (3.75 to 15). The Reynolds number is calculated by equation (4.3) where the average flow velocity was defined as 2/3 of the maximum flow velocity ($u_{avg} = \frac{2}{3} u_{max}$) [58]. Both drag force (equation (3.24)) and lift force (equation (3.29)) were considered in fluid-particle interaction. The cohesive force among the particles were computed by using equation (3.21). In this study, different cohesive strength was applied to determine the cohesive force between different functional agents. Therefore, five different values of cohesive strength were used for the interactions of bacterial cells with bacterial cells, bacteria cells with EPS particles, bacteria cells with particle-wall, EPS particles with the particle-wall, EPS particles with EPS particles. Since EPS plays a significant role on binding the bacterial cells, the cohesive strength driven by EPS was assumed to be three orders of magnitude larger than it governed by HET bacteria. The simulation parameters are listed in table 6.2.

Table 6.2 Input parameters for biofilm deformation and detachment.

Numerical simulation parameters	
Density of particles	10^3 kg m^{-3}
Normal and tangential elastic constants	10^3 kg m^{-1} s^{-2}
Fluid dynamic viscosity	1×10^{-3} kg m^{-1} s^{-1}
Fluid density	10^3 kg m^{-3}
Normal damping constants	10^{13} m^{-1} s^{-1}
Tangential damping constants	10 m^{-1} s^{-1}
Parameters for cohesive model	
Particle interaction	Cohesive strength
HET bacteria-EPS	1.6×10^{-18} J
HET bacteria - particle wall	2.3×10^{-21} J [218]
EPS - particle wall	2.3×10^{-18} J

EPS - EPS	5×10^{-18} J [219]
HET bacteria - HET bacteria	1.6×10^{-21} J [220]

6.4 Results and discussion

6.4.1 Flow effect on biofilm deformation and detachment

Figure 6.5 shows the deformation and detachment of biofilm contains 63 % EPS subjected to inlet flow velocity of 0.1 m/s. Because of the gradient flow shear force along y direction and the patchy structure of biofilm, the top of the biofilm deforms much more than the bottom of the biofilm. The biofilm elongated along with the flow direction and detachment occurs in the rear part (figure 6.5A). Since the small inlet velocity was applied, biofilm deformation is dominant during biofilm exposed to the fluid shear force and only erosion occurs. It is found that the largest detached biofilm floc consists of 831 particles with volume of 4.55E-16 m^3. Figure 6.5B displays the remaining biofilm at the end of 40 ms fluid shear. There was no further erosion or detachment observed.

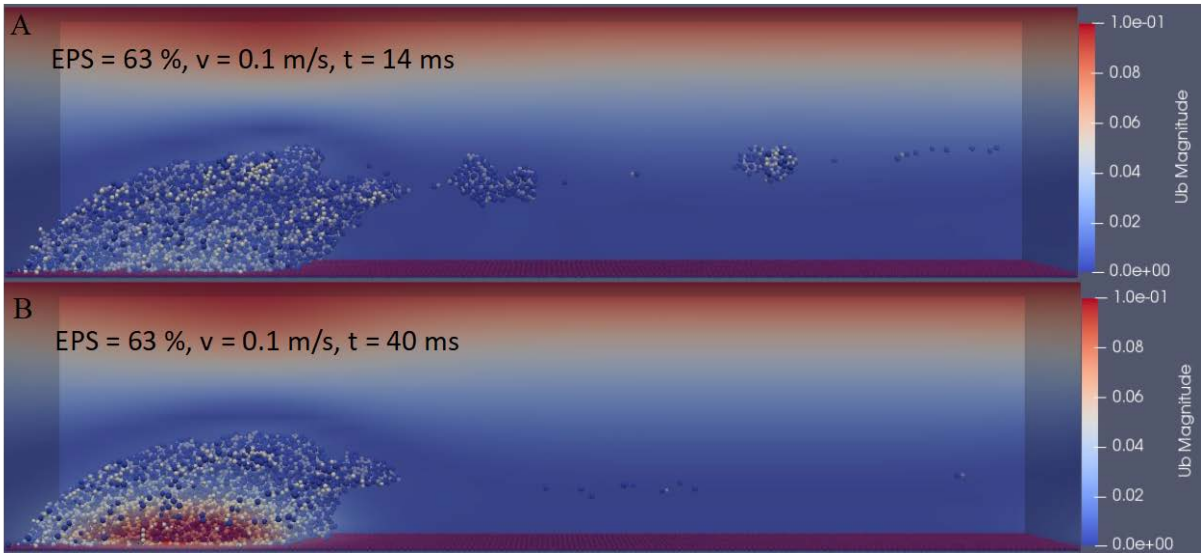

Figure 6.5. Biofilm deformation and detachment at inlet flow velocity of 0.1 m/s. (A) t = 14 ms and (B) t = 40 ms.

When the inlet flow velocity increase to 0.2 m/s, detachment at the rear part of the biofilm occurred as early as 3 ms (figure 6.6A). Compare to lower inlet fluid velocity (i.e. 0.1 m/s), detachment frequency sharply increased and biofilm sloughing also occurred as seen in figure 6.6B. The largest detached floc contained 2194 particles with the volume of 1.19E-15 m^3. The continuous detachment events led to a decrease in the volume of the remaining biofilm.

Comparing figure 6.5 and 6.6, it is clear that higher flow velocity led to more biofilm detachment at the same time period. However, there was still some biofilm remaining on the surface at the time of 40 ms (figure 6.6C).

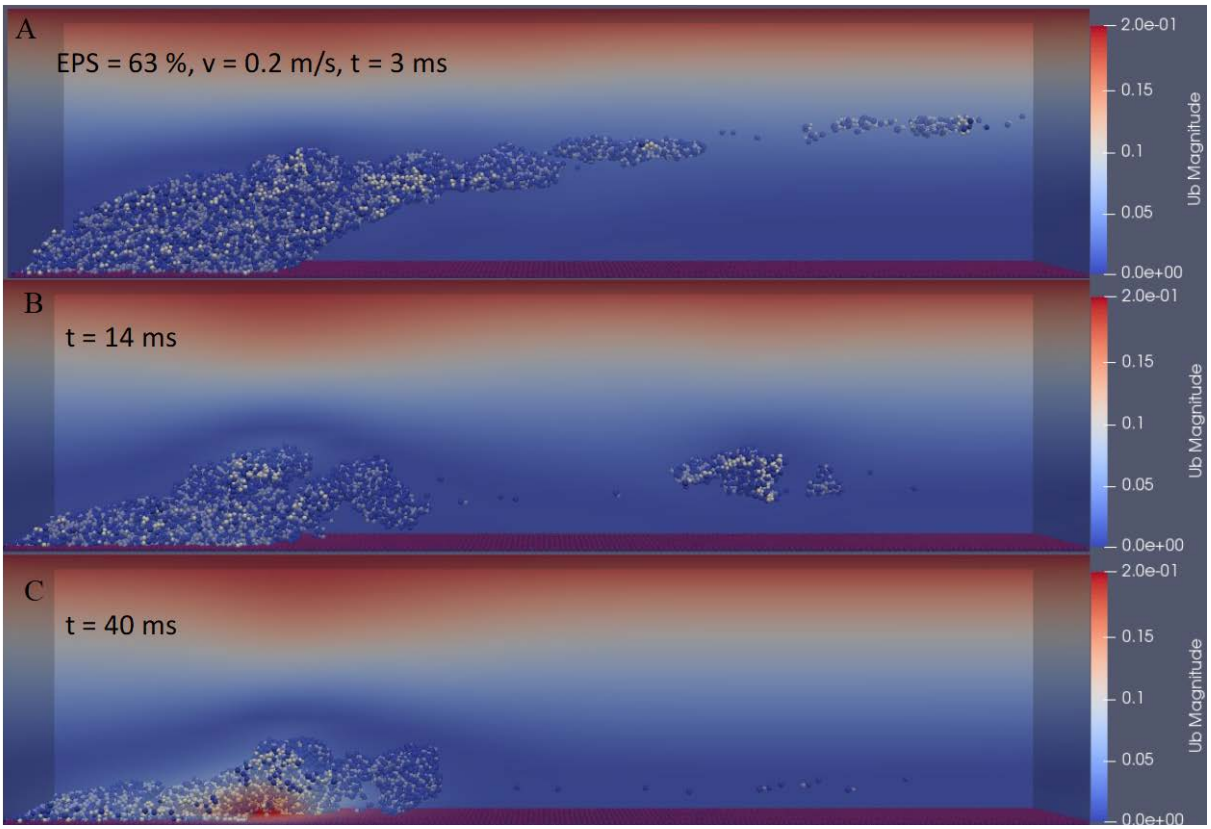

Figure 6.6. Biofilm deformation and detachment at inlet flow velocity of 0.2 m/s, t =3 ms, 14 ms and 40 ms.

High-frequency biofilm detachment could also be captured when further increasing the inlet flow velocity to 0.3 m/s. It was found that biofilm sloughing became the predominant behaviour during the detachment process. In this case, the largest detached floc contained 4434 particles with the volume of 2.38E-15 m^3. As shown in figure 6.7A, there still has a small fraction of biofilm remained and adhered to the surface due to the cohesive force at time of 14 ms. The rest of biofilm continuously exposed to the fluid shear force and more biofilm flocs detached from the parent biofilm at 25 ms (figure 6.7B). Interestingly, it was found that the remaining biofilm layer (marked in figure 6.7B) started rolling along the particle wall under the steady fluid shear force (figure 6.7C, D and E). This phenomenon was firstly observed by Rupp et al. [15], the *S.aureus* microcolonies moved downstream by rolling in a flow cell. Biofilm removal occurred by the rolling motion and finally moved out of the original location at around 40 ms (figure 6.7F).

The inlet velocity of fluid flow is finally increased to 0.4 m/s, various-sized biofilm flocs detached rapidly due to the high fluid shear force. Figure 6.8A displays the morphology of the biofilm after being subjected to the shear force for 14 ms. From which, it can be seen that only a layer of biofilm left on the surface. Furthermore, the rolling motion was also captured in this case. The biofilm rolled along the surface for several microseconds then lift from the surface by the fluid (figure 6.8B-F). Finally, the biofilm was washed away with the fluid flow at around 36 ms (figure 6.8G).

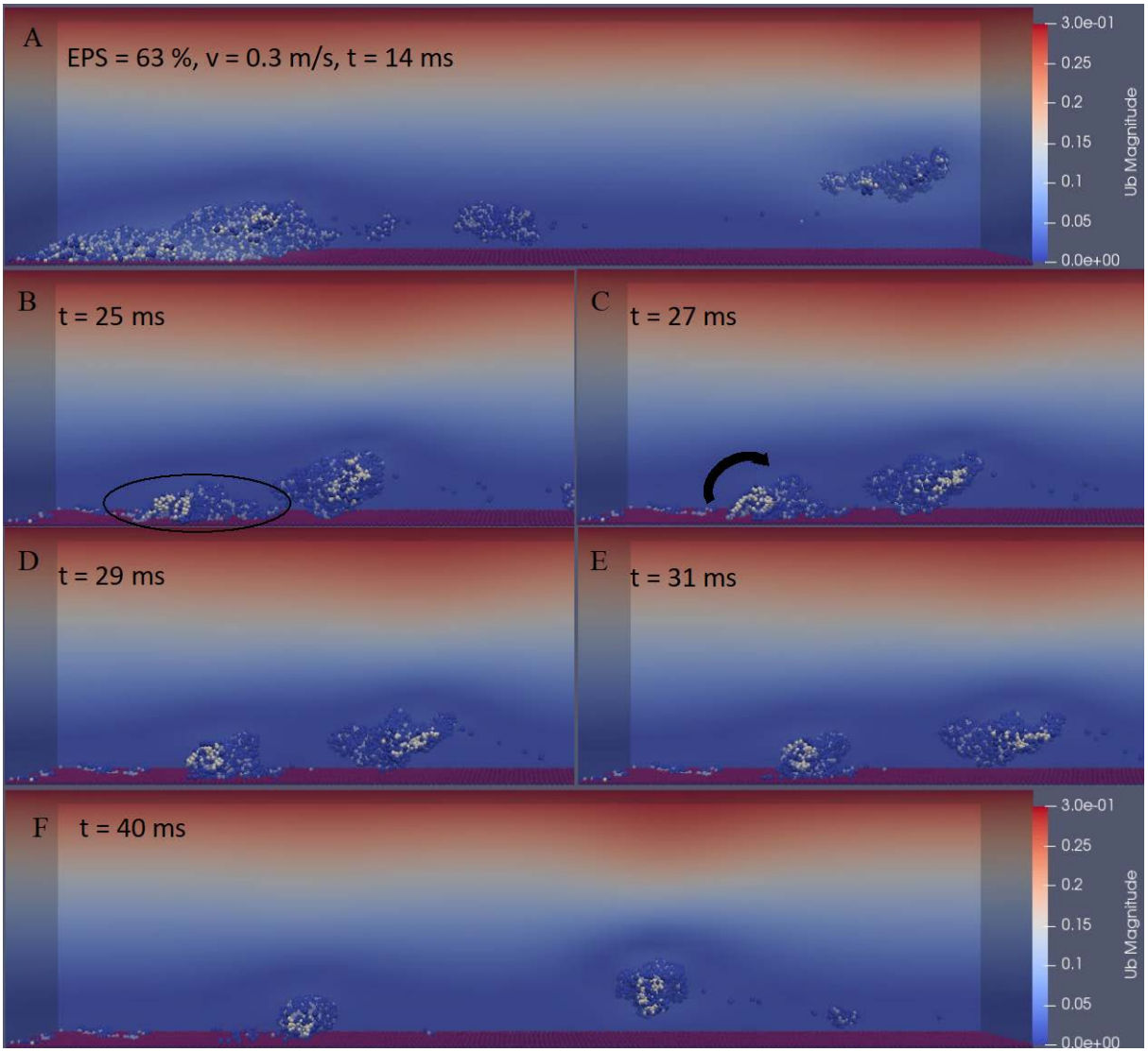

Figure 6.7. Biofilm (63 % EPS) deformation and detachment at inlet flow velocity of 0.3 m/s. (A) Biofilm deformation and detachment at time of 14 ms. (B) - (E) the rolling motion of biofilm observed in simulation. (F) Biofilm deformation and detachment at time of 40 ms.

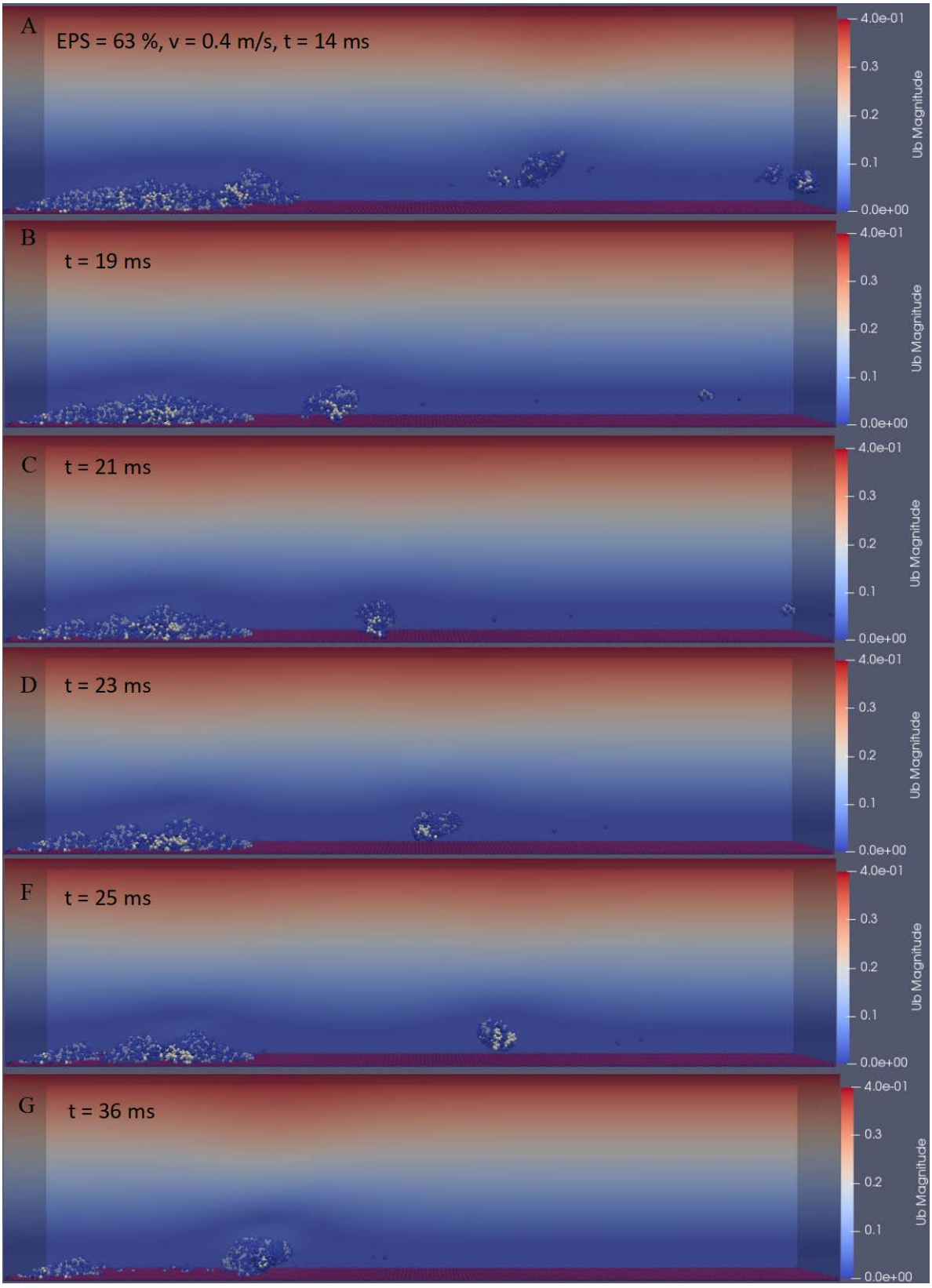

Figure 6.8. (A) Biofilm deformation and detachment at inlet flow velocity of 0.4 m/s, 14 ms. (B)-(E) the rolling motion of biofilm observed in simulation. (F) Biofilm removal at inlet flow velocity of 0.4 m/s.

6.4.2 EPS effect on biofilm deformation and detachment

To study how the EPS amount affect the deformation and detachment of biofilm, we apply the inlet fluid velocity of 0.3 m/s for a duration of 40 ms. When the biofilm contains a small amount of EPS (34 % EPS), it was found the biofilm flocs could easily detach from the parent biofilm at a high frequency. In addition, it can be seen that lots of the heterotrophic particles separated from the biofilm and exposed to the fluid individually (figure 6.9). This phenomenon should be caused by the low EPS production in the biofilm since one of the functions of the extracellular polymeric substances is to immobilize the cells in biofilm [2]. Therefore, the low EPS amount in the biofilm may not be able to hold biofilm cells in close proximity. Another reason is the cohesive force among the particles within the biofilm is positively related to the EPS amount. The small number of EPS makes biofilm less strong and susceptible to flow induced erosion and detachment.

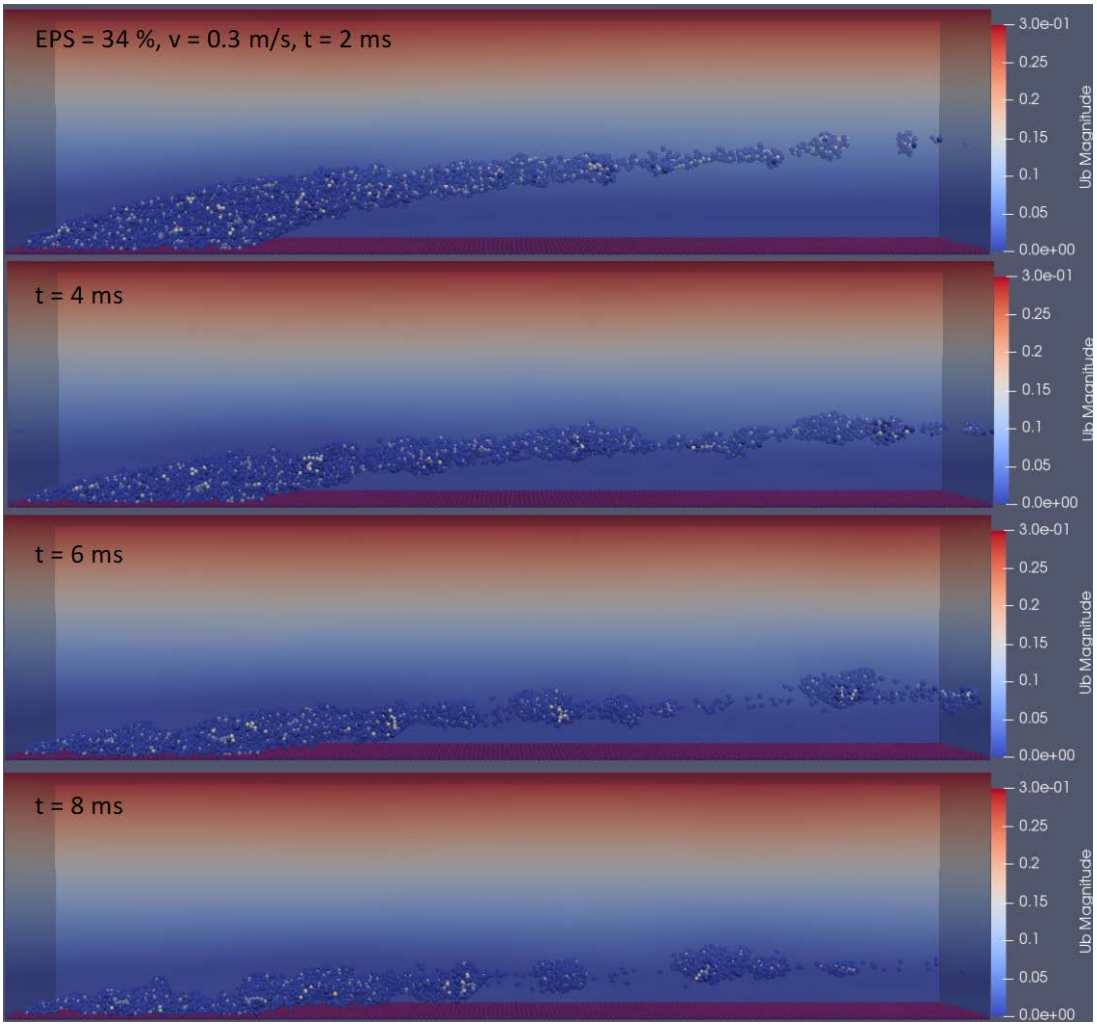

Figure 6.9. The deformation and detachment of biofilm with EPS amount of 34 % during initial 8 ms, the inlet fluid velocity here is 0.3 m/s.

When EPS amount increased, the detachment frequency of biofilm decreased. Figure 6.10 shows the biofilms after being subjected to the fluid flow for 14 ms. It can be seen that the volume of detached biofilm decreased as the EPS amount increased. At the end of 40 ms (figure 6.11), it was found that for the biofilms with low EPS amount (34 %, 49 % and 58 % EPS), most particles were detached at the end of the simulation but still have a thin layer biofilm adhered to the particles wall. However, when the EPS amount increased to 63 %, the biofilm was finally removed by the rolling motion. It was suggested that the rolling motion may depend on the amount of EPS. When the EPS amount further increased to 68 %, about half of the initial biofilm remained on the surface at the end of simulation. It was further demonstrated that the biofilm appeared to be stiffer due to high EPS production.

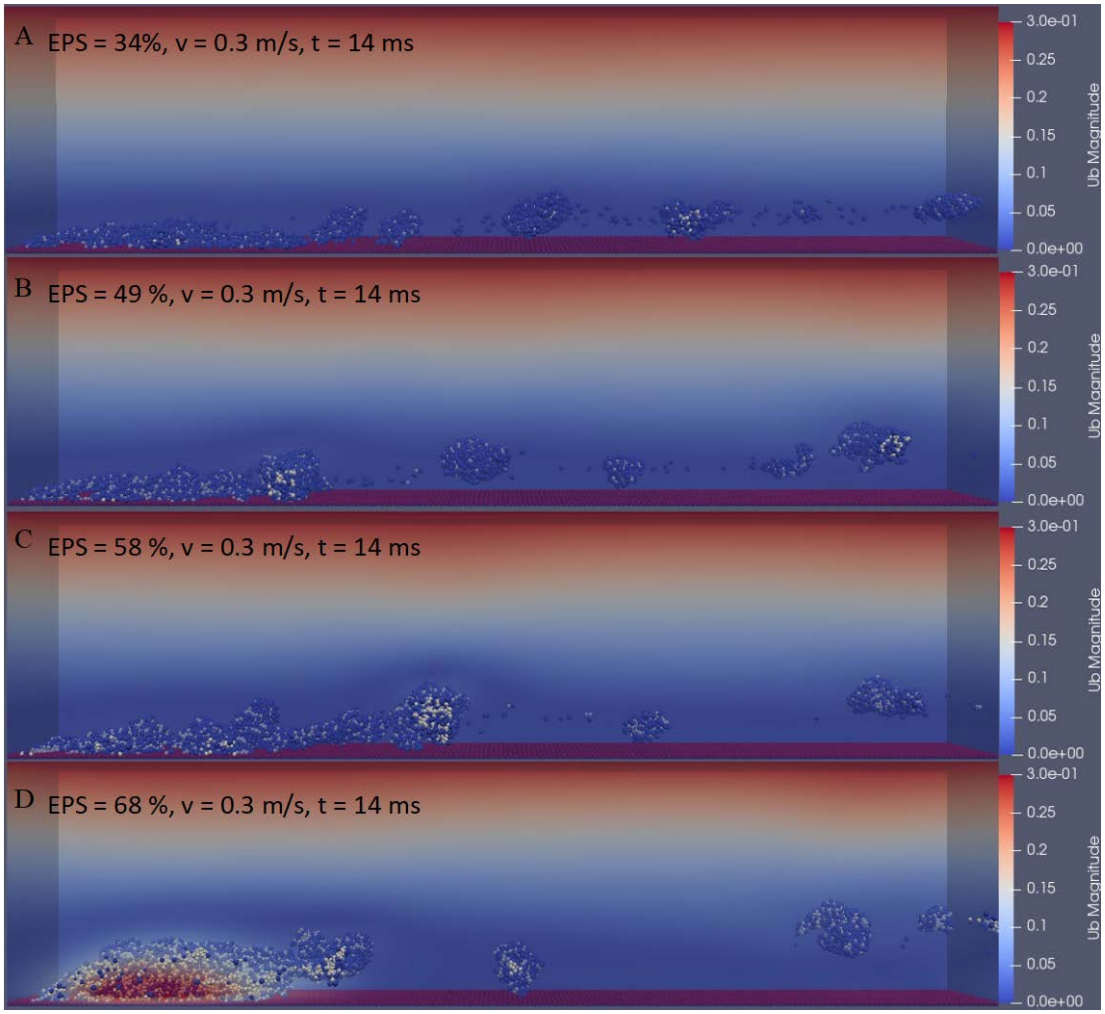

Figure 6.10. Biofilm deformation and detachment at time of 14 ms with the inlet fluid velocity of 0.3 m/s. The amount of EPS within the biofilm increased from (A) 34 %, (B) 49 %, (C) 58 % to (D) 68 %. For the biofilm with 63 % EPS amount, the deformation and detachment results of biofilm in the same hydrodynamic condition was shown in figure 6.7A.

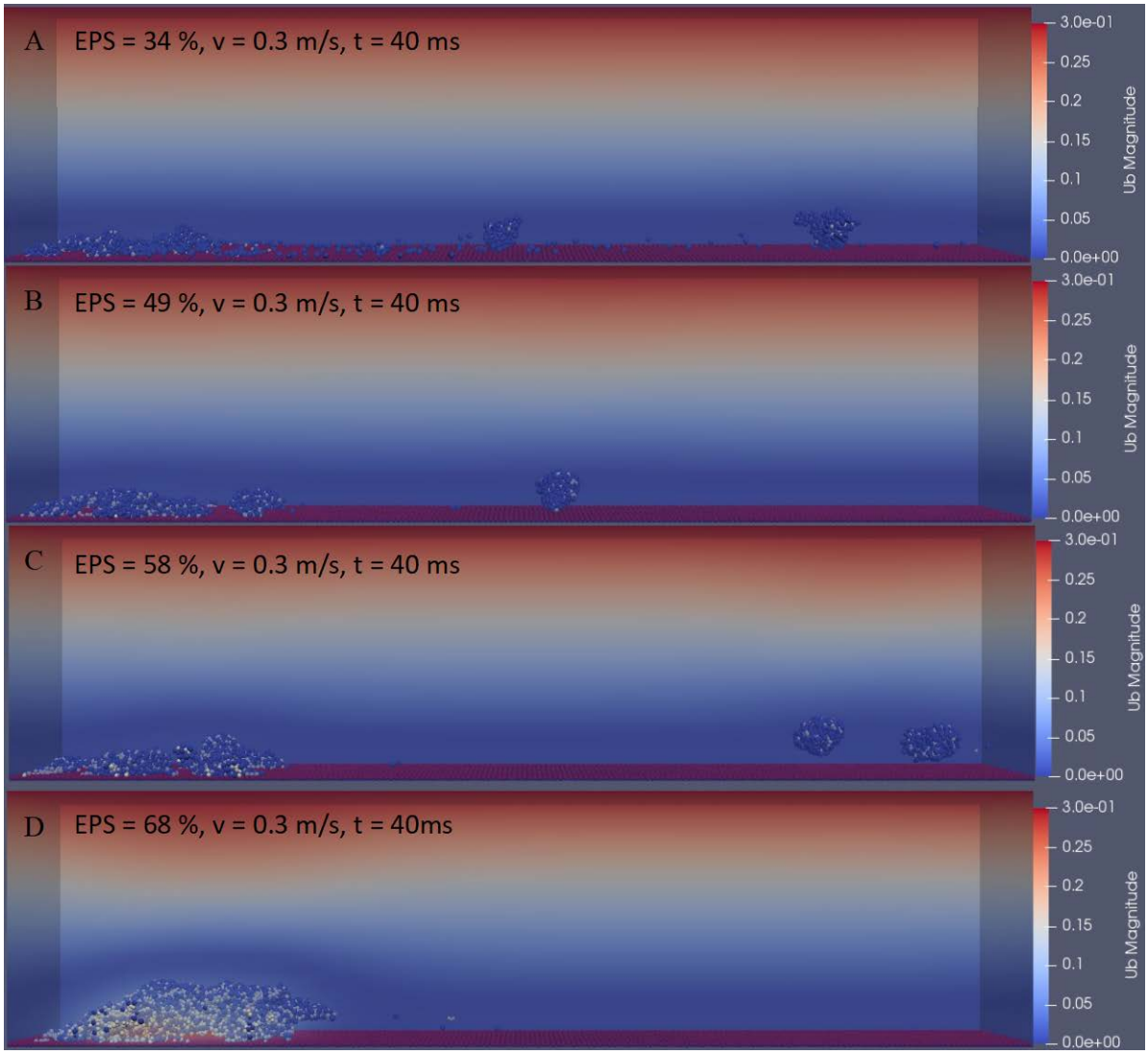

Figure 6.11. Biofilm deformation and detachment at time of 40 ms with the inlet fluid velocity of 0.3 m/s. The amount of EPS within the biofilm increased from (A) 34 %, (B) 49 %, (C) 58 % to (D) 68 %. For the biofilm with 63 % EPS amount, the deformation and detachment results of biofilm in the same hydrodynamic condition was shown in figure 6.7F.

The detachment rate coefficient, which is defined as the ratio of the volume of detached biofilm flocs to the total volume of preformed biofilm in 14 ms, was adopted to describe the biofilms detachment behaviour under the hydrodynamic conditions. As displayed in figure 6.12, the detachment rate coefficient increased with the inlet fluid velocity which agrees with the experimental observation [54]. There is no significant detachment until inlet flow velocity increased to 0.2 m/s, the coefficient increased sharply before the inlet flow velocity reached 0.3 m/s and then slowed down when the inlet fluid velocity was further increased. In addition, as expected, the detachment rate coefficient decreased with the increase in EPS amount when the

inlet fluid velocity was kept as constants (figure 6.13). The detachment rate coefficient for the biofilm with 34 % EPS was approximately twice that for the biofilm with 68 % EPS. It was suggested that the resistance of the biofilm to the external fluid is largely attributed to the EPS amount. EPS are responsible for the mechanical stability of the biofilm due to their cohesive prosperities, therefore, the biofilms with more EPS agents are more stable when exposed to the fluid flow.

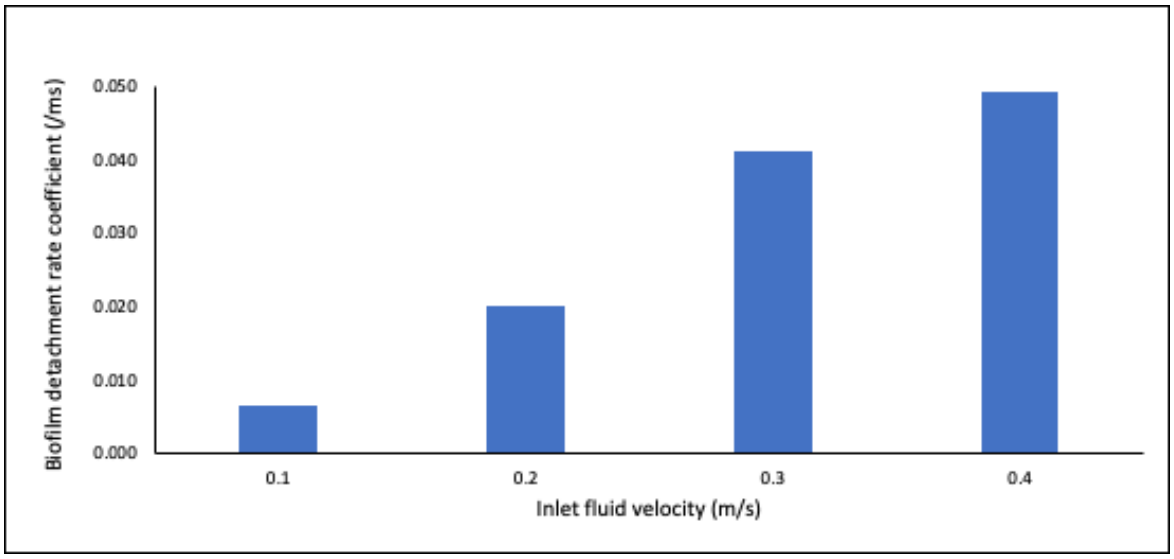

Figure 6.12. (A) Detachment rate coefficient increased with the elevated inlet fluid velocity. Biofilm with 63 % EPS has been considered.

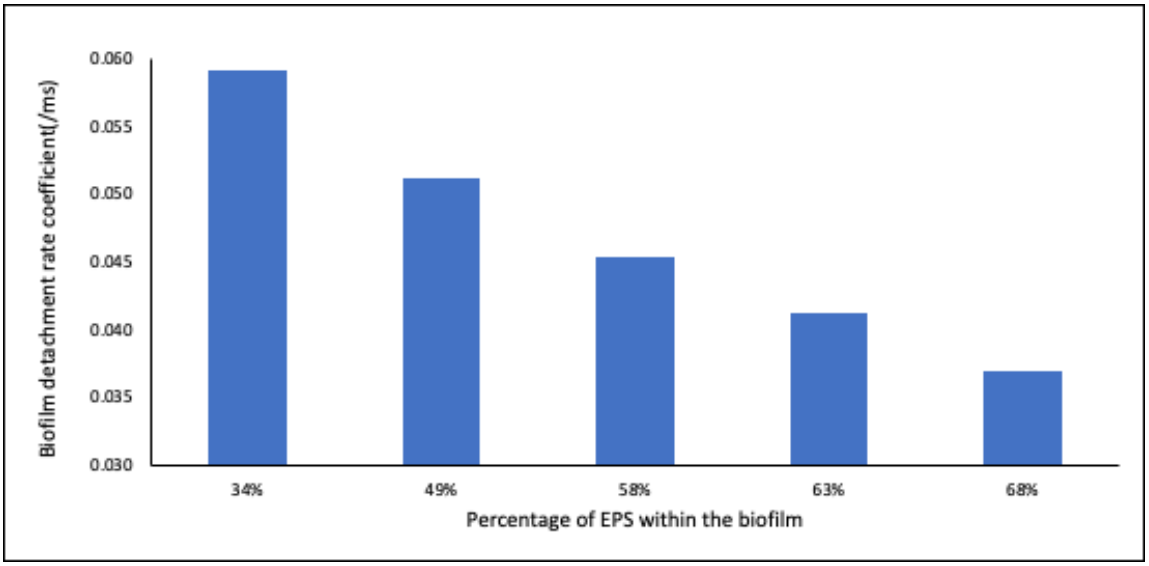

Figure 6.13. Detachment rate coefficient decreased with the increase in EPS amount when the inlet fluid velocity is kept at 0.3 m/s.

6.4.3 Biofilm viscoelastic responses during deformation-recovery test

Deformation of the biofilm was monitored for 3 ms as the fluid velocity was incrementally increased from 0 m/s. Then the fluid flow was suddenly stopped, the biofilm was allowed to relax for 17 ms. The stress-strain curve was obtained from the loading and unloading cycle. Figure 6.14 shows the deformation and recovery properties of the biofilm (63 % EPS). In this case, the fluid velocity was elevated at the acceleration of 20 m/s^2 and reached the maximum value (0.06 m/s) at 3 ms. The maximal deformation angle, which was approximately 23 degree (0.41 in radians), was captured at the same time (figure 6.14B). After the fluid flow was stopped, biofilm started recovery. As seen in figure 6.14C, the biofilm did not return to the original shape at time of 20 ms, about 6 times of the duration of flow induced biofilm deformation. Such a residual deformation is due to the viscous nature [221]. This is not surprising as the interactions between the biofilm particles were modelled as spring-dashpot based viscoelastic models.

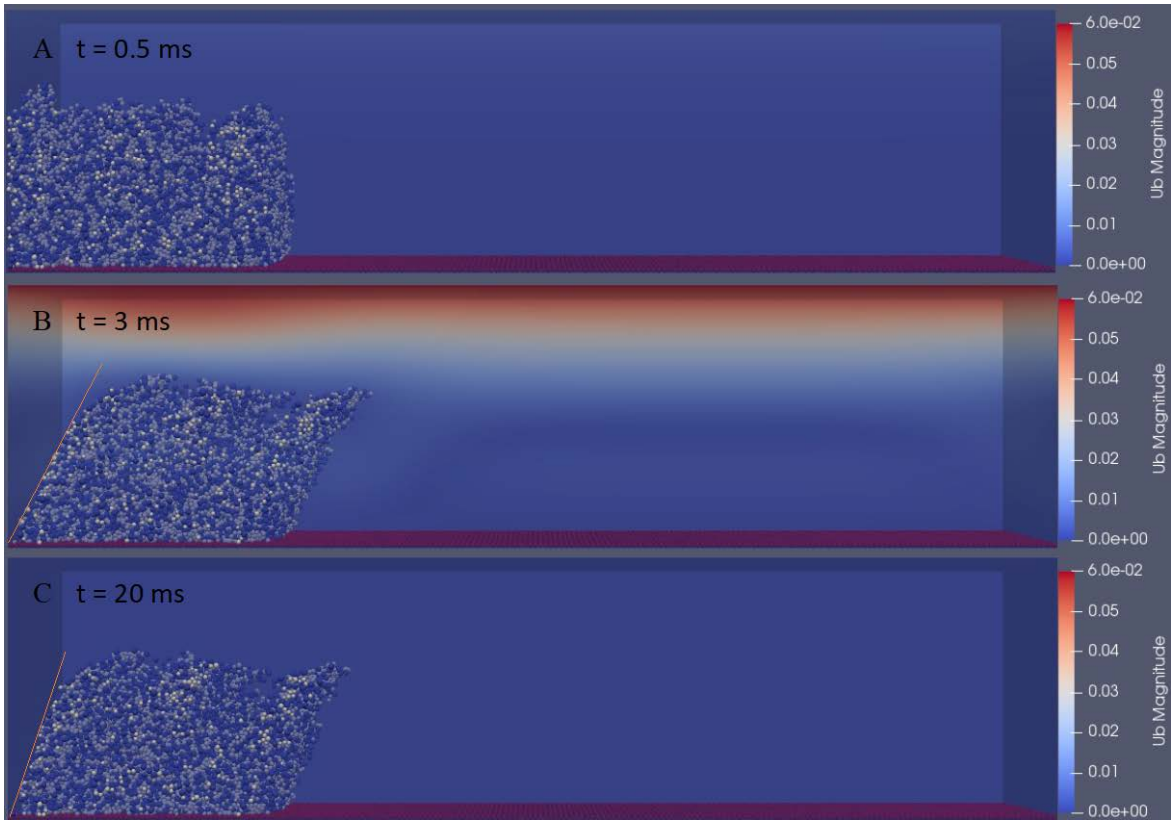

Figure 6.14. Biofilm (with 63 % EPS) deformation in a loading-recovery test. The biofilm was subjected to the fluid for 3 ms, and the relaxation of biofilm was monitored by stop the fluid for 17 ms. The fluid velocity was increased at the acceleration of 20 m/s^2. (A) shows the biofilm structure at time of 0.5 ms. (B) shows the maximum deformation angle which was capture at time of 3 ms. (C) shows the recovery of biofilm when the fluid was stop for 17 ms and the biofilm did not return to its original shapes.

To understand the viscoelastic deformation of biofilms at different loading rates and different levels of stress, additional simulations were performed using the acceleration of fluid velocity of 30 m/s^2 and 40 m/s^2. Correspondingly, the maximum fluid velocity was 0.09 m/s and 0.12 m/s, respectively.

Figure 6.15A shows the fluid-induced stress σ_{xz} changes overtime, the stresses were calculated every 0.2 ms. It can be clearly seen that the stress σ_{xz} increased significantly when the biofilm was subjected to the fluctuate fluid flow. The applied fluid velocity, fluid induced shear stress on biofilm and deformation angle (shear strain) reached the peak value at 3 ms. In addition, the higher loading rate results in the higher maximal stress. When the applied fluid flow velocity increased slowly over time (acceleration of fluid flow velocity was 20 m/s^2), the maximum fluid induced shear stress is 3.16 Pa. This peak value increased to 4.26 Pa and 5.39 Pa when further increasing the acceleration to 30 m/s^2 and 40 m/s^2. The corresponding maximum deformation angle was 28° (0.49 in radians) and 33° (0.57 in radians)

As displayed in figure 6.15B, the strain was measured during biofilm deformation and recovery. The deformation angle increases sharply when the biofilm exposed to the fluid flow. After the fluid flow was removed, the biofilm recovery was monitored for 17 ms wherein no fluid shear force was applied. The fluid induced stress decreased rapidly during 3 ms and 4 ms (figure 6.15A), some of the deformation (12 %-16 %) was recovered in this short-term. This immediate recovery was caused by the elastic contraction. Afterwards, stress reduced slightly and showed a plateau at the end of the test. Further contraction of biofilm could be observed over the remaining 16 ms. However, it can be seen that a significant residual deformation remained finally, and the residual strain increase with the maximum fluid velocity. It is because that the higher fluid velocity results in the higher fluid induced shear stress and strain during biofilm deformation. Upon stress removal, an instantaneous elastic strain could be recovered due to the time-independent elastic response. However, the viscoelastic recovery proceed slowly since the viscoelasticity is a time-dependent behaviour of the materials [222]. Therefore, the biofilm with larger deformation needs more time to get recovered.

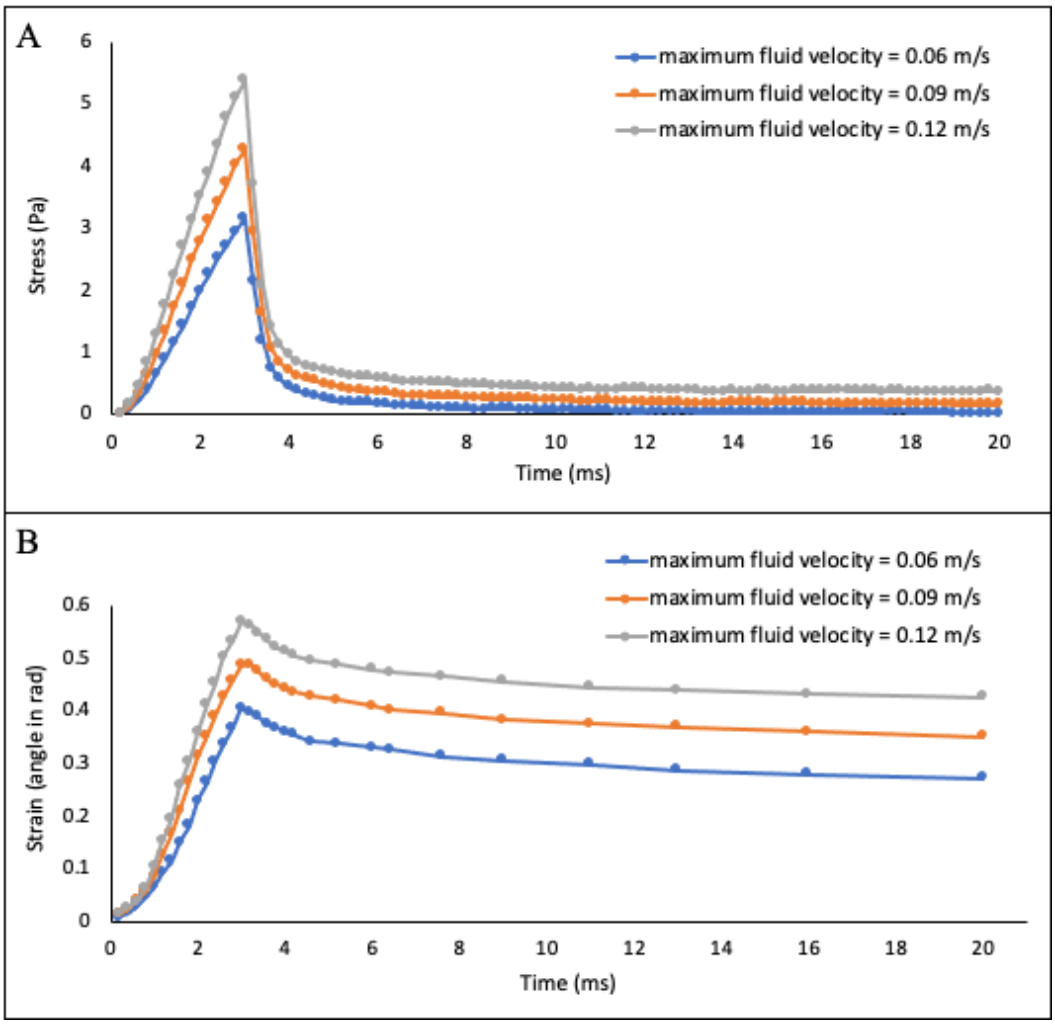

Figure 6.15. (A) Fluid induced shear stress on biofilm changes overtime, the fluid was applied for 3 ms and followed by a relaxation of 17 ms. Three tests were carried out for biofilm with 63 % EPS. In each test, the accelerations of increasing the fluid velocity are 20 m/s^2, 30 m/s^2 and 40 m/s^2, respectively. (B) Measurements of strain during the deformation and recovery.

Figure 6.16 shows the fluid induced stress-strain correlation during biofilm deformation and recovery within 20 ms. When the biofilm exposed to the small fluid shear force, almost all the fluid induced stress could be relived after the fluid flow was stopped (blue curve in figure 6.16). The hysteresis loop in the curve represented the dissipation of energy during the biofilm deformation process. The "J" shaped stress-strain curve has further documented that the biofilm is viscoelastic material. When the applied fluid shear force increased, the stress relaxation and biofilm recovery could be captured as well, however, a residual stress remained at the end of the test which indicates that the time for biofilm relaxation may not enough. The area of hysteresis loop increased with the maximum fluid velocity, it is suggested that the biofilm exposed to higher external force may lose more energy during deformation. The tangent shear

modulus, which is the slope of any two adjacent data point on stress-strain curve, were calculated at small deformation (strain < 0.1). The results were summarized in table 6.3. The initial modulus (e.g. data point 1-2) was often correlated to the shear modulus within the linear region. It can be seen that lower acceleration rate leads to smaller initial modulus, which is due to the viscous effect of biofilms. In general, the results demonstrated this biofilm showed some strain stiffening effect follow by strain softening effect, which is possibly due to the change in the microstructure within the biofilm.

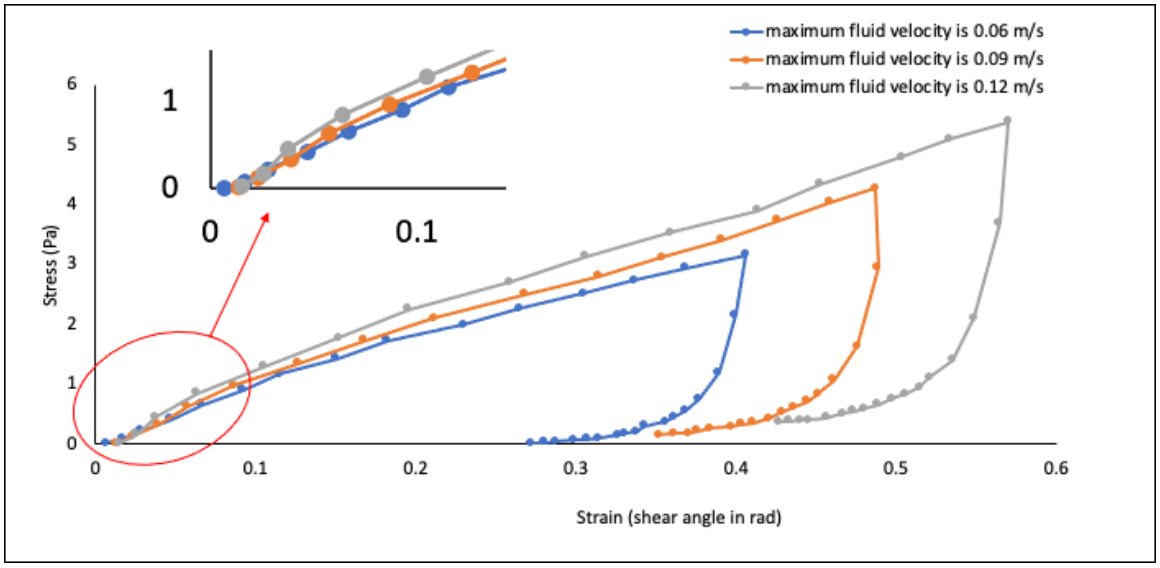

Figure 6.16. The stress-strain curve during biofilm (with 63 % EPS) deformation and relaxation. The applied fluid shear force was increased by elevating the maximal fluid flow velocity.

Table 6.3 Tangent shear modulus for biofilm with 63 % EPS when the strain is less than 0.1.

Shear modulus at small deformation (Pa)			
	acceleration = 20 m/s^2	acceleration = 30 m/s^2	acceleration = 40 m/s^2
Data point 1-2	7.0	11.3	14.0
Data point 2-3	12.4	13.1	24.3
Data point 3-4	10.5	16.3	15.1
Data point 4-5	12.1	11.7	--
Data point 5-6	9.79	--	--

The biofilms with varied EPS amount were subjected to the increased fluid shear force by increasing the fluid velocity at a constant acceleration of 40 m/s^2. The previous results of biofilm detachment showed that the biofilm with less EPS could easily detached when applied

an external fluid shear force. Therefore, the biofilms which contain higher EPS amount (58 %, 63 % and 68 % EPS) were considered in this section. The height, roughness and porosity of these biofilms were shown in table 6.1. Since the fluid flow was applied along the top wall in the simulation domain, the velocity varied with the height of simulation box (figure A1 in Appendix). Therefore, it is important to note that although the inlet fluid condition was set as the same, the biofilms would be subjected to different fluid shear force if their height varied.

Figure 6.17 shows the fluid induced stress and strain changes overtime. Similar to the previous results, the stress rose rapidly, and a significant deformation could be observed during the loading period. In addition, it could be found that for the biofilms which contains 58 % and 63 % EPS, the maximum fluid induced stresses during deformation equal to 5.52 and 5.39 Pa since they have the similar height (38.9 and 36.9 μm). However, the maximal strain of the biofilm with 58 % EPS was greater than it of biofilm with 63 % EPS (figure 6.17). It was suggested that the high EPS production results in the better resistance to the external fluid shear force.

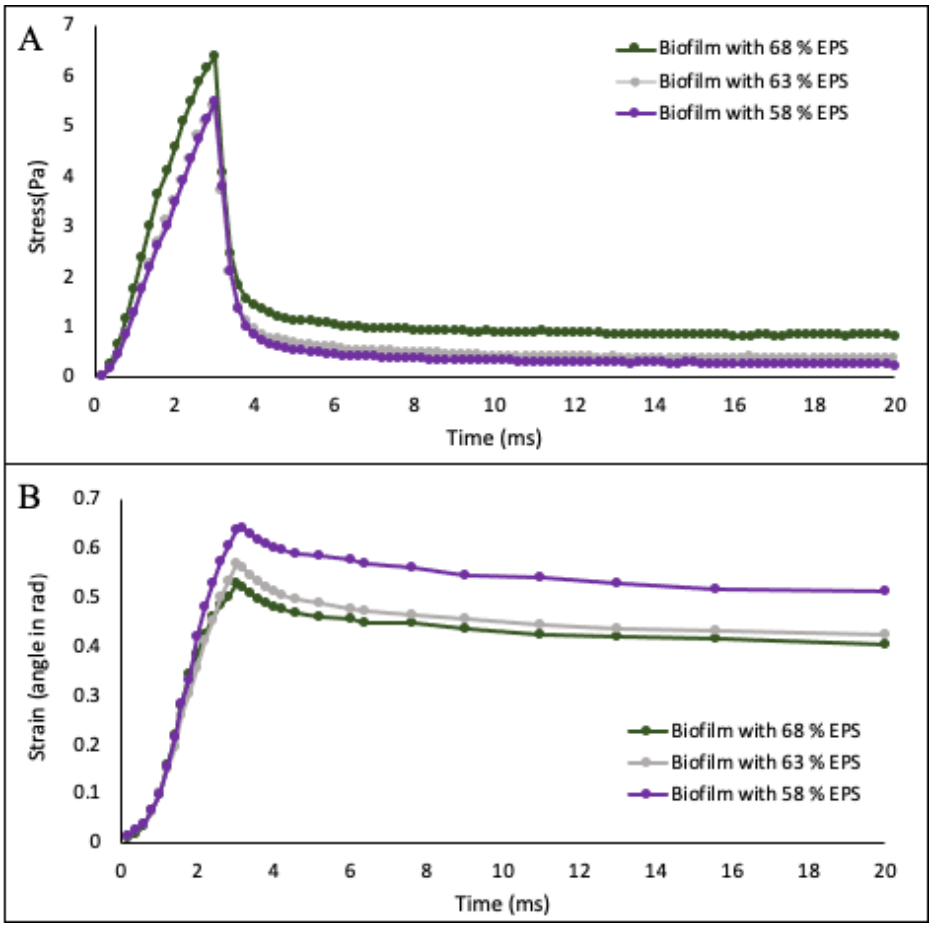

Figure 6.17. (A) Plot the fluid induced stress during biofilm deformation and recovery. The biofilms with 58 %, 63 % and 68 % EPS were selected. The fluid velocity was elevated at a constant acceleration of 40 m/s^2 during deformation. (B) Plot the strain changes during biofilm deformation and recovery.

The maximum height of the preformed biofilm increased to 44.4 μm when the proportion of EPS in the biofilm reached 68 %. Thereby, the top portions of the biofilm experienced a higher shear force and showed a greater deformation. Correspondingly, a higher fluid induced shear stress on biofilm was captured at 3 ms, equals to 6.41 Pa (figure 6.17A). However, the strain curve in figure 6.17B illustrates that the large stress did not lead to a large shear angle of deformation. By contrast, the biofilm with 68 % EPS has the minimal strain during deformation. It indicates that the biofilm with high EPS production might be hard to deform when exposed to the external fluid shear force. Those results demonstrated that the EPS matrix plays an important role in protecting biofilms from the external stress [17].

For all the biofilms, a significant recovery could be observed over a short time after the fluid was stopped, the further contraction occurred slowly over the remaining time. The fluid induced stress declined and biofilm retracted with time due to the cell rearrangement in the deformed biofilm [223], it was demonstrated that the process of rearrangement of EPS is faster than the rearrangement of bacteria [224]. In the present modelling work, 19 % deformation was recovered during the total relaxation period when the number of EPS accounted for 58 % in the biofilm. Meanwhile, it was found that 25 % deformation was recovered when the biofilm contained more EPS components (63 %). Since those two biofilms experienced similar fluid shear force. Therefore, the simulation results suggest that the biofilms recovery could be facilitated by the EPS.

The stress-strain curves of different biofilms during deformation and recovery are shown in figure 6.18. It can be seen that the deformed biofilms did not achieve steady-state relaxation in the present study since the time scale here is in milliseconds. As a result, a small residual stress remained at the end of the simulation. In the loading period, the fluid induced stress appears to be linearly proportional to the strain. The tangent shear modulus for different biofilm has been calculated when the strain is less than 0.1. The results in table 6.4 indicate the shear modulus in small deformation increased with the EPS amount. It can be seen that lower EPS ratio leads to a smaller initial modulus. In general, all these biofilms exhibit some strain stiffening effect followed by strain softening, which is also due to the change in the microstructure of biofilms during the deformation.

The shear compliance, which is the reciprocal of the shear modulus, could be used to describe the strain induced by unit shear stress. Therefore, the biofilms with more EPS amount have a smaller deformation when exposed to the same external shear force.

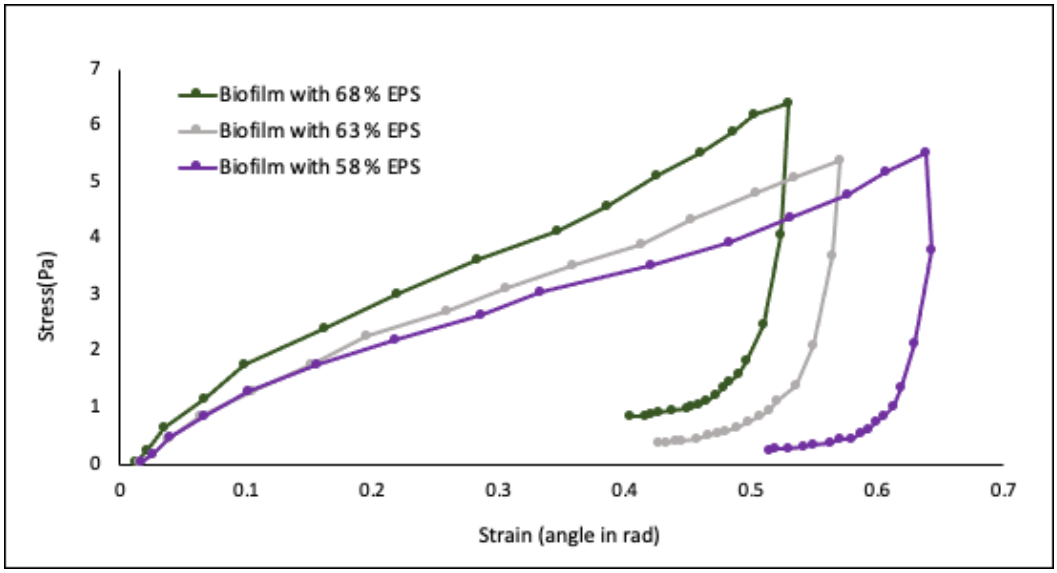

Figure 6.18. Stress-strain curves of biofilms (58 % EPS, 63 % EPS and 68 % EPS) during deformation and relaxation. The fluid velocity was increased from 0 m/s at a constant acceleration of 40 m/s^2.

Table 6.4 Tangent shear modulus for different biofilm when the strain is less than 0.1.

Shear modulus at small deformation (Pa)			
	Biofilm with 58 %	Biofilm with 63 %	Biofilm with 68 % EPS
Data point 1-2	16.6	14.0	24.6
Data point 2-3	20	24.3	29.4
Data point 3-4	14.5	15.1	16.3
Data point 4-5	--	--	19.0

6.5 Conclusions

The CFD-DEM approach has been adopted to investigate the biofilm deformation and detachment under hydrodynamic condition. It was demonstrated that the model allows the prediction of biofilm detachment at various hydrodynamic conditions. When the biofilm (63 % EPS) was exposed to a steady fluid shear force (inlet fluid velocity was kept as constant), the detachment rate coefficient increased with inlet fluid velocity (i.e. shear stress). When the inlet flow velocity is less than 0.1 m/s, biofilm deformed along the fluid direction and only erosion occurs. Biofilm sloughing occurred when the inlet flow velocity increased to 0.2 m/s. Further increasing the inlet fluid velocity to 0.3 and 0.4 m/s, the detachment events was dominated by sloughing and the biofilm could be removed for the surface by the rolling motion.

For biofilms with different EPS amount, the inlet fluid velocity was kept at 0.3 m/s during the detachment. The detachment rate coefficient decreased with the amount of EPS within the biofilm. For the biofilm with a low EPS production (34 % and 49 % EPS), the biofilm flocs could easily detach when exposed to the fluid shear force. In addition, the dispersion of individual cell could be observed during detachment process. The frequency of the detachment events decreased with the increased EPS amount. Finally, the biofilm could not be removed when the EPS amount increased to 68 %.

In addition, the loading-recovery tests were carried out by using the 3D model to investigate the mechanical properties of biofilm. The results demonstrated that before biofilm failure occurred, for the biofilm which experienced a greater fluid shear force, more energy was dissipated during deformation. The results also suggested that the resistance of biofilm to external force is related to the EPS amount in the biofilm. In the present modelling, the bacteria mutant that produces more EPS appears to be stiffer.

7 Conclusion and Future work

7.1 Conclusions

In this PhD project, biofilm deformation and detachment have been modelled using individual based model where a simple drag model was adopted, which was followed by two way coupled CFD-DEM model. Both models could reasonably predict biofilm deformation and detachment in different fluid conditions.

For the biofilm exposed to a very small shear flow (Reynold number was less than 0.0015), biofilm detachment can occur after several days. The detachment of large segments of biofilms seemed to be caused by shear failure. Biofilm shape varied with EPS production within the biofilm. Biofilms with different EPS amount were subjected to the shear flow to study how EPS affect biofilm detachment. However, there was no well-defined relationship between EPS amount and biofilm detachment rate coefficient. In this case, the detachment behaviour was mainly affected by the biofilm morphology and EPS distribution rather than the EPS amount within the biofilm although the EPS adhesion force is proportional to the EPS mass. For the biofilms pre-grown with a given EPS formation coefficient, it was found that the detachment rate coefficient increased with shear rate in this case. In addition, for biofilms grown at shear flow condition became easier to detach when the shear rate increased to 0.2-0.4 s^{-1}.

This work has been extended by using CFD-DEM approach. In the two-way coupled model, the detachment rate coefficient increased with the inlet fluid velocity when biofilm was subject to fluid flow, which was similar with the results of individual based modelling. In addition, it was found that the biofilm with less EPS could be easier to detach when exposed to the fluid flow. The detachment rate coefficient decreased with the EPS amount in the biofilm. Those results demonstrated that EPS could provide a sufficient mechanical stability of biofilm system, especially in the hydrodynamic environment.

The biofilm streamer oscillation and their cohesive failure have been predicted by using CFD-DEM approach. Those simulations have demonstrated that the streamer oscillation was caused by the vortex shedding which could be generated when flow pass the upstream biofilm cluster. Fluid velocity could affect the oscillation frequency and amplitude of streamer. The oscillation amplitude could also be affected by the streamer length. For parallel biofilm streamers, the oscillation amplitude increased with the spacing distance between them, finally reached a peak value due to the decoupled oscillation. For biofilm streamers in tandem, the oscillation

amplitudes of the upstream streamer were larger than that of the downstream streamer when flow velocity was great than 0.3 m/s. An invert drafting effect was found when the fluid velocity was 0.2 m/s. The cohesive failure of biofilm streamer occurred when exposed to an elevated fluid velocity. For side-by-side biofilm, the critical velocity increased with the spacing distance. When biofilm steamers in tandem arrangement, the upstream streamer always break first. If it broke towards head, the detached segment would lead to the breakup of downstream streamer.

Finally, the deformation-recovery tests were carried out to investigate the mechanical properties of biofilm. It was found that the biofilm experienced a higher shear force would dissipate more energy during deformation. The high EPS production within the biofilm would help biofilm resistant to the external shear force.

7.2 Future work

7.2.1 Further improvement in biofilm model

In chapter one, biofilm deformation and detachment have been studies by using individual based modelling (NUFEB). It was found that the biofilm slide along the bottom wall during deformation and detachment in all cases. In this model, the normal adhesion model was adopted between biofilm and the bottom wall, in which the first layer of biofilm did not detach from surface but slide along the wall proportional to the tangential force of flow. Therefore, the sliding fraction, which also termed Coulomb damping, could be adopted into this model in future [225]:

$$F_S = \mu_S F_{an} \tag{7.1}$$

F_{an} is the normal adhesive force and μ_S is the coefficient of siling fraction coefficient which depends on the surface roughness. It was found that the biofilm initial attachment and adhesion force could be increased by increasing the surface roughness [226]. Therefore, the implement of sliding fraction can potentially enable us to predict how surface roughness affect initial biofilm attachment and how the flow can flush away the biofilms.

7.2.2 Biofilm streamer formation in porous media

The simulations in this research work have demonstrated that the two-way coupled CFD-DEM approach have the capacity to study the biofilm-fluid interaction. The oscillation of biofilm streamers and their cohesive failure have been investigated in chapter 5. However, the streamer formation has not been simulated. A lot of experimental work has demonstrated that the biofilm

streamers are ubiquitous and could easily form in porous media, such as curved microfluid channel, water filter and medical stents [22, 60, 227]. The formation of biofilm streamer will lead to some industrial problems, such as the clogging of filtration system and the increased pressure drop in the feed channel of membrane. Therefore, it is of particular significant to model the biofilm streamer formation and deformation in porous media to gain deeper insight into streamer formation. By using the CFD-DEM model, as show in figure 7.1, the porous media could be designed as water filtration which is similar to the experiment work in [21]. The width of the channel is 10 μm (figure 7.1A). The filamentous biofilm formed downstream (Figure 7.1B and C). In future, three case studies could be considered:

1. When the channel width was kept at 10 μm, biofilm streamer formation in different hydrodynamic fluid conditions could be studied by changing the inlet flow velocity.
2. The channel width then could be varied from 5 μm to 20 μm to study the effect of channel dimension on biofilm streamer formation, in this case, the inlet fluid velocity has to be constants.
3. Investigate the effect of EPS amount on biofilm streamer formation in porous media since EPS is the major component in the streamers. Similar to the previous work, EPS production could be varied by changing the EPS formation coefficient during biofilm growth.

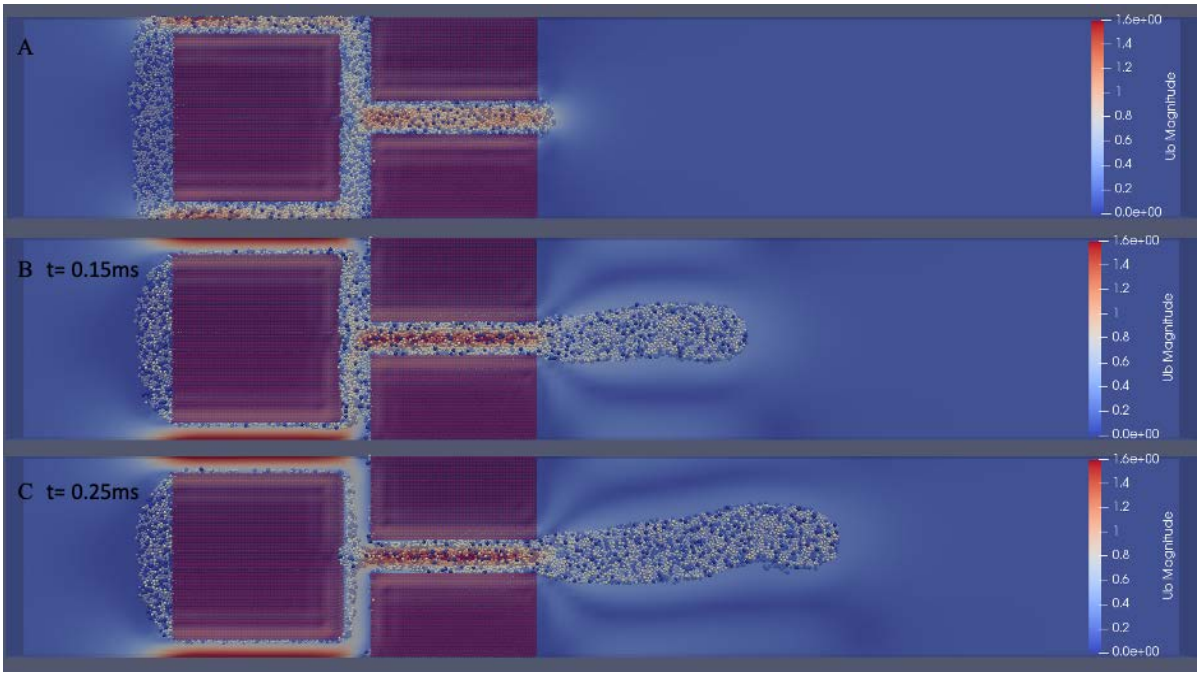

Figure 7.1. Biofilm streamer formation in porous media. The width of the microchannel is 10 μm, inlet fluid velocity is 0.1 m/s.

7.2.3 Scale up strategy for the modelling

In this research work, biofilm/flow interactions have been studied by using individual based model and tow-way coupled CFD-DEM model at microscale (50-100 μm). It is not feasible to using IbM approach to simulate the large-scale microbial system, such as those in wastewater treatment plants or in the marine environment [104]. A method which could be adopted to overcome this limitation is to use super-individuals (super particles) which has been demonstrated by Cristian et al. [19]. In that model, particles with diameter of 10-20 μm have been applied to represent a cluster of similar cells rather than a single particle whose diameter was around 1 μm. Therefore, our model could be scaled-up in the same manner. Additionally, the timestep in the simulation could also be reduced by using super-individuals since the maximum stable timestep (critical timestep) in DEM is $\sqrt{\frac{m}{k}}$, where m is the minimum particle mass and k is the stiffness among the particles [228, 229]. In chapter 6, biofilm deformation and detachment were simulated by exposing biofilm to a hydrodynamic. In this case, the particles within the biofilm were around 1 μm, the timestep in DEM is 1e-8 s, each simulation need to be run for 4-5 days which is computationally expensive. Therefore, super-individual based model could be used in future to simulate large-scale microbial community and reduce the computational effort.

8 Appendix

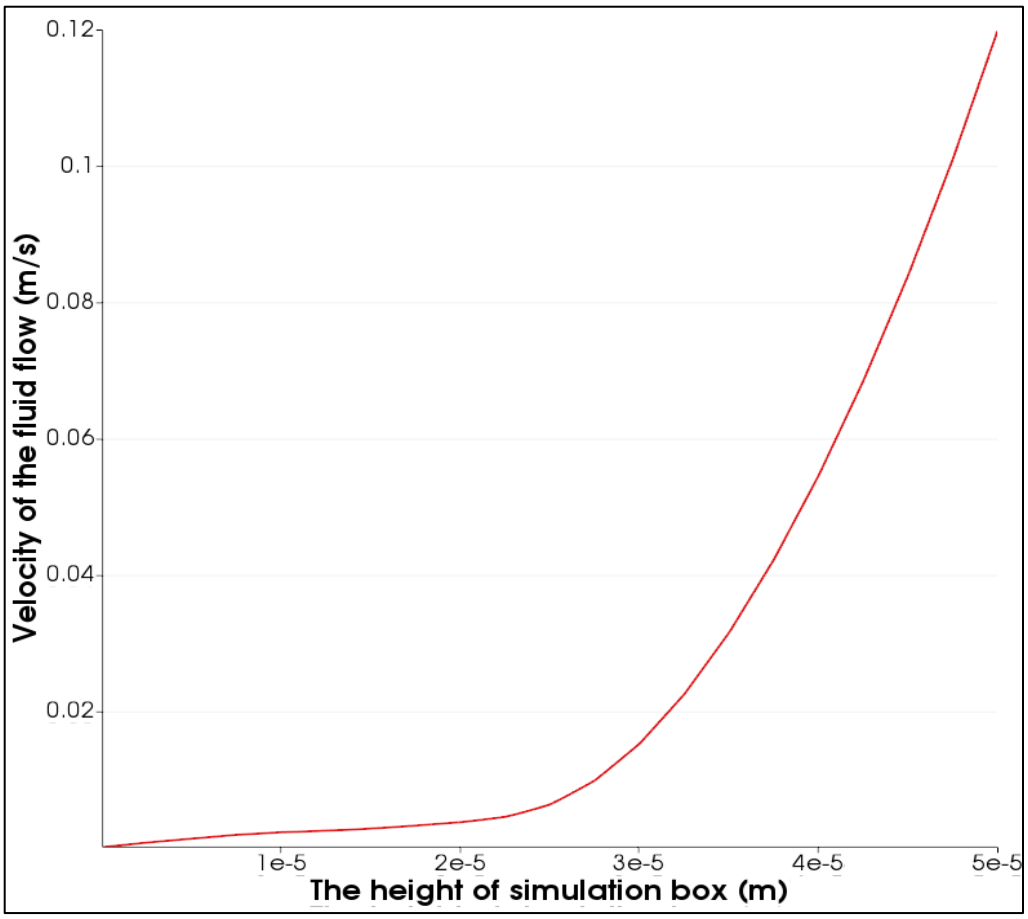

Figure A1. Inlet fluid velocity varied with the height of simulation box since the fluid flow was applied along the top wall, Therefore, the biofilms with different height would be subjected to different fluid shear force.

9 References

1. Schachter, B., *Slimy business—the biotechnology of biofilms.* Nature biotechnology, 2003. **21**(4): p. 361-365.
2. Flemming, H.-C. and J. Wingender, *The biofilm matrix.* Nature reviews microbiology, 2010. **8**(9): p. 623-633.
3. Flemming, H.-C., et al., *Biofilms: an emergent form of bacterial life.* Nature Reviews Microbiology, 2016. **14**(9): p. 563.
4. Mah, T.-F., *Biofilm-specific antibiotic resistance.* Future microbiology, 2012. **7**(9): p. 1061-1072.
5. Azizi, S., I. Kamika, and M. Tekere, *Evaluation of heavy metal removal from wastewater in a modified packed bed biofilm reactor.* PloS one, 2016. **11**(5): p. e0155462.
6. Yadav, S.K. and S. Sanyal, *Biofilms: The Good and the Bad*, in *Biofilms in Human Diseases: Treatment and Control*. 2019, Springer. p. 13-26.
7. Das, S. and H.R. Dash, *Microbial bioremediation: A potential tool for restoration of contaminated areas*, in *Microbial biodegradation and bioremediation*. 2014, Elsevier. p. 1-21.
8. Davies, D., *Understanding biofilm resistance to antibacterial agents.* Nature reviews Drug discovery, 2003. **2**(2): p. 114-122.
9. Sousa, C., M. Henriques, and R. Oliveira, *Mini-review: antimicrobial central venous catheters–recent advances and strategies.* Biofouling, 2011. **27**(6): p. 609-620.
10. Kostakioti, M., M. Hadjifrangiskou, and S.J. Hultgren, *Bacterial biofilms: development, dispersal, and therapeutic strategies in the dawn of the postantibiotic era.* Cold Spring Harbor perspectives in medicine, 2013. **3**(4): p. a010306.
11. Galie, S., et al., *Biofilms in the food industry: health aspects and control methods.* Frontiers in microbiology, 2018. **9**: p. 898.
12. Van Houdt, R. and C. Michiels, *Biofilm formation and the food industry, a focus on the bacterial outer surface.* Journal of applied microbiology, 2010. **109**(4): p. 1117-1131.
13. Towler, B.W., et al., *Viscoelastic properties of a mixed culture biofilm from rheometer creep analysis.* Biofouling, 2003. **19**(5): p. 279-285.
14. Körstgens, V., et al., *Uniaxial compression measurement device for investigation of the mechanical stability of biofilms.* Journal of microbiological methods, 2001. **46**(1): p. 9-17.
15. Rupp, C.J., C.A. Fux, and P. Stoodley, *Viscoelasticity of Staphylococcus aureus biofilms in response to fluid shear allows resistance to detachment and facilitates rolling migration.* Applied and environmental microbiology, 2005. **71**(4): p. 2175-2178.
16. Stoodley, P., et al., *Structural deformation of bacterial biofilms caused by short‐term fluctuations in fluid shear: An in situ investigation of biofilm rheology.* Biotechnology and bioengineering, 1999. **65**(1): p. 83-92.
17. Gloag, E.S., et al., *Biofilm mechanics: implications in infection and survival.* Biofilm, 2020. **2**: p. 100017.
18. Kreft, J.-U., et al., *Individual-based modelling of biofilms.* Microbiology, 2001. **147**(11): p. 2897-2912.
19. Picioreanu, C., J.-U. Kreft, and M.C. Van Loosdrecht, *Particle-based multidimensional multispecies biofilm model.* Applied and environmental microbiology, 2004. **70**(5): p. 3024-3040.
20. Kreft, J.-U. and J. Wimpenny, *Effect of EPS on biofilm structure and function as revealed by an individual-based model of biofilm growth.* Water Science and Technology, 2001. **43**(6): p. 135-135.
21. Marty, A., et al., *Formation of bacterial streamers during filtration in microfluidic systems.* Biofouling, 2012. **28**(6): p. 551-562.
22. Das, S. and A. Kumar, *Formation and post-formation dynamics of bacterial biofilm streamers as highly viscous liquid jets.* Scientific reports, 2014. **4**: p. 7126.

23. Stoodley, P., et al., *Oscillation characteristics of biofilm streamers in turbulent flowing water as related to drag and pressure drop.* Biotechnology and bioengineering, 1998. **57**(5): p. 536-544.
24. Rusconi, R., et al., *Laminar flow around corners triggers the formation of biofilm streamers.* Journal of The Royal Society Interface, 2010. **7**(50): p. 1293-1299.
25. Kanematsu, H. and D.M. Barry, *Biofilm and materials science*. 2015: Springer.
26. Cheng, K., D. Akin, and J. Costerton. *Rumen bacteria: interaction with particulate dietary components and response to dietary variation*. in *Federation proceedings*. 1977.
27. Costerton, J., R. Irvin, and K. Cheng, *The bacterial glycocalyx in nature and disease.* Annual Reviews in Microbiology, 1981. **35**(1): p. 299-324.
28. Nickel, J.C., et al., *Tobramycin resistance of Pseudomonas aeruginosa cells growing as a biofilm on urinary catheter material.* Antimicrob Agents Chemother, 1985. **27**(4): p. 619-24.
29. Høiby, N., *A short history of microbial biofilms and biofilm infections.* Apmis, 2017. **125**(4): p. 272-275.
30. Lappin-Scott, H., S. Burton, and P. Stoodley, *Revealing a world of biofilms—the pioneering research of Bill Costerton.* Nature Reviews Microbiology, 2014. **12**(11): p. 781-787.
31. Berne, C., et al., *Bacterial adhesion at the single-cell level.* Nature Reviews Microbiology, 2018. **16**(10): p. 616-627.
32. Meireles, A., et al., *Methods to study microbial adhesion on abiotic surfaces.* AIMS Bioengineering, 2015. **2**(4): p. 297-309.
33. Karaguler, T., H. Kahraman, and M. Tuter, *Analyzing effects of ELF electromagnetic fields on removing bacterial biofilm.* Biocybernetics and biomedical engineering, 2017. **37**(2): p. 336-340.
34. Tuson, H.H. and D.B. Weibel, *Bacteria–surface interactions.* Soft matter, 2013. **9**(17): p. 4368-4380.
35. Vigeant, M.A.-S., et al., *Reversible and irreversible adhesion of motile Escherichia coli cells analyzed by total internal reflection aqueous fluorescence microscopy.* Applied and environmental microbiology, 2002. **68**(6): p. 2794-2801.
36. Marshall, K.C., R. Stout, and R. Mitchell, *Mechanism of the initial events in the sorption of marine bacteria to surfaces.* Microbiology, 1971. **68**(3): p. 337-348.
37. Ammar, Y., et al., *Influence of surface roughness on the initial formation of biofilm.* Surface and Coatings Technology, 2015. **284**: p. 410-416.
38. Beloin, C., A. Roux, and J.-M. Ghigo, *Escherichia coli biofilms*, in *Bacterial biofilms*. 2008, Springer. p. 249-289.
39. Stoodley, P., et al., *Biofilms, biomaterials, and device-related infections*, in *Handbook of polymer applications in medicine and medical devices*. 2013, Elsevier. p. 77-101.
40. Garrett, T.R., M. Bhakoo, and Z. Zhang, *Bacterial adhesion and biofilms on surfaces.* Progress in Natural Science, 2008. **18**(9): p. 1049-1056.
41. Van Houdt, R. and C.W. Michiels, *Role of bacterial cell surface structures in Escherichia coli biofilm formation.* Research in microbiology, 2005. **156**(5-6): p. 626-633.
42. Petrova, O.E. and K. Sauer, *Sticky situations: key components that control bacterial surface attachment.* Journal of bacteriology, 2012. **194**(10): p. 2413-2425.
43. T Garrison, A. and R. W Huigens III, *Eradicating bacterial biofilms with natural products and their inspired analogues that operate through unique mechanisms.* Current topics in medicinal chemistry, 2017. **17**(17): p. 1954-1964.
44. Maier, R.M., I.L. Pepper, and C.P. Gerba, *Environmental microbiology*. Vol. 397. 2009: Academic press.
45. Kolter, R., D.A. Siegele, and A. Tormo, *The stationary phase of the bacterial life cycle.* Annual Reviews in Microbiology, 1993. **47**(1): p. 855-874.
46. Kaplan, J.á., *Biofilm dispersal: mechanisms, clinical implications, and potential therapeutic uses.* Journal of dental research, 2010. **89**(3): p. 205-218.

47. Wille, J. and T. Coenye, *Biofilm dispersion: the key to biofilm eradication or opening Pandora's box?* Biofilm, 2020: p. 100027.
48. Watnick, P. and R. Kolter, *Biofilm, city of microbes.* Journal of bacteriology, 2000. **182**(10): p. 2675-2679.
49. Lebeaux, D., J.-M. Ghigo, and C. Beloin, *Biofilm-related infections: bridging the gap between clinical management and fundamental aspects of recalcitrance toward antibiotics.* Microbiology and Molecular Biology Reviews, 2014. **78**(3): p. 510-543.
50. Lebeaux, D., et al., *From in vitro to in vivo models of bacterial biofilm-related infections.* Pathogens, 2013. **2**(2): p. 288-356.
51. Videla, H. and L. Herrera, *Biocorrosion*, in *Studies in Surface Science and Catalysis*. 2004, Elsevier. p. 193-218.
52. Beech, I.B. and J. Sunner, *Biocorrosion: towards understanding interactions between biofilms and metals.* Current opinion in Biotechnology, 2004. **15**(3): p. 181-186.
53. de Carvalho, C.C., *Marine biofilms: a successful microbial strategy with economic implications.* Frontiers in marine science, 2018. **5**: p. 126.
54. Stoodley, P., et al., *Biofilm material properties as related to shear-induced deformation and detachment phenomena.* Journal of Industrial Microbiology and Biotechnology, 2002. **29**(6): p. 361-367.
55. Brindle, E.R., D.A. Miller, and P.S. Stewart, *Hydrodynamic deformation and removal of Staphylococcus epidermidis biofilms treated with urea, chlorhexidine, iron chloride, or DispersinB.* Biotechnology and bioengineering, 2011. **108**(12): p. 2968-2977.
56. Wagner, M. and H. Horn, *Optical coherence tomography in biofilm research: a comprehensive review.* Biotechnology and Bioengineering, 2017. **114**(7): p. 1386-1402.
57. Wagner, M., et al., *Investigation of the mesoscale structure and volumetric features of biofilms using optical coherence tomography.* Biotechnology and bioengineering, 2010. **107**(5): p. 844-853.
58. Blauert, F., H. Horn, and M. Wagner, *Time‐resolved biofilm deformation measurements using optical coherence tomography.* Biotechnology and bioengineering, 2015. **112**(9): p. 1893-1905.
59. Klapper, I., et al., *Viscoelastic fluid description of bacterial biofilm material properties.* Biotechnology and bioengineering, 2002. **80**(3): p. 289-296.
60. Drescher, K., et al., *Biofilm streamers cause catastrophic disruption of flow with consequences for environmental and medical systems.* Proceedings of the National Academy of Sciences, 2013. **110**(11): p. 4345-4350.
61. Picologlou, B.F., N. Zelver, and W.G. Characklis. *Biofilm growth and hydraulic performance*. in *Journal of the Hydraulics Division*. 1980.
62. Valiei, A., et al., *A web of streamers: biofilm formation in a porous microfluidic device.* Lab on a Chip, 2012. **12**(24): p. 5133-5137.
63. Hassanpourfard, M., et al., *Bacterial floc mediated rapid streamer formation in creeping flows.* Scientific reports, 2015. **5**: p. 13070.
64. Danhorn, T. and C. Fuqua, *Biofilm formation by plant-associated bacteria.* Annu. Rev. Microbiol., 2007. **61**: p. 401-422.
65. Gunawardena, J., *Models in biology:'accurate descriptions of our pathetic thinking'.* BMC biology, 2014. **12**(1): p. 29.
66. Mattei, M., et al., *Continuum and discrete approach in modeling biofilm development and structure: a review.* Journal of Mathematical Biology, 2018. **76**(4): p. 945-1003.
67. Rittmann, B.E. and P.L. McCarty, *Evaluation of steady‐state‐biofilm kinetics.* Biotechnology and Bioengineering, 1980. **22**(11): p. 2359-2373.
68. Williamson, K. and P.L. McCarty, *A model of substrate utilization by bacterial films.* Journal (Water Pollution Control Federation), 1976: p. 9-24.
69. Rittmann, B.E. and P.L. McCarty, *Model of steady‐state‐biofilm kinetics.* Biotechnology and bioengineering, 1980. **22**(11): p. 2343-2357.

70. Rittman, B.E., *The effect of shear stress on biofilm loss rate.* Biotechnology and Bioengineering, 1982. **24**(2): p. 501-506.
71. Wanner, O. and W. Gujer, *A multispecies biofilm model.* Biotechnology and bioengineering, 1986. **28**(3): p. 314-328.
72. Suraishkumar, G., *Mass Flux*, in *Continuum Analysis of Biological Systems*. 2014, Springer. p. 21-67.
73. Wanner, O. and P. Reichert, *Mathematical modeling of mixed‐culture biofilms.* Biotechnology and bioengineering, 1996. **49**(2): p. 172-184.
74. Rauch, W., H. Vanhooren, and P.A. Vanrolleghem, *A simplified mixed-culture biofilm model.* Water Research, 1999. **33**(9): p. 2148-2162.
75. Rittmann, B.E., D. Stilwell, and A. Ohashi, *The transient-state, multiple-species biofilm model for biofiltration processes.* Water Research, 2002. **36**(9): p. 2342-2356.
76. Eberl, H.J., D.F. Parker, and M.C. Vanloosdrecht, *A new deterministic spatio-temporal continuum model for biofilm development.* Computational and Mathematical Methods in Medicine, 2001. **3**(3): p. 161-175.
77. Eberl, H.J. and M.A. Efendiev, *A transient density-dependent diffusion-reaction model for the limitation of antibiotic penetration in biofilms.* Electronic Journal of Differential Equations (EJDE)[electronic only], 2003. **2003**: p. 123-142.
78. Eberl, H.J., H. Khassehkhan, and L. Demaret, *A mixed-culture model of a probiotic biofilm control system.* Computational and Mathematical Methods in Medicine, 2010. **11**(2): p. 99-118.
79. Klapper, I. and J. Dockery, *Finger formation in biofilm layers.* SIAM Journal on Applied Mathematics, 2002. **62**(3): p. 853-869.
80. Klapper, I., *Effect of heterogeneous structure in mechanically unstressed biofilms on overall growth.* Bulletin of Mathematical Biology, 2004. **66**(4): p. 809-824.
81. Dupin, H.J., P.K. Kitanidis, and P.L. McCarty, *Pore‐scale modeling of biological clogging due to aggregate expansion: A material mechanics approach.* Water Resources Research, 2001. **37**(12): p. 2965-2979.
82. Taherzadeh, D., et al., *Computational study of the drag and oscillatory movement of biofilm streamers in fast flows.* Biotechnology and bioengineering, 2010. **105**(3): p. 600-610.
83. Tierra, G., et al., *Multicomponent model of deformation and detachment of a biofilm under fluid flow.* Journal of The Royal Society Interface, 2015. **12**(106): p. 20150045.
84. Witten Jr, T. and L.M. Sander, *Diffusion-limited aggregation, a kinetic critical phenomenon.* Physical review letters, 1981. **47**(19): p. 1400.
85. Matsushita, M. and H. Fujikawa, *Diffusion-limited growth in bacterial colony formation.* Physica A: Statistical Mechanics and its Applications, 1990. **168**(1): p. 498-506.
86. Fujikawa, H., *Diversity of the growth patterns of Bacillus subtilis colonies on agar plates.* FEMS microbiology ecology, 1994. **13**(3): p. 159-167.
87. Wimpenny, J.W. and R. Colasanti, *A unifying hypothesis for the structure of microbial biofilms based on cellular automaton models.* FEMS microbiology ecology, 1997. **22**(1): p. 1-16.
88. Ben-Jacob, E., et al., *Generic modelling of cooperative growth patterns in bacterial colonies.* Nature, 1994. **368**(6466): p. 46-49.
89. Picioreanu, C., M.C. van Loosdrecht, and J.J. Heijnen, *A new combined differential‐discrete cellular automaton approach for biofilm modeling: Application for growth in gel beads.* Biotechnology and bioengineering, 1998. **57**(6): p. 718-731.
90. Picioreanu, C., M.C. Van Loosdrecht, and J.J. Heijnen, *Mathematical modeling of biofilm structure with a hybrid differential‐discrete cellular automaton approach.* Biotechnology and bioengineering, 1998. **58**(1): p. 101-116.
91. Horn, H. and S. Lackner, *Modeling of biofilm systems: a review*, in *Productive Biofilms*. 2014, Springer. p. 53-76.
92. Picioreanu, C., M. Van Loosdrecht, and J. Heijnen, *Discrete-differential modelling of biofilm structure.* Water Science and Technology, 1999. **39**(7): p. 115-122.

93. Picioreanu, C., M.C. Van Loosdrecht, and J.J. Heijnen, *Two‐dimensional model of biofilm detachment caused by internal stress from liquid flow.* Biotechnology and bioengineering, 2001. **72**(2): p. 205-218.
94. DeAngelis, D.L. and V. Grimm, *Individual-based models in ecology after four decades.* F1000prime reports, 2014. **6**.
95. Kreft, J., G. Booth, and J. Wimpenny. *Applications of individual-based modelling in microbial ecology*. in *Microbial biosystems: new frontiers (Proceedings of the eighth international symposium on microbial ecology). Atlantic Canada Society for Microbial Ecology, Halifax*. 1999.
96. Kreft, J.-U., G. Booth, and J.W. Wimpenny, *BacSim, a simulator for individual-based modelling of bacterial colony growth.* Microbiology, 1998. **144**(12): p. 3275-3287.
97. Xavier, J.B., C. Picioreanu, and M.C. Van Loosdrecht, *A framework for multidimensional modelling of activity and structure of multispecies biofilms.* Environmental microbiology, 2005. **7**(8): p. 1085-1103.
98. Xavier, J.d.B., C. Picioreanu, and M.C. van Loosdrecht, *A general description of detachment for multidimensional modelling of biofilms.* Biotechnology and bioengineering, 2005. **91**(6): p. 651-669.
99. Alpkvist, E., et al., *Three‐dimensional biofilm model with individual cells and continuum EPS matrix.* Biotechnology and bioengineering, 2006. **94**(5): p. 961-979.
100. Lardon, L.A., et al., *iDynoMiCS: next‐generation individual‐based modelling of biofilms.* Environmental microbiology, 2011. **13**(9): p. 2416-2434.
101. Gingold, R.A. and J.J. Monaghan, *Smoothed particle hydrodynamics: theory and application to non-spherical stars.* Monthly notices of the royal astronomical society, 1977. **181**(3): p. 375-389.
102. Jayathilake, P.G., et al., *A mechanistic Individual-based Model of microbial communities.* PloS one, 2017. **12**(8): p. e0181965.
103. Gogulancea, V., et al., *Individual based model links thermodynamics, chemical speciation and environmental conditions to microbial growth.* Frontiers in microbiology, 2019. **10**: p. 1871.
104. Hellweger, F.L., et al., *Advancing microbial sciences by individual-based modelling.* Nature Reviews Microbiology, 2016. **14**(7): p. 461-471.
105. Shaw, T., et al., *Commonality of elastic relaxation times in biofilms.* Physical review letters, 2004. **93**(9): p. 098102.
106. Cense, A., et al., *Removal of biofilms by impinging water droplets.* Journal of applied physics, 2006. **100**(12): p. 124701.
107. Stoodley, P., et al., *Growth and detachment of cell clusters from mature mixed-species biofilms.* Applied and environmental microbiology, 2001. **67**(12): p. 5608-5613.
108. Papanicolaou, G. and S. Zaoutsos, *Viscoelastic constitutive modeling of creep and stress relaxation in polymers and polymer matrix composites*, in *Creep and fatigue in polymer matrix composites*. 2019, Elsevier. p. 3-59.
109. Panwar, V. and K. Pal, *Chapter 12 - Dynamic Mechanical Analysis of Clay–Polymer Nanocomposites*, in *Clay-Polymer Nanocomposites*, K. Jlassi, M.M. Chehimi, and S. Thomas, Editors. 2017, Elsevier. p. 413-441.
110. Gould, T.E., et al., *Chapter 6 - Mouth Protection in Sports*, in *Materials in Sports Equipment (Second Edition)*, A. Subic, Editor. 2019, Woodhead Publishing. p. 199-231.
111. Guélon, T., J.-D. Mathias, and P. Stoodley, *Advances in biofilm mechanics*, in *Biofilm highlights*. 2011, Springer. p. 111-139.
112. Nihat Özkaya, D.L., David Goldsheyder, Margareta Nordin, *Mechanical Properties of Biological Tissues*, in *Fundamentals of Biomechanics*. 2017, Springer. p. 361-387.
113. Körstgens, V., et al., *Influence of calcium ions on the mechanical properties of a model biofilm of mucoid Pseudomonas aeruginosa.* Water Science and Technology, 2001. **43**(6): p. 49-57.
114. Cense, A., et al., *Mechanical properties and failure of Streptococcus mutans biofilms, studied using a microindentation device.* Journal of microbiological methods, 2006. **67**(3): p. 463-472.

115. Boudarel, H., et al., *Towards standardized mechanical characterization of microbial biofilms: analysis and critical review.* NPJ biofilms and microbiomes, 2018. **4**(1): p. 1-15.
116. Catão, E.C., et al., *Shear stress as a major driver of marine biofilm communities in the NW Mediterranean Sea.* Frontiers in microbiology, 2019. **10**: p. 1768.
117. Wloka, M., et al., *Rheological properties of viscoelastic biofilm extracellular polymeric substances and comparison to the behavior of calcium alginate gels.* Colloid and Polymer Science, 2004. **282**(10): p. 1067-1076.
118. Wloka, M., et al., *Structure and rheological behaviour of the extracellular polymeric substance network of mucoid Pseudomonas aeruginosa biofilms.* biofilms, 2005. **2**(4): p. 275-283.
119. Azeredo, J., et al., *Critical review on biofilm methods.* Critical reviews in microbiology, 2017. **43**(3): p. 313-351.
120. Ahimou, F., et al., *Biofilm cohesiveness measurement using a novel atomic force microscopy methodology.* Appl. Environ. Microbiol., 2007. **73**(9): p. 2897-2904.
121. Lau, P.C., et al., *Differential lipopolysaccharide core capping leads to quantitative and correlated modifications of mechanical and structural properties in Pseudomonas aeruginosa biofilms.* Journal of bacteriology, 2009. **191**(21): p. 6618-6631.
122. Böl, M., et al., *Recent advances in mechanical characterisation of biofilm and their significance for material modelling.* Critical reviews in biotechnology, 2013. **33**(2): p. 145-171.
123. Stoodley, P., et al., *The influence of fluid shear and AlCl3 on the material properties of Pseudomonas aeruginosa PAO1 and Desulfovibrio sp. EX265 biofilms.* Water Science and Technology, 2001. **43**(6): p. 113-120.
124. Dunsmore, B., et al., *The influence of fluid shear on the structure and material properties of sulphate-reducing bacterial biofilms.* Journal of Industrial Microbiology and Biotechnology, 2002. **29**(6): p. 347-353.
125. Lahaye, E., et al., *Does water activity rule P. mirabilis periodic swarming? II. Viscoelasticity and water balance during swarming.* Biomacromolecules, 2007. **8**(4): p. 1228-1235.
126. Houari, A., et al., *Rheology of biofilms formed at the surface of NF membranes in a drinking water production unit.* Biofouling, 2008. **24**(4): p. 235-240.
127. Zhang, Z.-X., *Chapter 5 - Effect of Temperature on Rock Fracture*, in *Rock Fracture and Blasting*, Z.-X. Zhang, Editor. 2016, Butterworth-Heinemann. p. 111-133.
128. Epaarachchi, J., *The effect of viscoelasticity on fatigue behaviour of polymer matrix composites*, in *Creep and fatigue in polymer matrix composites*. 2011, Elsevier. p. 492-513.
129. Peterson, B.W., et al., *Viscoelasticity of biofilms and their recalcitrance to mechanical and chemical challenges.* FEMS microbiology reviews, 2015. **39**(2): p. 234-245.
130. Bansal, A., P. Setia, and R. Chawla, *Prediction of Mechanical Properties of Graphene/Copper Nanolayered Composites Using LAMMPS.* Molecular Dynamics Simulation of Nanocomposites using BIOVIA Materials Studio, Lammps and Gromacs, 2019: p. 114.
131. Hong, Y., J. Zhang, and X.C. Zeng, *Monolayer and bilayer polyaniline C 3 N: two-dimensional semiconductors with high thermal conductivity.* Nanoscale, 2018. **10**(9): p. 4301-4310.
132. Luo, C. and J.-U. Sommer, *Coding coarse grained polymer model for LAMMPS and its application to polymer crystallization.* Computer Physics Communications, 2009. **180**(8): p. 1382-1391.
133. Wang, Q. and T. Zhang, *Review of mathematical models for biofilms.* Solid State Communications, 2010. **150**(21): p. 1009-1022.
134. Kampen, W.H., *Chapter 4 - Nutritional Requirements in Fermentation Processes*, in *Fermentation and Biochemical Engineering Handbook (Third Edition)*, H.C. Vogel and C.M. Todaro, Editors. 2014, William Andrew Publishing: Boston. p. 37-57.
135. Fan, L.S., et al., *Diffusion of phenol through a biofilm grown on activated carbon particles in a draft ‐tube three ‐phase fluidized ‐bed bioreactor.* Biotechnology and Bioengineering, 1990. **35**(3): p. 279-286.

136. Tsuneda, S., et al., *Enhancement of nitrifying biofilm formation using selected EPS produced by heterotrophic bacteria.* Water Science and Technology, 2001. **43**(6): p. 197-204.
137. Cundall, P.A., *The measurement and analysis of accelerations in rock slopes.* PhD Thesis, Imperial College of Science & Technology, 1971.
138. Lee, J.G., *Computational materials science: an introduction*. 2016: CRC press.
139. Silbert, L.E., et al., *Granular flow down an inclined plane: Bagnold scaling and rheology.* Physical Review E, 2001. **64**(5): p. 051302.
140. Luo, J. and Y. Liu. *Coupled CFD-DEM Simulation of Tea Particles in a Cylinder Fixation Equipment*. in *Journal of Physics: Conference Series*. 2019. IOP Publishing.
141. Li, Z. and H. Wang, *Drag force, diffusion coefficient, and electric mobility of small particles. I. Theory applicable to the free-molecule regime.* Physical Review E, 2003. **68**(6): p. 061206.
142. Sun, R. and H. Xiao, *SediFoam: A general-purpose, open-source CFD–DEM solver for particle-laden flow with emphasis on sediment transport.* Computers & Geosciences, 2016. **89**: p. 207-219.
143. Gupta, P., *Verification and validation of a DEM-CFD model and multiscale modelling of cohesive fluidization regimes.* 2015.
144. Sun, R., H. Xiao, and H. Sun, *Realistic representation of grain shapes in CFD–DEM simulations of sediment transport with a bonded-sphere approach.* Advances in water resources, 2017. **107**: p. 421-438.
145. Sun, R. and H. Xiao, *Diffusion-based coarse graining in hybrid continuum–discrete solvers: theoretical formulation and a priori tests.* International Journal of Multiphase Flow, 2015. **77**: p. 142-157.
146. Israelachvili, J.N., *Intermolecular and surface forces*. 2011: Academic press.
147. Sun, R., H. Xiao, and H. Sun, *Investigating the settling dynamics of cohesive silt particles with particle-resolving simulations.* Advances in Water Resources, 2018. **111**: p. 406-422.
148. Sun, R. and H. Xiao, *Diffusion-based coarse graining in hybrid continuum–discrete solvers: Applications in CFD–DEM.* International Journal of Multiphase Flow, 2015. **72**: p. 233-247.
149. Syamlal, M., et al., *Theory guide.* US Department of Energy, Morgantown, WV, 1993.
150. Garside, J. and M.R. Al-Dibouni, *Velocity-voidage relationships for fluidization and sedimentation in solid-liquid systems.* Industrial & engineering chemistry process design and development, 1977. **16**(2): p. 206-214.
151. Van Rijn, L.C., *Sediment transport, part I: bed load transport.* Journal of hydraulic engineering, 1984. **110**(10): p. 1431-1456.
152. Zhu, H., et al., *Discrete particle simulation of particulate systems: theoretical developments.* Chemical Engineering Science, 2007. **62**(13): p. 3378-3396.
153. Hernández-Jiménez, E., et al., *Biofilm vs. planktonic bacterial mode of growth: which do human macrophages prefer?* Biochemical and biophysical research communications, 2013. **441**(4): p. 947-952.
154. Banerjee, D., et al., *A review on basic biology of bacterial biofilm infections and their treatments by nanotechnology-based approaches.* Proceedings of the National Academy of Sciences, India Section B: Biological Sciences, 2019: p. 1-17.
155. Srivastava, S. and A. Bhargava, *Biofilms and human health.* Biotechnology Letters, 2016. **38**(1): p. 1-22.
156. O'Toole, G., H.B. Kaplan, and R. Kolter, *Biofilm formation as microbial development.* Annual Reviews in Microbiology, 2000. **54**(1): p. 49-79.
157. Beech, I., et al., *Microbially-influenced corrosion: damage to prostheses, delight for bacteria.* The International journal of artificial organs, 2006. **29**(4): p. 443-452.
158. Guo, J., et al., *Polymers for combating biocorrosion.* Frontiers in Materials, 2018. **5**: p. 10.
159. Procópio, L., *The role of biofilms in the corrosion of steel in marine environments.* World Journal of Microbiology and Biotechnology, 2019. **35**(5): p. 1-8.

160. Aruliah, R. and Y.-P. Ting, *Characterization of corrosive bacterial consortia isolated from water in a cooling tower.* International Scholarly Research Notices, 2014. **2014**.
161. Chambless, J.D. and P.S. Stewart, *A three‐dimensional computer model analysis of three hypothetical biofilm detachment mechanisms.* Biotechnology and bioengineering, 2007. **97**(6): p. 1573-1584.
162. Karimi, A., et al., *Interplay of physical mechanisms and biofilm processes: review of microfluidic methods.* Lab on a Chip, 2015. **15**(1): p. 23-42.
163. Di Martino, P., *Extracellular polymeric substances, a key element in understanding biofilm phenotype.* AIMS microbiology, 2018. **4**(2): p. 274.
164. Ni, B.J., et al., *Characterization of extracellular polymeric substances produced by mixed microorganisms in activated sludge with gel-permeating chromatography, excitation-emission matrix fluorescence spectroscopy measurement and kinetic modeling.* Water Res, 2009. **43**(5): p. 1350-8.
165. Stoodley, P., L. Hall-Stoodley, and H.M. Lappin-Scott, *[21] Detachment, surface migration, and other dynamic behavior in bacterial biofilms revealed by digital time-lapse imaging.* Methods in enzymology, 2001. **337**: p. 306-319.
166. Vollmayr-Lee, K., *Introduction to molecular dynamics simulations.* American Journal of Physics, 2020. **88**(5): p. 401-422.
167. Aranson, I., *The aquatic dance of bacteria.* Physics, 2013. **6**: p. 61.
168. Paul, E., et al., *Effect of shear stress and growth conditions on detachment and physical properties of biofilms.* Water research, 2012. **46**(17): p. 5499-5508.
169. Choi, Y. and E. Morgenroth, *Monitoring biofilm detachment under dynamic changes in shear stress using laser-based particle size analysis and mass fractionation.* Water Science and Technology, 2003. **47**(5): p. 69-76.
170. Kundu, P.K., I.M. Cohen, and D.R. Dowling, *Chapter 10 - Boundary Layers and Related Topics*, in *Fluid Mechanics (Sixth Edition)*, P.K. Kundu, I.M. Cohen, and D.R. Dowling, Editors. 2016, Academic Press: Boston. p. 469-532.
171. Walter, M., et al., *Detachment characteristics of a mixed culture biofilm using particle size analysis.* Chemical engineering journal, 2013. **228**: p. 1140-1147.
172. Zhao, Y.X., et al., *Insights into biofilm carriers for biological wastewater treatment processes: Current state-of-the-art, challenges, and opportunities.* Bioresource Technology, 2019. **288**.
173. Hall‐Stoodley, L. and P. Stoodley, *Evolving concepts in biofilm infections.* Cellular microbiology, 2009. **11**: p. 1034-1043.
174. Cao, Y.Y., et al., *Nanostructured titanium surfaces exhibit recalcitrance towards Staphylococcus epidermidis biofilm formation.* Scientific Reports, 2018. **8**.
175. Vrouwenvelder, J., et al., *Impact of flow regime on pressure drop increase and biomass accumulation and morphology in membrane systems.* Water research, 2010. **44**(3): p. 689-702.
176. Fabbri, S., et al., *A marine biofilm flow cell for in situ screening marine fouling control coatings using optical coherence tomography.* Ocean Engineering, 2018. **170**: p. 321-328.
177. Wang, X., et al., *The mechanical analysis of the biofilm streamer nucleation and geometry characterization in microfluidic channels.* Computational and mathematical methods in medicine, 2016. **2016**.
178. Schrader, M., et al., *Design of a CFD-DEM-based method for mechanical stress calculation and its application to glass bead-enhanced cultivations of filamentous Lentzea aerocolonigenes.* Biochemical Engineering Journal, 2019. **148**: p. 116-130.
179. Gu, Y., A. Ozel, and S. Sundaresan, *A modified cohesion model for CFD–DEM simulations of fluidization.* Powder technology, 2016. **296**: p. 17-28.
180. Jayathilake, P.G., et al., *Modelling bacterial twitching in fluid flows: a CFD-DEM approach.* Scientific reports, 2019. **9**(1): p. 1-10.
181. Li, B., et al., *NUFEB: A massively parallel simulator for individual-based modelling of microbial communities.* PLoS Computational Biology, 2019. **15**(12).

182. Elvitigala, K., et al. *Numerical Simulation of Shaking Optimization in a Suspension Culture of iPS Cells*. in *International Conference on Global Research and Education*. 2018. Springer.
183. Kleinstreuer, C. and Z. Xu, *Computational microfluidics applied to drug delivery in pulmonary and arterial systems.* Microfluidics: fundamentals, devices, and applications. Wiley, Weinheim, 2018.
184. Plimpton, S., *Fast parallel algorithms for short-range molecular dynamics*. 1993, Sandia National Labs., Albuquerque, NM (United States).
185. Greenshields, C.J., *OpenFoam user guide. Version 6.* OpenFOAM Foundation Ltd July, 2017.
186. Song, Y. and J.B. Perot, *Cfd simulation of the nrel phase vi rotor.* Wind engineering, 2015. **39**(3): p. 299-309.
187. Milferstedt, K., M.N. Pons, and E. Morgenroth, *Analyzing characteristic length scales in biofilm structures.* Biotechnology and bioengineering, 2009. **102**(2): p. 368-379.
188. Raunkjær, K., P.H. Nielsen, and T. Hvitved-Jacobsen, *Acetate removal in sewer biofilms under aerobic conditions.* Water research, 1997. **31**(11): p. 2727-2736.
189. Guhados, G., W. Wan, and J.L. Hutter, *Measurement of the elastic modulus of single bacterial cellulose fibers using atomic force microscopy.* Langmuir, 2005. **21**(14): p. 6642-6646.
190. Konhauser, K.O. and M.K. Gingras, *Linking geomicrobiology with ichnology in marine sediments.* Palaios, 2007. **22**(4): p. 339-342.
191. Hsieh, Y.C., et al., *An estimation of the Young's modulus of bacterial cellulose filaments.* Cellulose, 2008. **15**(4): p. 507-513.
192. Malarkey, J., et al., *The pervasive role of biological cohesion in bedform development.* Nature communications, 2015. **6**: p. 6257.
193. Storck, T., et al., *Variable cell morphology approach for individual-based modeling of microbial communities.* Biophysical journal, 2014. **106**(9): p. 2037-2048.
194. Sumer, B.M., *Hydrodynamics around cylindrical strucures*. Vol. 26. 2006: World scientific.
195. Asyikin, M.T., *CFD simulation of vortex induced vibration of a cylindrical structure*. 2012, Institutt for bygg, anlegg og transport.
196. Oliveira, P.J., *Method for time-dependent simulations of viscoelastic flows: vortex shedding behind cylinder.* Journal of non-newtonian fluid mechanics, 2001. **101**(1-3): p. 113-137.
197. SARIOĞLU, M. and T. Yavuz, *Vortex shedding from circular and rectangular cylinders placed horizontally in a turbulent flow.* Turkish Journal of Engineering and Environmental Sciences, 2000. **24**(4): p. 217-228.
198. Ristroph, L. and J. Zhang, *Anomalous hydrodynamic drafting of interacting flapping flags.* Physical review letters, 2008. **101**(19): p. 194502.
199. Favier, J., A. Revell, and A. Pinelli, *Numerical study of flapping filaments in a uniform fluid flow.* Journal of Fluids and Structures, 2015. **53**: p. 26-35.
200. Jana, S., et al., *Nonlinear rheological characteristics of single species bacterial biofilms.* NPJ biofilms and microbiomes, 2020. **6**(1): p. 1-11.
201. Xia, Y., P. Duan, and J. Chen, *Modelling the nanomechanical responses of biofilms grown on the indenter probe.* Processes, 2018. **6**(7): p. 84.
202. Flemming, H.-C., T.R. Neu, and D.J. Wozniak, *The EPS matrix: the "house of biofilm cells".* Journal of bacteriology, 2007. **189**(22): p. 7945-7947.
203. Singh, R., D. Paul, and R.K. Jain, *Biofilms: implications in bioremediation.* Trends in microbiology, 2006. **14**(9): p. 389-397.
204. Sehar, S. and I. Naz, *Role of the biofilms in wastewater treatment.* Microbial biofilms-importance and applications, 2016: p. 121-144.
205. Capdeville, B. and J. Rols, *Introduction to biofilms in water and wastewater treatment*, in *Biofilms—science and technology*. 1992, Springer. p. 13-20.
206. Abe, Y., et al., *Cohesiveness and hydrodynamic properties of young drinking water biofilms.* Water Research, 2012. **46**(4): p. 1155-1166.

207. Tasneem, U., et al., *Biofilm producing bacteria: A serious threat to public health in developing countries.* J Food Sci Nutr. 2018; 1 (2): 25-31. J Food Sci Nutr 2018 Volume 1 Issue, 2018. **2**.
208. Lau, P.C.Y., et al., *Absolute quantitation of bacterial biofilm adhesion and viscoelasticity by microbead force spectroscopy.* Biophysical journal, 2009. **96**(7): p. 2935-2948.
209. Kwon, T.-H. and S. Kim, *Measuring elastic modulus of bacterial biofilms in a liquid phase using atomic force microscopy.* Geomechanics Eng, 2017. **12**: p. 863-870.
210. Stoodley, P., et al., *The formation of migratory ripples in a mixed species bacterial biofilm growing in turbulent flow.* Environmental microbiology, 1999. **1**(5): p. 447-455.
211. Song, X., et al., *Relationship between putative eps genes and production of exopolysaccharide in Lactobacillus casei LC2W.* Frontiers in microbiology, 2018. **9**: p. 1882.
212. Ali, A., et al., *Mutations in the extracellular protein secretion pathway genes (eps) interfere with rugose polysaccharide production in and motility of Vibrio cholerae.* Infection and immunity, 2000. **68**(4): p. 1967-1974.
213. Hibbing, M.E., et al., *Bacterial competition: surviving and thriving in the microbial jungle.* Nature Reviews Microbiology, 2010. **8**(1): p. 15-25.
214. Fish, K., A. Osborn, and J. Boxall, *Biofilm structures (EPS and bacterial communities) in drinking water distribution systems are conditioned by hydraulics and influence discolouration.* Science of the Total Environment, 2017. **593**: p. 571-580.
215. Whitehouse, D., *3 - Profile and areal (3D) parameter characterization*, in *Surfaces and Their Measurement*, D. Whitehouse, Editor. 2002, Kogan Page Science: Oxford. p. 48-95.
216. Thompson, A.P., S.J. Plimpton, and W. Mattson, *General formulation of pressure and stress tensor for arbitrary many-body interaction potentials under periodic boundary conditions.* The Journal of chemical physics, 2009. **131**(15): p. 154107.
217. Heyes, D.M., *Pressure tensor of partial-charge and point-dipole lattices with bulk and surface geometries.* Physical Review B, 1994. **49**(2): p. 755.
218. Lower, S.K., *Directed natural forces of affinity between a bacterium and mineral.* American Journal of Science, 2005. **305**(6-8): p. 752-765.
219. Fang, H.H., K.-Y. Chan, and L.-C. Xu, *Quantification of bacterial adhesion forces using atomic force microscopy (AFM).* Journal of microbiological methods, 2000. **40**(1): p. 89-97.
220. Bos, R., H.C. Van der Mei, and H.J. Busscher, *Physico-chemistry of initial microbial adhesive interactions–its mechanisms and methods for study.* FEMS microbiology reviews, 1999. **23**(2): p. 179-230.
221. Jafari, M., et al., *Effect of biofilm structural deformation on hydraulic resistance during ultrafiltration: A numerical and experimental study.* Water research, 2018. **145**: p. 375-387.
222. Capurro, M. and F. Barberis, *9 - Evaluating the mechanical properties of biomaterials*, in *Biomaterials for Bone Regeneration*, P. Dubruel and S. Van Vlierberghe, Editors. 2014, Woodhead Publishing. p. 270-323.
223. Peterson, B.W., et al., *A distinguishable role of eDNA in the viscoelastic relaxation of biofilms.* MBio, 2013. **4**(5).
224. Peterson, B.W., et al., *Visualization of microbiological processes underlying stress relaxation in Pseudomonas aeruginosa biofilms.* Microscopy and Microanalysis, 2014. **20**(3): p. 912.
225. Inman, D., *DAMPING MODELS*, in *Encyclopedia of Vibration*, S. Braun, Editor. 2001, Elsevier: Oxford. p. 335-342.
226. Yu, P., et al., *Influence of surface properties on adhesion forces and attachment of Streptococcus mutans to zirconia in vitro.* BioMed research international, 2016. **2016**.
227. Rusconi, R., et al., *Secondary flow as a mechanism for the formation of biofilm streamers.* Biophysical journal, 2011. **100**(6): p. 1392-1399.
228. Hart, R., P.A. Cundall, and J. Lemos. *Formulation of a three-dimensional distinct element model—Part II. Mechanical calculations for motion and interaction of a system composed of many polyhedral blocks*. in *International Journal of Rock Mechanics and Mining Sciences & Geomechanics Abstracts*. 1988. Elsevier.

229. Burns, S.J., P.T. Piiroinen, and K.J. Hanley, *Critical time step for DEM simulations of dynamic systems using a Hertzian contact model.* International Journal for Numerical Methods in Engineering, 2019. **119**(5): p. 432-451.